

Electronic Thesis and Dissertation Repository

5-29-2015 12:00 AM

High Pressure and High Temperature Study of Magnesiochromite and Its Geophysical Implications

N M Tauhid Belal Khan, *The University of Western Ontario*

Supervisor: Dr. Sean Shieh, *The University of Western Ontario*

A thesis submitted in partial fulfillment of the requirements for the Master of Science degree in Geophysics

© N M Tauhid Belal Khan 2015

Follow this and additional works at: <https://ir.lib.uwo.ca/etd>



Part of the [Physical Sciences and Mathematics Commons](#)

Recommended Citation

Khan, N M Tauhid Belal, "High Pressure and High Temperature Study of Magnesiochromite and Its Geophysical Implications" (2015). *Electronic Thesis and Dissertation Repository*. 2902.
<https://ir.lib.uwo.ca/etd/2902>

This Dissertation/Thesis is brought to you for free and open access by Scholarship@Western. It has been accepted for inclusion in Electronic Thesis and Dissertation Repository by an authorized administrator of Scholarship@Western. For more information, please contact wlsadmin@uwo.ca.

«HIGH PRESSURE AND HIGH TEMPERATURE STUDY OF MAGNESIOCHROMITE
AND ITS GEOPHYSICAL IMPLICATIONS»

(Thesis format: Monograph)

by

«N M TAUHID BELAL KHAN»

Department of Earth Sciences «Geophysics»

A thesis submitted in partial fulfillment
of the requirements for the degree of
« Master of Science »

The School of Graduate and Postdoctoral Studies
The University of Western Ontario
London, Ontario, Canada

© « N M Tauhid Belal Khan » « 2015 »

Abstract

Magnesiochromite (MgCr_2O_4) is commonly found in the Earth's crust, upper mantle, meteorites, and possibly in lunar crust. Synchrotron X-ray diffraction measurements of MgCr_2O_4 using double-sided laser heating diamond anvil cell showed the dissociation of MgCr_2O_4 to $\text{Cr}_2\text{O}_3+\text{MgO}$ at ~ 15 GPa and to $\text{Mg}_2\text{Cr}_2\text{O}_5+\text{Cr}_2\text{O}_3$ below and above ~ 1500 K, respectively. At above 20 GPa, only a single phase CaTi_2O_4 -type structure of MgCr_2O_4 was observed at 1400-2000 K. Fitting the pressure-volume data of CaTi_2O_4 type structure of MgCr_2O_4 with Birch-Murnaghan equation of state yields volume at ambient condition (V_0) = $264.4(8) \text{ \AA}^3$, bulk modulus (K_0) = $185.4(4)$ GPa, and pressure derivative of the bulk modulus (K_0') = 4; and for CaTi_2O_4 type structure of natural chromite: $V_0 = 261(1) \text{ \AA}^3$, $K_0 = 175.4(2)$ GPa, $K_0' = 4$, and mLd-type $\text{Mg}_2\text{Cr}_2\text{O}_5$ yields: $V_0 = 338.9(8) \text{ \AA}^3$, $K_0 = 186.5(6)$ GPa, $K_0' = 4$. Obtained phase diagram and bulk modulus data provide important information to better understand the structure and dynamics of the deep earth.

Keywords

DAC, LHDAC, MgCr_2O_4 , CaTi_2O_4 , modified ludwigite, phase diagram, equation of state, bulk modulus, synchrotron, X-ray, high pressure, high temperature

Acknowledgements

Firstly, I would like to thank my supervisor, Dr. Sean Shieh, for his helpful advices, constructive discussions, patient instructions and support for the past two years.

I would also like to thank Dr. Clemens Prescher and Dr. Xinguo Hong for their patient, responsible work with synchrotron facility in Advanced Photon Source in Argonne National Laboratory and in National Synchrotron Light Source in Brookhaven National Laboratory, respectively. Their kindly technical assistance made my experiments went smoothly.

Thanks to my colleagues Ievgeniia Morozova and Tianqi Xie. My research life has more fun with their fruitful input.

I would like to thank Jon Jacobs, Ivan Barker, Barry Price, Stephen Wood and Dr. Wenjun Yong for their helps in technical issues in different stage of my experiments.

Most importantly, with full of my heart, I'd like to thank to my family for their support and encouragement. Without their help and understanding I would not have been able to finish this work.

Table of Contents

Abstract	ii
Acknowledgements	iii
Table of Contents	iv
List of Tables	vii
List of Figures	viii
List of Appendices	xii
List of Abbreviations	xiii
List of Symbols	xv
Chapter 1	1
1. Introduction	1
1.1. The Spinel Structure	1
1.2. Chromite Spinel	4
1.3. Objective of the thesis	12
Chapter 2	13
2. Experimental Method	13
2.1. Experiments and Instruments	13
2.2. The Diamond Anvil Cell	14
2.3. Synchrotron X-ray Radiation	16
2.4. Laser heating	19
2.5. Powder X-ray Diffraction	20
2.6. Raman Spectroscopy	23
2.7. Ruby Fluorescence Scale	24
2.8. Sample Preparation	25
2.8.1. Sample	25
2.8.2. DAC	25
2.8.3. Gasket Preparation	26

2.8.4.	Sample Loading	29
2.8.5.	Pressure medium	30
2.8.6.	Determination of Equations of state (EOS).....	31
2.8.7.	Murnaghan integrated linear EOS	32
2.8.8.	Birch-Murnaghan EOS.....	33
2.8.9.	The third-order Birch-Murnaghan EOS.....	34
2.9.	Analysis of X-Ray Diffraction Patterns.....	35
Chapter 3		37
3.	Phase diagram of $MgCr_2O_4$	37
3.1.	Experiment.....	37
3.2.	Results	38
3.3.	Discussion	45
Chapter 4		46
4.	Equation of State of $CaTi_2O_4$ type structure of $MgCr_2O_4$	46
4.1.	Experiment.....	46
4.2.	Results	47
4.3.	Discussion	52
Chapter 5		54
5.	Equation of State of modified ludwigite-type (mLd type) $Mg_2Cr_2O_5$ phase	54
5.1.	Experiment.....	54
5.2.	Results	55
5.3.	Discussion	61
Chapter 6		63
6.	Equation of State of $CaTi_2O_4$ type structure of Natural Chromite	63
6.1.	Experiment.....	63
6.2.	Results	64
6.3.	Discussion	68
Chapter 7		69
7.	Geophysical implications	69

Chapter 8	72
8. Conclusion	72
References	74
Appendices	83
Curriculum Vitae	93

List of Tables

Table 3.1. Results of high-pressure high-temperature experiments	40
Table 3.2. Lattice parameters, symmetry and space group of different phases obtained from MgCr ₂ O ₄	44
Table 3.3. Lattice parameters, symmetry and space group of different phases reported from references for MgCr ₂ O ₄ at ambient conditions. But the Tetragonal MgCr ₂ O ₄ is at 22.5GPa	44
Table 4.1. Unit-cell parameters of synthesised CaTi ₂ O ₄ type MgCr ₂ O ₄ at different pressure	49
Table 5.1. Unit-cell parameters of synthesised MgCr ₂ O ₅ type MgCr ₂ O ₄ at different pressure .	58
Table 6.1. Unit-cell parameters of synthesised CaTi ₂ O ₄ type of natural chromite at different pressure	65

List of Figures

Figure 1.1. The spinel structure. Red spheres are “Oxygen”, Gold spheres are “A-atom”, and Blue spheres are “B-atom”. Solid black line represents the boundary of unit cell. (Structural data from Yamanaka et al., 1983)	2
Figure.1.2. Phase diagram of $MgAl_2O_4$ reported by Ono et al. (2006). SP=Spinel-type, MA=MgO+ Al_2O_3 , CF= $CaFe_2O_4$ -type $MgAl_2O_4$, EP= ϵ -type $MgAl_2O_4$, CT= $CaTi_2O_4$ -type $MgAl_2O_4$	4
Figure 1.3. High-pressure polymorph of chromite first reported by Chen et al (2003), by studying in the shock veins of the Suizhou meteorite	5
Figure 1.4. Reflectance spectra of spinels (Cloutis et al., 2004). Gray spectra in background are the common lunar minerals	6
Figure 1.5. Spinels with Cr-numbers of at least about 80 is stable in cratonic Lithosphere (Stachel and Harris 2008)	7
Figure 1.6. Phase transformation Magnesiochromite spinel by Raman study (Wang et al. 2002)	9
Figure 1.7. Phase transition from cubic structure to tetragonal structure of magnesiochromite (Yong et al., 2012)	9
Figure 1.8. Phase diagram of $FeCr_2O_4$ at HP-HT. Solid lines represent phase boundaries. Sp = spinel-type $FeCr_2O_4$; mLd = modified ludwigite-type $Fe_2Cr_2O_5$; Es = Cr_2O_3 eskolaite; CF = $CaFe_2O_4$ -type $FeCr_2O_4$; CT = $CaTi_2O_4$ -type $FeCr_2O_4$. (Ishii et al. 2014)	10
Figure 1.9. Phase diagram of $MgCr_2O_4$ at HP-HT. Solid lines represent phase boundaries. A dashed line represents the extrapolated transition boundary of mLd + Es to CT. Sp = spinel-type $MgCr_2O_4$; mLd = modified ludwigite-type $Mg_2Cr_2O_5$; Es = corundum type Cr_2O_3 eskolaite; CT = $CaTi_2O_4$ -type $MgCr_2O_4$; Pc = rocksalt-type MgO periclase. (Ishii et al, 2015)	11
Figure 2.1. Experimental Setup of laser heated diamond anvil cell incorporating with synchrotron XRD	13
Figure 2.2. (a) Shapes of diamond anvils (b) culet designs (Miletich et al. 2000)	15

Figure 2.3. Schematic view of a synchrotron radiation source (Adapted from Mi et al., 2012)	17
Figure 2.4. Comparative illustration of the generation process of synchrotron light by a (a) bending magnet, by insertion devices (b) wiggler and (c) undulator. (Adapted from Mi et al., 2012)	18
Figure 2.5. Experimental setup of laser heating diamond anvil cell in at GSECARS, 13-ID-D, Advanced Photon Source (APS) of Argonne National Laboratory (a) Picture (b) Schematic diagram (Prakapenka,, 2008)	22
Figure 2.6. Schematic diagram of angular dispersive X-Ray diffraction technique	20
Figure 2.7. Layout of the Raman system used in this study for high pressure ruby fluorescence measurements	23
Figure 2.8. Unaligned and aligned DAC	26
Figure 2.9. Deformation of gasket under pressures during indentation; (a) Before deformation at low pressure; (b) After deformation at high pressure	27
Figure 2.10. Electronic drilling machine (EDM)	28
Figure 2.11. Gasket; (a) Rhenium gasket attached in the middle of steel gasket; (b) after indentation with DAC; (c) After drilling hole	29
Figure 2.12. Example of sample configuration for the radial X-ray diffraction study in a DAC	30
Figure.2.13. (a) 2-dimensional Xrd pattern collected by CCD, (b) After integration (c) Peak position determination using PeakFit	35
Figure 3.1. Synthesizing CaTi_2O_4 type structure of MgCr_2O_4	35
Figure 3.1. Synthesis of CaTi_2O_4 type structure of MgCr_2O_4	38
Figure 3.2. MgCr_2O_4 first dissociates to $\text{Cr}_2\text{O}_3+\text{MgO}$ about at 1200K and 16GPa, and then to $\text{Mg}_2\text{Cr}_2\text{O}_5+\text{Cr}_2\text{O}_3$ about at 1700K and 16GPa	39
Figure 3.3. Figure 3.3: Phase diagram of MgCr_2O_4 . Solid black lines represent the phase boundary from our LHDAC experiment. Dashed red lines represent the phase boundary reported by Ishii et al (2015)	43
Figure 4.1. Synthesis of CaTi_2O_4 type structure of magnesiochromite was decompressed from 45GPa to ambient conditions	47

Figure 4.2. Crystal structure of CaTi ₂ O ₄ -type MgCr ₂ O ₄ in b-c planes. Solid silver lines represent the unit cell. Blue spheres are Magnesium, green polyhedra are Chromium, and red spheres are Oxygen. (Structure adapted from Ishii et al., 2015)	48
Figure 4.3. Normalized pressure vs. Eulerian Strain plot of CaTi ₂ O ₄ type structure of MgCr ₂ O ₄	50
Figure 4.4. Equation of State of CaTi ₂ O ₄ type structure of MgCr ₂ O ₄	51
Figure 4.5. Variation of unit cell parameters with pressure (a) a-parameter variation with pressure (b) b-parameter variation with pressure (c) c-parameter variation with pressure (d) variation of unit cell dimensions [red circle (a/a ₀), Green rectangle (b/b ₀), Blue triangle (c/c ₀)] with pressure	52
Figure 5.1. Synthesis of Mg ₂ Cr ₂ O ₅ and Cr ₂ O ₃ phases was decompressed from 16GPa to ambient conditions	55
Figure 5.2. Crystal structure of modified ludwigite-type (mLd type) Mg ₂ Cr ₂ O ₅ phase in a-b plane. Solid silver lines represent the unit cell. Blue spheres are Magnesium, different shades of green spheres are Magnesium or Chromium with different probabilities, and red spheres are Oxygen. (Structure adapted from Ishii et al., 2015)	56
Figure 5.3. Equation of state of Cr ₂ O ₃ . Red circles are P-V data obtained from our sample, and solid red line is Birch-Murnaghan EOS fittings. Solid green curve is the Equation of State of Cr ₂ O ₃ determined by Dera et al (2011)	58
Figure 5.4. Normalized pressure vs. Eulerian Strain plot of Mg ₂ Cr ₂ O ₅ phase	59
Figure 5.5. Equation of State of MgCr ₂ O ₅ phase	60
Figure 5.6. Variation of unit cell parameters with pressure (a) a-parameter variation with pressure (b) b-parameter variation with pressure (c) c-parameter variation with pressure (d) variation of unit cell dimensions [red circle (a/a ₀), Green rectangle (b/b ₀), Blue triangle (c/c ₀)] with pressure	61
Figure 6.1. Synthesis of CaTi ₂ O ₄ type structure of natural chromite was decompressed from 40 GPa to ambient conditions	64
Figure 6.2. Equation of State of CaTi ₂ O ₄ type structure of natural chromite. Red circles are our P-V data and red line is the second order Birch-Murnagahan EOS fitting. Blue solid line is the EOS drawn by Ishii et al. (2015) for CaTi ₂ O ₄ type structure of FeCr ₂ O ₄ , and green solid line is the EOS of CaTi ₂ O ₄ type structure of MgCr ₂ O ₄ , which has been presented in chapter 4	66

Figure 6.3. Normalized pressure vs Eulerian Strain plot shows that the derivative of the bulk modulus (K_0') is actually 4 67

Figure 6.4. Variation of unit cell parameters with pressure (a) a-parameter variation with pressure (b) b-parameter variation with pressure (c) c-parameter variation with pressure (d) variation of unit cell dimensions [red circle (a/a_0), Green rectangle (b/b_0), Blue triangle (c/c_0)] with pressure 67

List of Appendices

Appendix A1. MgCr_2O_4 decomposed to $\text{Mg}_2\text{Cr}_2\text{O}_5$ and Cr_2O_3 at about 1500 K and 18 GPa	83
Appendix A2. Cr_2O_3 peaks showed up after reheating the synthesized CaTi_2O_4 type structure of MgCr_2O_4	84
Appendix A3. Calculated and observed peak positions of synthesised CaTi_2O_4 type MgCr_2O_4	85
Appendix A4. Calculated and observed peak positions of synthesised $\text{Mg}_2\text{Cr}_2\text{O}_5+\text{Cr}_2\text{O}_3$ and CaTi_2O_4 type MgCr_2O_4	86
Appendix A5. Laser heating spot on the sample from both sides	89
Appendix A6. Composition of different samples	89
Appendix A7. Ionic radius of different ions	90
Appendix A8. High pressure polymorphs of different spinel group minerals	90
Appendix A9. Interatomic distances and angles in the structures of CaTi_2O_4 (CT)-type MgCr_2O_4 and modified ludwigite (mLd)-type $\text{Mg}_2\text{Cr}_2\text{O}_5$ (Ishii et al., 2015)	91

List of Abbreviations

ADXN:	Angle dispersive X-ray diffraction
ANL:	Argonne National Laboratory
APS:	Advanced Photon Source
Ar:	Argon
Au:	Gold
Be:	Beryllium
BM:	Bending Magnets
BNL:	Brookhaven National Laboratory
BS:	Beam Splitter
CCD:	Charge-Coupled Device
Chr:	Chromite
CF:	CaFe ₂ O ₄
CT:	CaTi ₂ O ₄
DAC:	Diamond Anvil Cell
D-DIA:	Deformation Diamond
EDM:	Electronic Discharge Machine
EDXD:	Energy Dispersive X-ray Diffraction
Fp:	Ferropericlas
FWHM:	Full Width at Half Maximum
GPa:	Giga-Pascal
HP:	High Pressure
HT:	High Temperature
ID:	Insertion device
IR:	Infrared
KB:	Kirkpatrick-Baez (a kind of mirror)
LHDAC:	Laser Heating Diamond Anvil Cell
LP:	Low Pressure
LT:	Low Temperature

mLd: Modified Ludwigite
Ne: Neon
NF: Notch filter
NSLS: National Synchrotron Light Source
PTM: Pressure transmitting medium
RDA: Rotation Drickamer Apparatus
rf: Radio frequency
RHDAC: Resistive Heating Diamond Anvil Cell
XRD: X-ray Diffraction

List of Symbols

c : Speed of light

E : Energy

m : Mass

I : Intensity

h : Planck constants

ϵ : Emissivity

λ : Wavelength

T : Temperature

d : Spacing of lattice planes

θ : Angle of specular reflection

B : Curvature parameter

P : Pressure

m : Mass

M : Mass

ϵ : Strain

f : Eulerian strain

F : Normalized pressure

R : Gas constant

N : Number of moles

T: Temperature

K: Bulk modulus

K_0' : pressure derivative of the bulk modulus

V: Volume

ρ : Density

Chapter 1

1. Introduction

1.1. The Spinel Structure

A spinel mineral is a molecular compound with the formula $(A)[B_2]O_4$, A and B being metal ions with valences of 2+ and 3+ respectively. Spinel compounds are known to crystallize into a cubic structure with the space group $Fd\bar{3}m$ (O'Neill & Navrotsky, 1983; O'Neill & Navrotsky, 1984). Two kinds of spinel structures that exist at ambient conditions are normal $\{(A)[B_2]O_4\}$ and inverse $\{(B)[AB]O_4\}$ spinels. In the normal spinel A and B ions inhabit the tetrahedral (T) and octahedral (M) sites respectively, while in the inverse spinel half of B ions center the fourfold coordination, leading to relocation of all the A ions to octahedral sites (Hazen, 1999; Levy et al., 2000). In order to completely describe the spinel structure geometry, one has to define the cell parameters and atomic position. An illustration of the spinel structure is presented in Figure 1.1.

Spinel may be synthesized in the laboratory and also occur as minerals. Some of the principal members of the oxide spinel family are: spinel ($MgAl_2O_4$), gahnite ($ZnAl_2O_4$), hercynite ($FeAl_2O_4$), cuprospinel ($CuFe_2O_4$), magnetite (Fe_3O_4), ulvöspinel ($TiFe_2O_4$), chromite ($FeCr_2O_4$), magnesiochromite ($MgCr_2O_4$), galaxite ($MnAl_2O_4$), magnesioferrite ($MgFe_2O_4$), franklinite ($ZnFe_2O_4$), trevorite ($NiFe_2O_4$), and the high-pressure silicate ringwoodite $[(Mg, Fe)_2SiO_4]$. Spinel is usually of normal type, however mutual substitution of A and B cations has been reported in many materials. The extreme cases of cation substitution lead to “inverse” spinels such as $CoFe_2O_4$, where the Co cation occupies half of the octahedral sites and the Fe cation occupies all the tetrahedral sites. In general most spinels have some degree of inversion. A particular case is $NiAl_2O_4$, which displays a complete randomization of both cations in octahedral and tetrahedral sites.

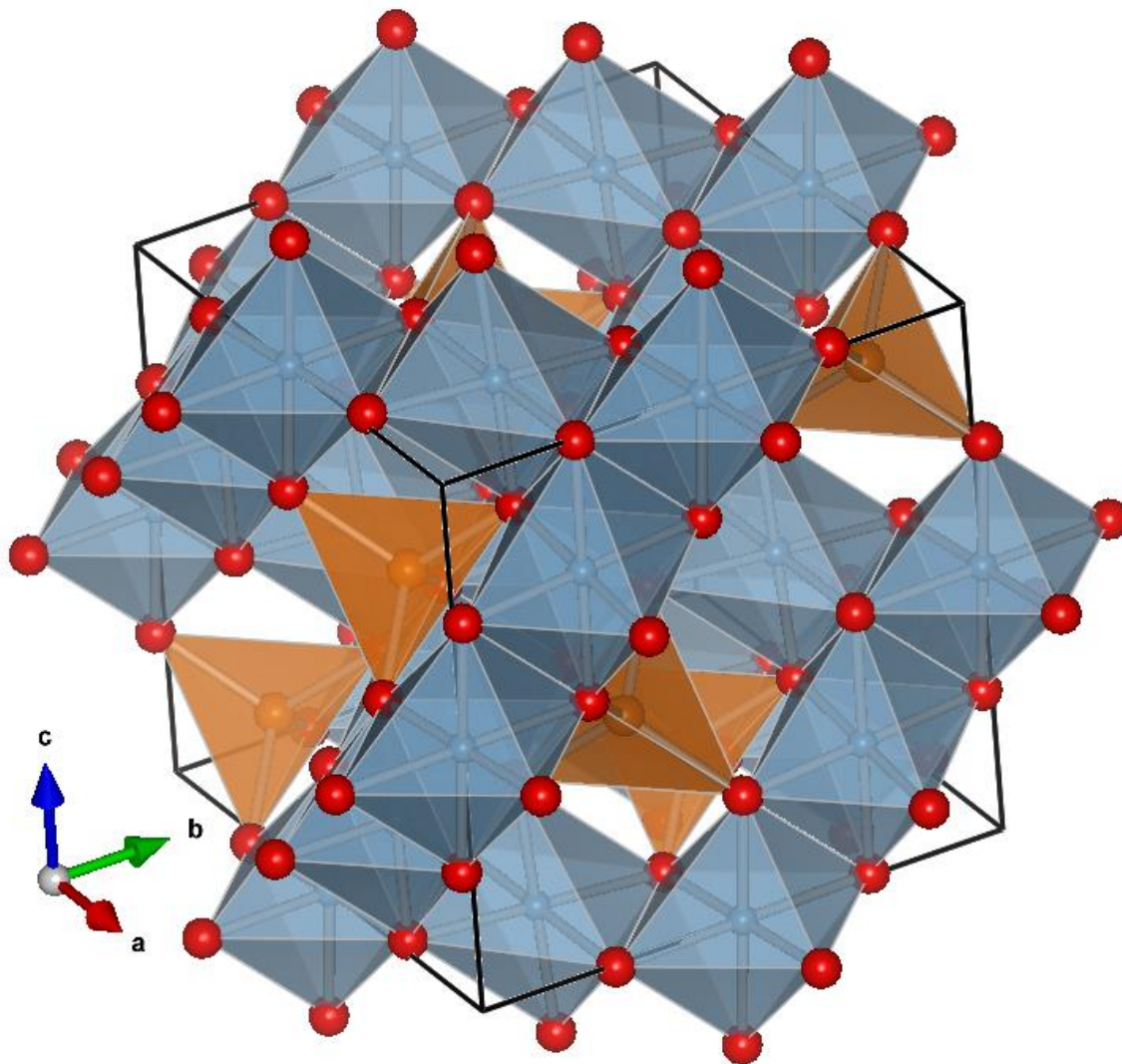


Figure 1.1: The spinel structure. Red spheres are “Oxygen”, Gold spheres are “A-atom”, and Blue spheres are “B-atom”. Solid black line represents the boundary of unit cell. (Structural data from Yamanaka et al., 1983)

Ever since Finger and colleagues (1986) studied the structure of spinel and magnetite at pressure up to 4 GPa, their report attracted much attention and many similar work on high-pressure spinel studies have been performed. The motivation to study these materials comes not only from geophysics, but also from technological applications and fundamental physics. In particular, spinel oxides have been widely studied under pressure because these are constituents of many igneous and metamorphic rocks and because the 660 km seismic discontinuity inside earth's

mantle has long been recognized with the decomposition of ringwoodite into (Mg, Fe)SiO₃ perovskite and (Mg, Fe)O magnesiowüstite (Hazen et al., 2000).

This class of structures exists in large quantities in the Earth's transition zone. It plays a significant role in describing the physical properties of our planet (Boehler, 2000). Olivine transforms to wadsleyite at high temperature and high pressure, in the environment of below 410 km deep earth mantle. At higher pressure and temperature environment, corresponding to >520 km deep mantle of earth, wadsleyite transforms into ringwoodite, which has the spinel structure (Chudinovskikh & Boehler, 2001). The formula of olivine, Mg₂SiO₄, can be rewritten as SiMg₂O₄, with Si assuming the role of an A cation and Mg the role of a B cation.

Spinel is also very important in materials science. These are binary oxides, which occur in numerous industrial processes and have important technological applications. Petric and Jacob (1982) reported that spinels are formed as stable corrosion products when alloys are exposed to an oxidizing environment. Spinel provides a protective layer between the alloy and gas, preventing further corrosion. Additionally, owing to their favorable electrical properties, certain spinels have been considered as candidate materials for magneto hydrodynamic electrodes and as promising materials (especially LiMn₂O₄) as cathode for Lithium batteries (Malavasi et al., 2005). Spinel is also used as catalysts for the decomposition of chlorinated organic pollutants (Kim & Ihm, 2001), as magnetic materials (Martinho et al., 2001), super hard materials (Zerr et al., 1999), high temperature ceramics (Kim et al., 2001) and as high pressure sensors (Jahren et al., 1992).

Due to their importance in geosciences, physics, materials science, and crystallography, properties of spinel compounds have been explored extensively. A great number of studies have been performed to find the pressure-induced phase transformations in spinel-type structures (Ringwood & Ried, 1969; Irifune et al., 1991, Catti et al., 1999; Levy et al., 2000; Haavik et al., 2000; Shim et al., 2001; Wang et al., 2002; Ono et al., 2006). Two types of high pressure behaviors have been reported: one involving a pressure-induced phase transformation from spinel structure to high pressure polymorph; and the other involving dissociation to a mixture of constituent oxides. High pressure and high temperature (HP-HT) study of MgAl₂O₄ by Ono et al.

(2006) reveals the transformation of cubic MgAl_2O_4 to several new phases at different pressure and temperature conditions (Figure 1.2). Other studies involve determining equations of state for numerous spinels (Irifune et al., 2002; Wang et al., 2003; Speziale et al., 2004) and performing theoretical calculations in aim of describing this wide array of structures (Catti et al., 1999).

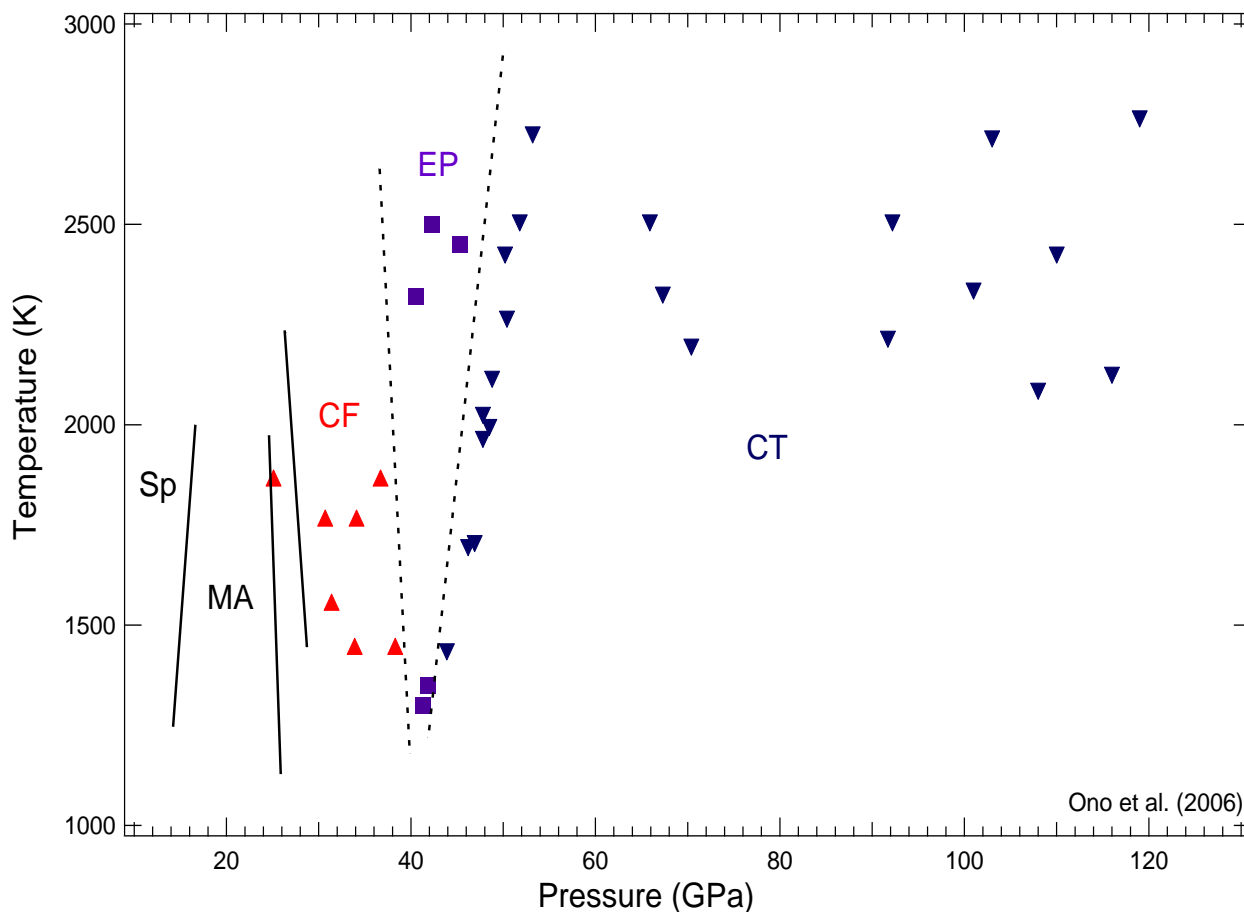


Figure.1.2: Phase diagram of MgAl_2O_4 reported by Ono et al. (2006). SP=Spinel-type, MA= $\text{MgO}+\text{Al}_2\text{O}_3$, CF= CaFe_2O_4 -type MgAl_2O_4 , EP= ϵ -type MgAl_2O_4 , CT= CaTi_2O_4 -type MgAl_2O_4

1.2. Chromite Spinel

Chromites are molecular compounds with the general formula ACr_2O_4 and have a normal type spinel structure (Romeijn, 1953; Miyahara & Ohnishi, 1956). The tetrahedra of oxygen atoms

surround divalent metal ions and the octahedra of oxygen surround chromium ions (Sawaoka et al., 1971). The divalent metals ions can be Fe, Mg, Zn or Mn. The chromite structure is similar to the spinel structure presented in Figure 1.1, where the yellow spheres are chromium ions and gold spheres are magnesium ions.

Chromite spinel $[(\text{Mg}, \text{Fe}, \text{Al})\text{Cr}_2\text{O}_4]$ is a common mineral in many meteorites (Rubin, 1997). More importantly, it has a high resistance against weathering & diagenesis and is often the only mineral surviving in fossil meteorites (Thorslund et al., 1984). By studying in the shock veins of the Suizhou meteorite (Figure 1.3), Chen et al. (2003a, 2003b) reported that chromite spinel (56–57 wt.% Cr_2O_3 , 29 wt.% FeO , and small amounts of Al_2O_3 , MgO , TiO_2 , MnO and V_2O_3) transforms to the CaFe_2O_4 (CF) type structure at 12.5 GPa and to the CaTi_2O_4 (CT) type structure above 20 GPa. The Suizhou meteorite is an L6 chondrite with shock classification stage as S3 to S4 (Xie et al., 2001, 2002), which fell in Dayanpo, in the southeast of Suizhou in Hubei, China, on April 15, 1986.

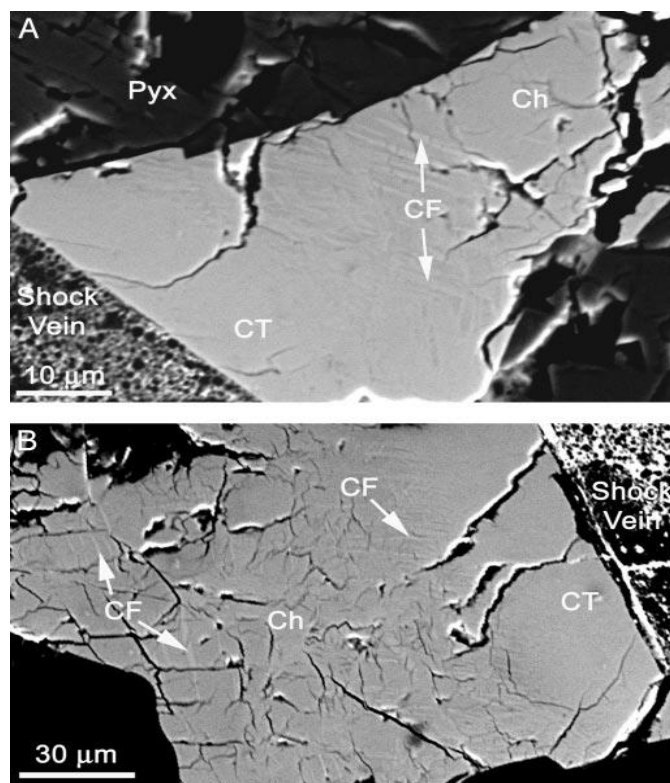


Figure 1.3: High-pressure polymorphs of chromite first reported by Chen et al. (2003), by studying in the shock veins of the Suizhou meteorite

Yamamoto et al. (2008) found numerous exsolution lamellae of diopsidic clinopyroxene and coesite in podiform chromitites from the Luobusa ophiolite. They were explained by the association of high pressure minerals (diamond, clinopyroxene and coesite) with chromites in the podiform chromitites of the Luobusa ophiolite by the inverse transformation from CT/CF-phase to chromite by a mantle upwelling process (Yang et al., 2007, Yamamoto et al., 2009, and Arai, 2010 & 2013). It is necessary to incorporate SiO_2 and CaO components in the host chromite or its precursor, for occurrence of diopsidic clinopyroxene and coesite exsolution lamellae in chromite. But natural chromite contain only 0.6 wt.% of SiO_2 and the CaO content is less than several tens of ppm (Arai and Yurimoto, 1994). But MgCr_2O_4 -rich CF/CT-phases can contain Ca, Si, Ti, and Fe as CaFe_2O_4 and CaTi_2O_4 solid solutions (Chen et al., 2003a, 2003b). This indicates the possibility of presence of high pressure polymorph of chromite spinel in deep earth mantle.

Spinel was reportedly found in lunar rocks (Figure 1.4), and magnesiochromite spinel is one of the highly plausible candidate (Cloutis et al., 2004, Pieters et al., 2011).

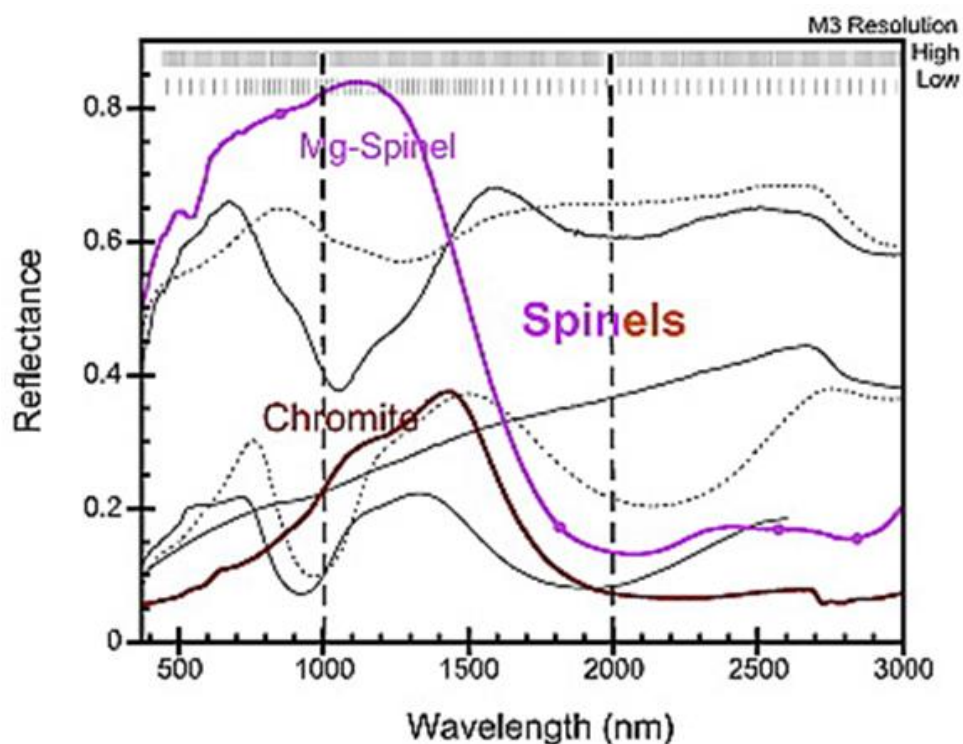


Figure 1.4: Reflectance spectra of spinels (Cloutis et al., 2004). Gray spectra in background are the common lunar minerals.

Chromite is commonly associated with olivine, serpentine, magnetite and corundum. Inclusions of chromite-magnesiochromite ($\text{FeCr}_2\text{O}_4\text{-MgCr}_2\text{O}_4$) solid solutions, in particular, magnesiochromite is among the most common inclusion in diamonds from the cratonic lithosphere (Stachel & Harris, 2008; Griffin & Ryan, 1995; Bulanova, 1995). The chemical analysis of spinels included in diamonds reported by Lenaz et al. (2009) showed that the most abundant component is magnesiochromite (magnesiochromite + chromite reach about 90%) followed by chromite and hercynite (6-7%).

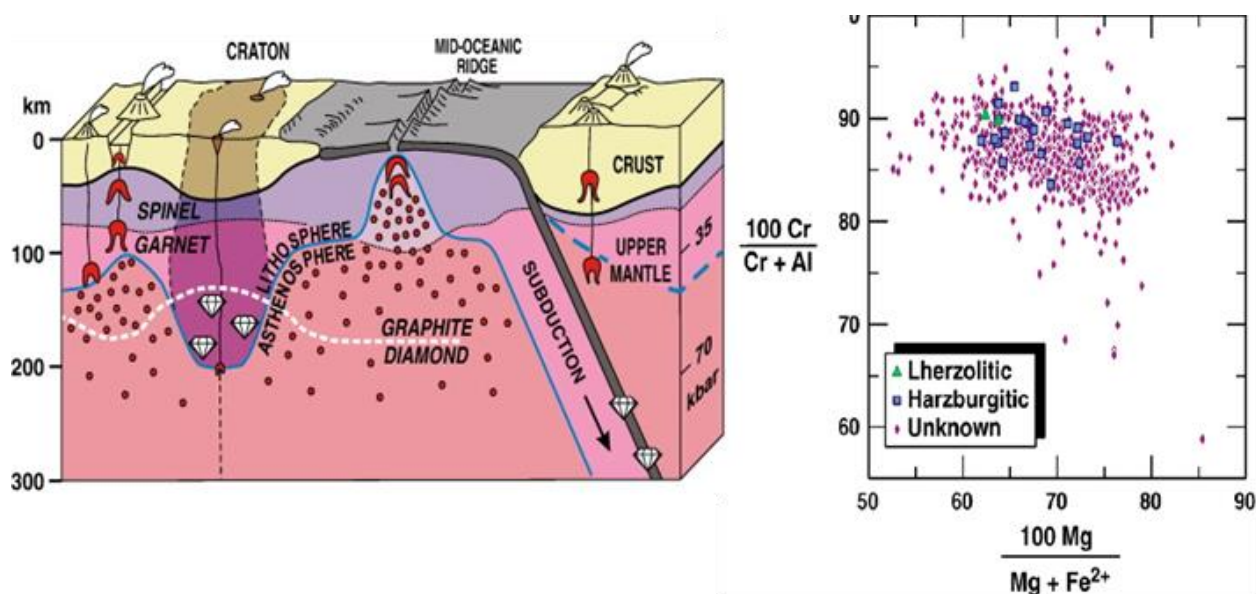


Figure 1.5: Spinel with Cr-numbers of at least about 80 is stable in cratonic Lithosphere (Stachel and Harris 2008)

Chromium bearing spinels $[(\text{Mg}, \text{Fe})\text{Cr}_2\text{O}_4]$ are found in peridotite from the Earth's mantle. It also occurs in layered ultramafic intrusive rocks (Gu and Wills 1988). In addition, it is found in metamorphic rocks such as some serpentinites. Ore deposits of chromite form as early magmatic differentiate. It is commonly associated with olivine, magnetite, serpentine, and corundum. Although typically present as accessory phases, chromium bearing spinels are widely considered to be important petrogenetic indicators (Irvine 1965, 1967; Evans and Frost 1975; Sack and Ghiorso 1991; Bosi et al. 2008), and can target a certain regions in garnet lherzolite for diamond exploration (Griffin and Ryan 1995, Stachel and Harris 2008). Chromium spinels present compositional variations and order-disorder modifications related to the petrologic processes in

which they are involved (Perinelli et al. 2014). Chromium spinels are stable over a wide range of temperatures and pressures in the Earth upper mantle. Besides Cr, the equilibrium inter-crystalline exchange of Mg^{2+} and Fe^{2+} cations has been intensely analyzed, and revealed its great potential to be used as geothermometer in rocks containing the paragenesis olivine-spinel (Fabries, 1979; Ballhaus, 1990). Chromium bearing spinels being the only commercial ore of chromium (Duke, 1983) is also important in materials science. Chromium is used in stainless steel, nichrome and chrome plating. Chromites are also used in the production of ferrochrome (an important alloying agent in preparing stainless steel) (Arvanitidis et al., 1996), metallic chromium, chromium chemicals, and refractories (Tathavadkar et al., 2005).

Due to their importance in geosciences, physics, materials science, and crystallography, properties of chromium bearing spinels have been explored extensively both theoretically and experimentally. Ab initio calculation has been performed by Catti et al. (1999) to examine the phase transformation of chromites. The simulation shows that the chromite can dissociate to constituent oxides at high pressure and room temperature. Wang et al. (2002) first studied the magnesiochromite ($MgCr_2O_4$) spinel at high pressure with raman and reported that this spinel begins undergoing a phase transformation to $CaFe_2O_4$ (CF) or $CaTi_2O_4$ (CT) structure at 14.2 GPa. The complete transition take place at 30.1 GPa (Figure 1.6).

However, the transformation of magnesiochromite to CF or CT phase was not supported by a more recent study by Yong et al. (2012). Instead, a polymorphic phase transition from cubic structure to tetragonal structure was reported for magnesiochromite at 23.5 GPa and room temperature (Figure 1.7) and at a much lower pressure (12 GPa) for iron-chromite (Kyono et al., 2012).

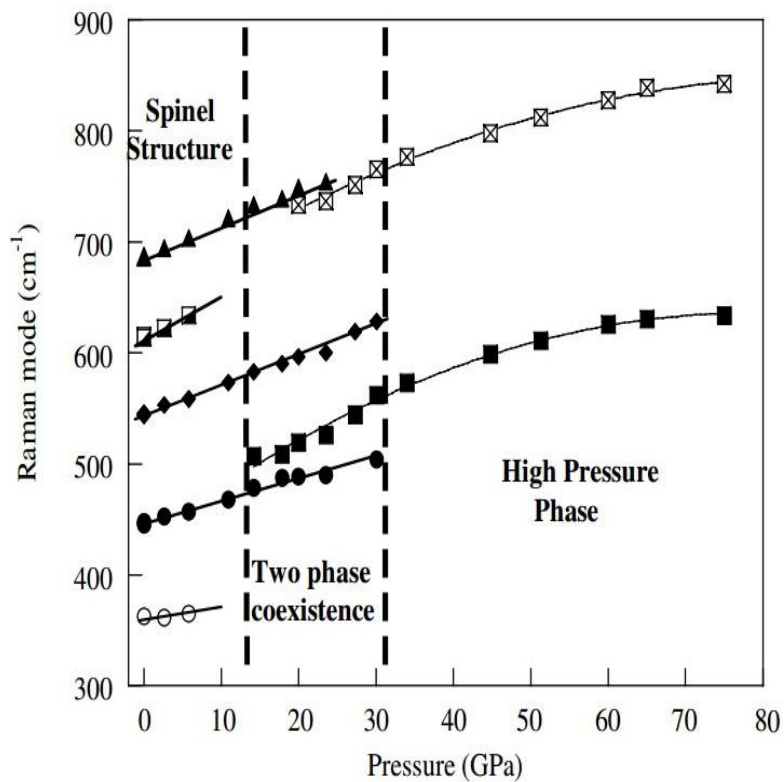


Figure 1.6: Phase transformation of Magnesiochromite by Raman study (Wang et al., 2002)

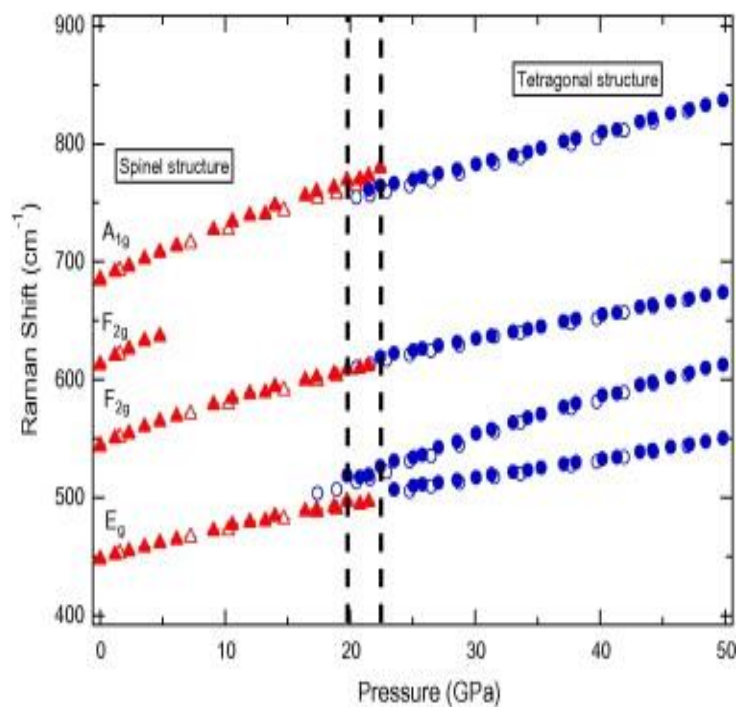


Figure 1.7: Phase transition from cubic structure to tetragonal structure of magnesiochromite (Yong et al., 2012)

A recent synthesis study on chromite (FeCr_2O_4) by Ishii et al. (2014) showed that chromite dissociates at 12-16 GPa to $\text{Cr}_2\text{O}_3 + \text{Fe}_2\text{Cr}_2\text{O}_5$, and is then transformed to CF and CT type structure at 17-18 GPa below and above 1300°C, respectively (Figure 1.8).

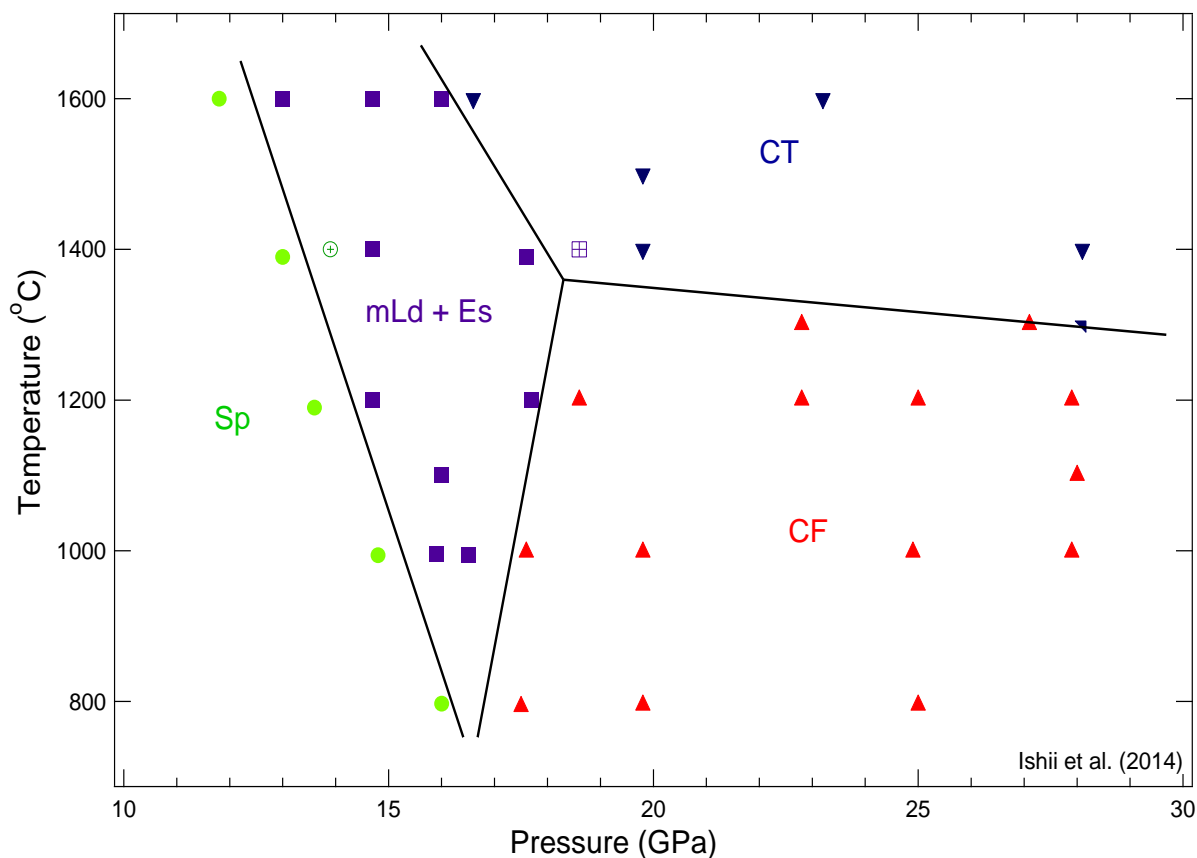


Figure 1.8: Phase diagram of FeCr_2O_4 at HP-HT. Solid lines represent phase boundaries. Sp = spinel-type FeCr_2O_4 ; mLd = modified ludwigite-type $\text{Fe}_2\text{Cr}_2\text{O}_5$; Es = Cr_2O_3 eskolaite; CF = Ca Fe_2O_4 -type FeCr_2O_4 ; CT = Ca Ti_2O_4 -type FeCr_2O_4 . (Ishii et al. 2014)

Another recent synthesis study on magnesiochromite (MgCr_2O_4) by Ishii et al. (2015) showed a different behavior. Magnesiochromite dissociates into a mixture of new modified ludwigite-type $\text{Mg}_2\text{Cr}_2\text{O}_5$ phase + corundum-type Cr_2O_3 at 1100–1600°C, but it decomposed first into MgO periclase + corundum-type Cr_2O_3 at 1000°C at 12-15 GPa. At about 17–19 GPa, the mixture of $\text{Mg}_2\text{Cr}_2\text{O}_5$ phase + corundum-type Cr_2O_3 transforms to a Ca Ti_2O_4 type single MgCr_2O_4 phase (Figure.1.9). Ishii et al. (2015) didn't find any trace of Ca Fe_2O_4 type structure of MgCr_2O_4 .

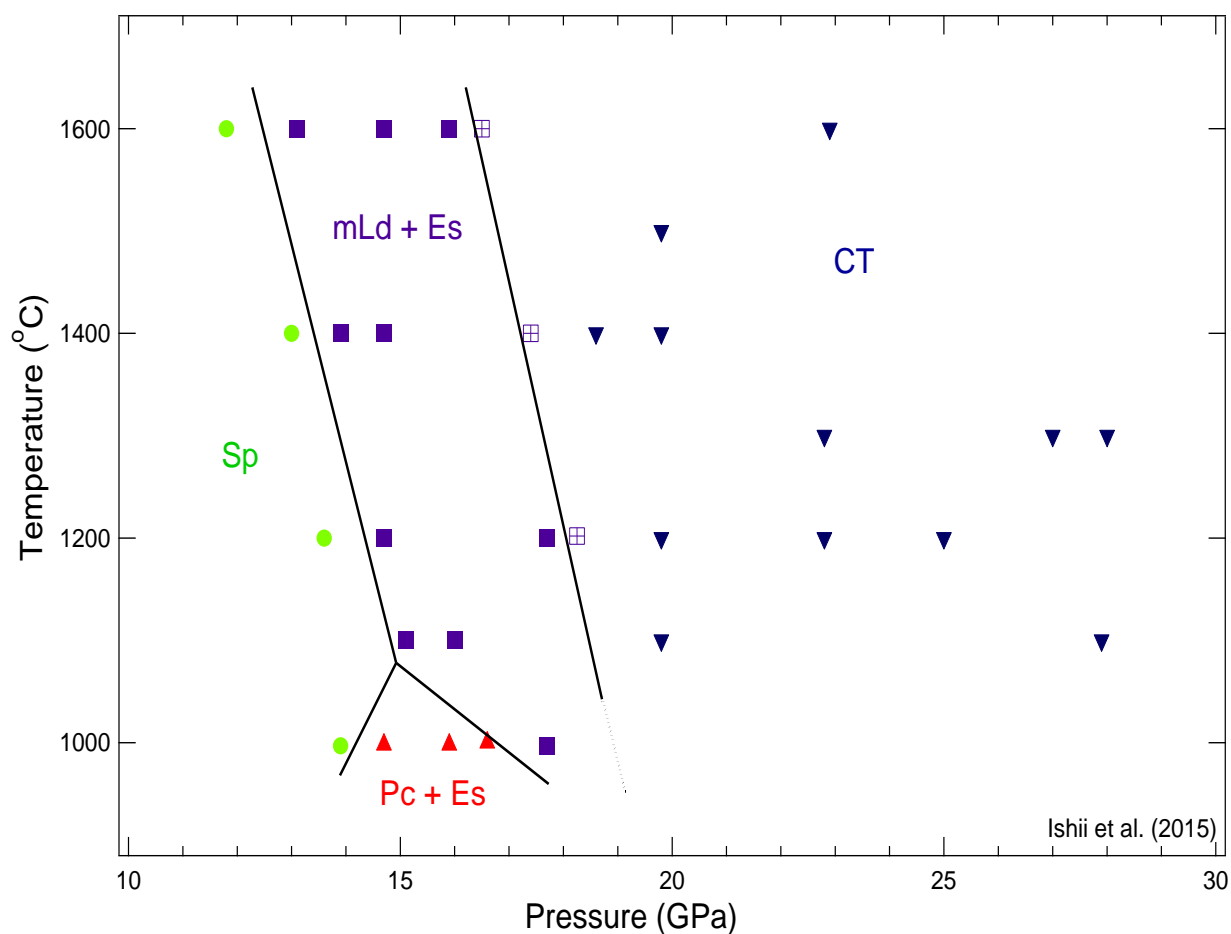


Figure 1.9: Phase diagram of MgCr₂O₄ at HP-HT. Solid lines represent phase boundaries. A dashed line represents the extrapolated transition boundary of mLd + Es to CT. Sp = spinel-type MgCr₂O₄; mLd = modified ludwigite-type Mg₂Cr₂O₅; Es = corundum type Cr₂O₃ eskolaite; CT = CaTi₂O₄-type MgCr₂O₄; Pc = rocksalt-type MgO periclase. (Ishii et al, 2015)

1.3. Objective of the thesis

The high pressure and high temperature (HP-HT) polymorphs of spinel series could potentially provide a comprehensive pressure gauge and geothermometer system over an extended range considering the presence of the spinel minerals in the earth's mantle and in extraterrestrial bodies, their extensive range of composition, their composition dependence of the transition pressure and temperature. A systematic and careful HP-HT experimental study of magnesiochromite (MgCr_2O_4) has been performed with double sided laser heating diamond anvil cell incorporated with synchrotron X-ray radiation in order to establish the reliable phase diagram.

A study of the equations of state of high pressure polymorphs of chromite spinel is also essential in geophysics for a better understanding of the mechanical and thermal state of the mantle. So, besides constructing the phase diagram of HP-HT polymorphs of magnesiochromite spinel, we have also determined the P-V equation of state (EOS) of all the traceable HP-HT polymorphs of magnesiochromite and one HP-HT polymorphs of natural chromite. This is the first step to determine the P-V-T equation of state of chromium bearing spinels. This would help with the calculation of density and bulk wave velocity over a wide range of P-T conditions and determination of depth dependence of important thermo-elastic parameters such as thermal expansivity and temperature sensitivity of bulk modulus.

Chapter 2

2. Experimental Method

2.1. Experiments and Instruments

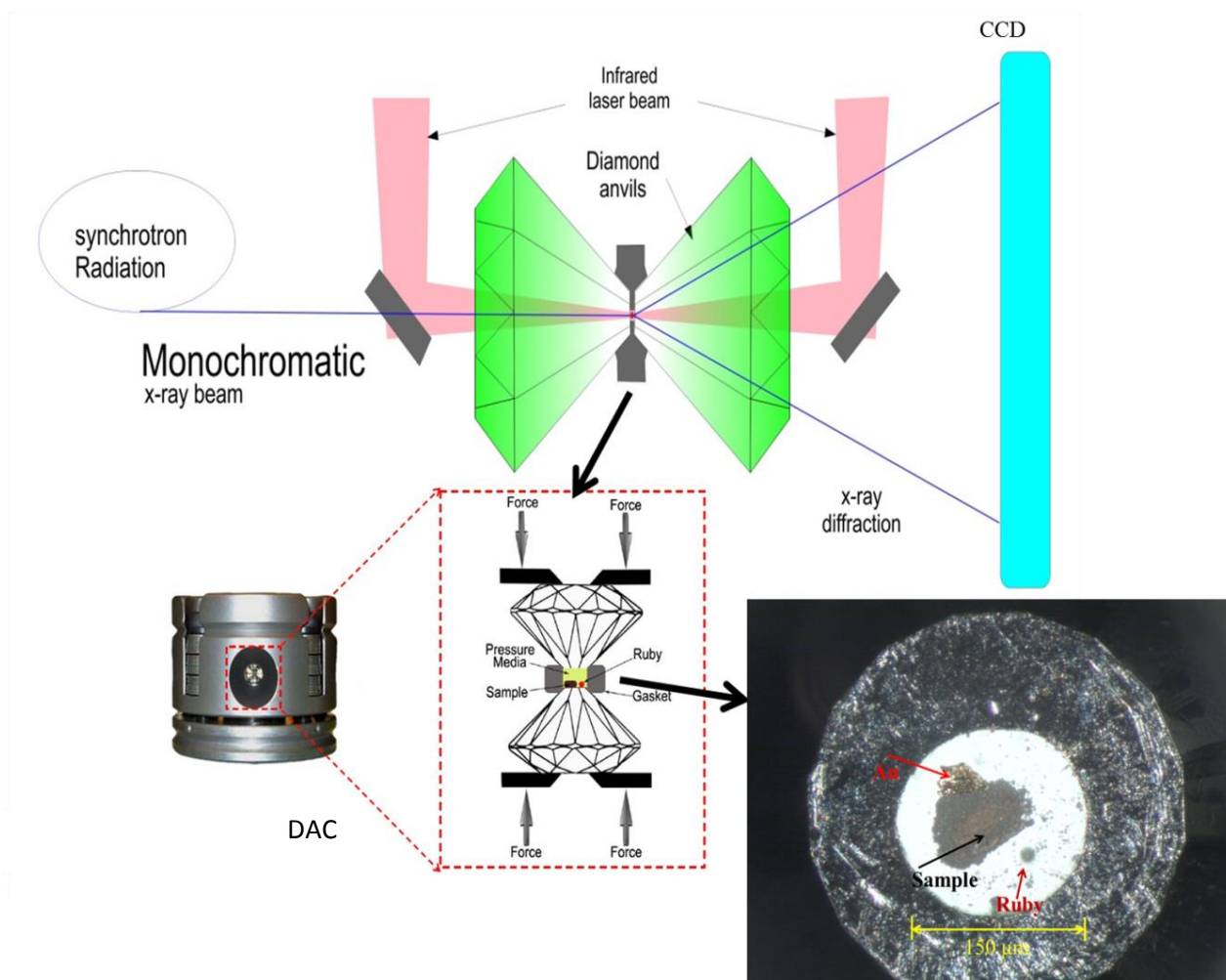


Figure 2.1: Experimental Setup of laser heated diamond anvil cell incorporating with synchrotron XRD.

High pressure and high temperature experiments were performed at GSECARS, 13-ID-D, Advanced Photon Source (APS) of Argonne National Laboratory (ANL) and at X17B3, National

Synchrotron Light Source (NSLS) of Brookhaven National Laboratory (BNL) using a diamond anvil cell (DAC). Double-sided laser heating method was employed with synchrotron X-ray diffraction in this study. Laser heating was used to heat the sample inside DAC to synthesize new phase and to study phase transformation at high pressure and high temperature. In this chapter, basic principles of DAC, fundamentals of synchrotron radiation, powder X-ray diffraction and theory of Raman spectroscopy and experimental methods are introduced. Figure 2.1 shows the schematic of the experimental setup.

2.2. The Diamond Anvil Cell

In high pressure science, we can generate pressure using two methods (a) dynamic and (b) static compression. While static compression uses a piston-cylinder mechanism, multi-anvil press and diamond anvil cell (DAC) and dynamic compression uses the shock wave method. The advantages of DAC are high transparency to a wide range of electromagnetic radiation, ability to visually observe the pressure effects and high strength to produce ultra-high pressures above 400 GPa (4 Mbar) (Ruoff et al., 1990), attaining the pressure range found in earth's deep interior.

There are various types of DACs, such as the Mao-Bell type, Merrill-Bassett cell, and custom-made symmetric DAC. In this study, symmetric DACs were adopted for different experiments and the geometry is shown in Figure 2.2. To prepare the diamond anvil cell for the experiments, firstly. Two diamonds are mounted onto two tungsten carbide seats corresponding to piston and cylinder of the DAC. Pressure is produced by mechanically tightening four screws to force two diamonds opposing each other thereby compressing the sample between two diamonds. The force required even for the highest attainable pressure is not large due to a small culet size of diamond. The culet size of diamond anvil determines the highest pressure it can attain. Normally, smaller the size higher the attainable pressure is.

Due to their ability to generate high pressures, diamonds are the most important components in a DAC. The rest of the cell serves to align the working tips, maintain this alignment under loading and sustain the load. Thus, it is vital to know the properties of diamonds to select the correct diamonds for various experiments. Generally, the diamonds are classified into two main types.

The type I diamonds contain mainly nitrogen atoms as their impurity, commonly at a concentration of 0.1%. On the other hand, type II diamonds have no measurable nitrogen impurities. A further subdivision categorizes diamonds into type Ia having isolated nitrogen atoms; type Ib having aggregated nitrogen atoms; type IIa being clear diamonds and type IIb having boron impurities. Type I diamonds have two strong absorption regions in infrared (IR) spectra, which are around 2000 cm^{-1} and $1000\text{-}1350\text{ cm}^{-1}$. Type II diamonds have a clean spectrum below 2000 cm^{-1} allowing IR measurements of the sample inside DAC. Therefore, type I diamonds are suitable for Raman spectroscopy, while type II diamonds are good for IR spectroscopy. At very high pressures, it has been established that type I diamonds with platelet nitrogen aggregates are more resilient to plastic deformation and therefore can constitute the best anvil material for diamond anvil cells functioning in very high pressure (Mao et al., 1979).

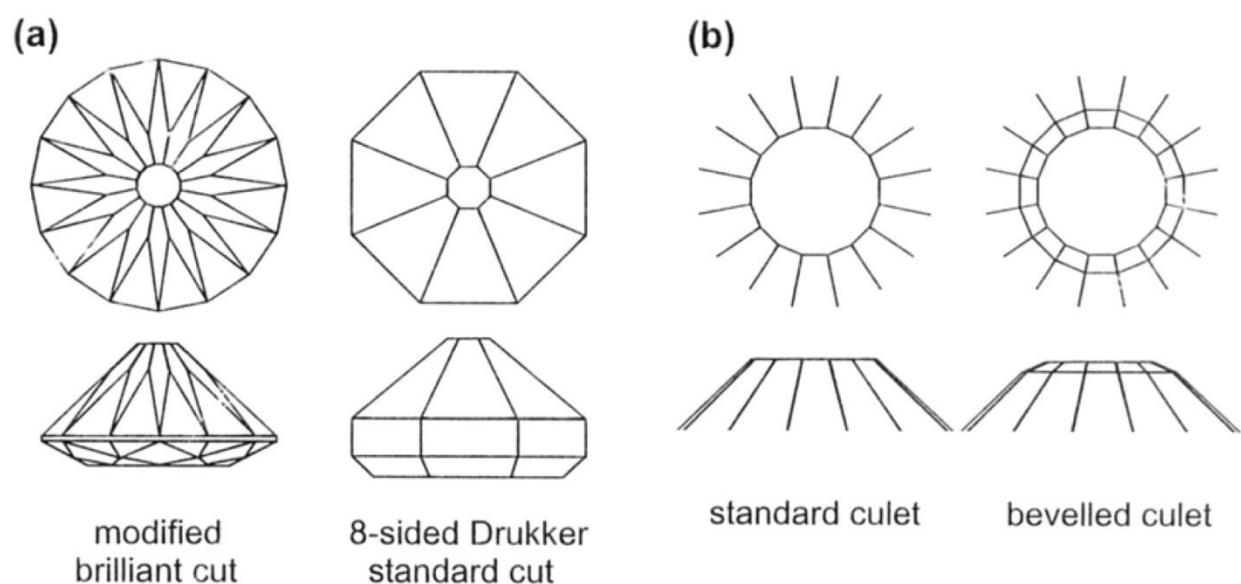


Figure 2.2: (a) Shapes of diamond anvils (b) culet designs (Miletich et al. 2000)

The design of anvil is crucial to determining the maximum pressure a DAC can achieve. Generally, two types of cutting are widely used: the modified brilliant cut and the Drukker cut (Figure 2.2). When compared to a brilliant cut diamond, the Drukker cut diamond has an enlarged table area and an increased anvil angle with the absence of highly stressed shoulders. These modifications can strengthen the diamond anvil and help sustain greater applied loads. Bevelled culets diamonds are usually suitable to work at very high pressures (Mao and Bell,

1978). The advantage of a beveled culet is that the stress concentrations at the edges of the culet are reduced; also the support by the gasket in culet is optimized (Bruno and Dunn, 1984). In this study, type Ia diamonds with Drukker cuts and standard culet were employed for synchrotron X-ray diffraction and Raman spectroscopy.

Another important component of DACs is the gasket. Without the gasket, DAC fails at around 10 GPa (Eremets, 1996). The gasket with a hole in the center serves as a sample chamber, building a lower pressure gradient and supporting the tips of the anvils. Different types of gaskets made of stainless steel, tungsten, rhenium, beryllium, boron-epoxy, etc. are used in different types of experiments. In this study, rhenium gaskets were employed in synchrotron X-ray diffraction experiments because of their high strength properties, while stainless steel gaskets were applied for moderate pressure range experiments conducted in-house Raman spectroscopy.

2.3. Synchrotron X-ray Radiation

When charged particles travel in a curved orbit at relativistic speeds, their tangentially emitted electromagnetic radiation is called ‘Synchrotron Radiation’. This radiation covers a wide range of wavelengths with extremely high intensity. It ranges from the infrared to visible and ultraviolet, as well as ranging into the soft and hard X-ray of the electromagnetic spectrum. Ever since its initial discovery at a General Electric (GE) laboratory in 1947 (Elder et al., 1947), synchrotron radiation has become a premier research tool for the study of matter in all varied manifestations, and has been quickly developed from first generation to the fourth. A synchrotron facility (Figure 2.3) is mainly composed of parts described below.

An electron gun generates a large number of free electrons. Electrons are then accelerated by a Linac function to a speed close to the speed of light, followed by a process called injection which involves injecting electrons into a vacuum chamber. Such a vacuum metal chamber is called a booster ring and it circulates the speedy electrons inside a metal tube. The radio frequency cavity system (RF) acts on circulating electrons and restores the energy lost through emission of electromagnetic radiation. The bending magnets force the electrons to circulate in a closed orbit by bending the course of the electrons. The insertion devices, such as wigglers and undulators,

are introduced into straight sections of the storage ring and further modify electron trajectories from straight line thereby inducing emission of further synchrotron radiations. The focusing magnets keep the electrons within a narrow range of the defined path with additional fine tuning of the electron beam trajectory. The beam, which is electromagnetic radiation, exits into the user's experimental chambers.

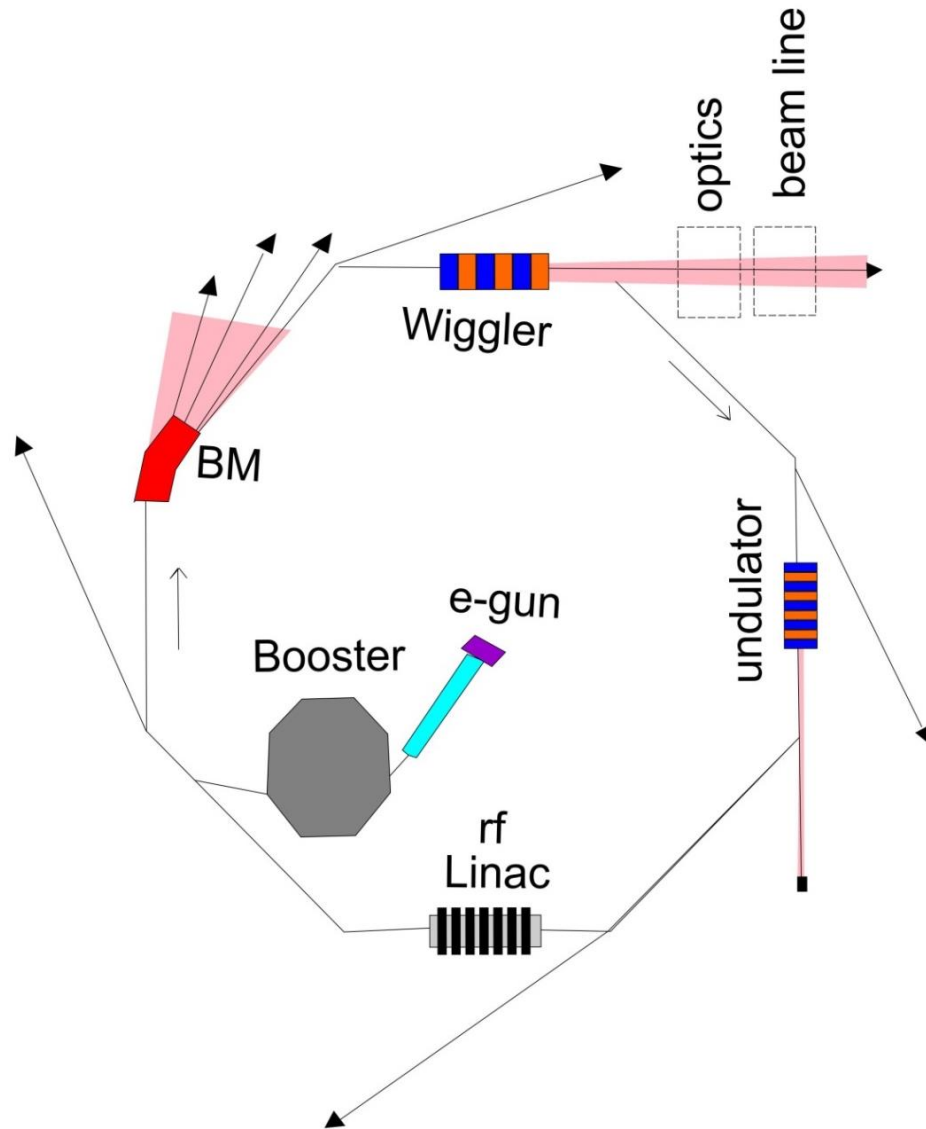


Figure 2.3: Schematic view of a synchrotron radiation source (Adapted from Mi et al., 2012).

A bending magnet produces a fan of radiation in the horizontal plane, like the sweeping of a search light. Several spatially separated experimental stations can be installed using one bending magnet, each using a different part of the fan of radiation. Wigglers and undulators are periodic

devices, consisting of a series of magnets with alternating polarities, which cause the electrons to curve back and forth. Therefore, the insertion devices can increase the intensity and brightness of the bending magnet radiation by up to 10 orders of magnitude.

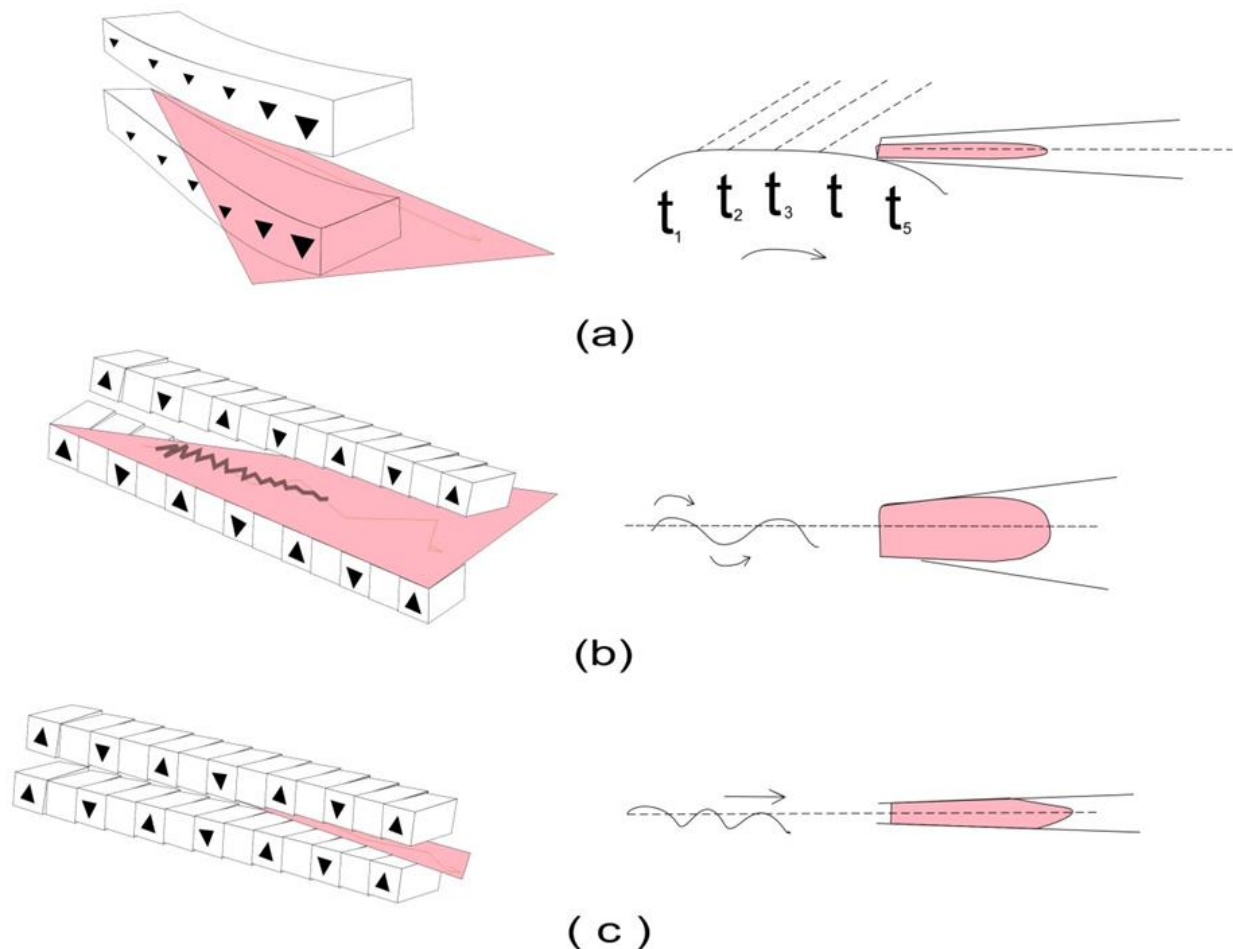


Figure 2.4: Comparative illustration of the generation process of synchrotron light by a (a) bending magnet, by insertion devices (b) wiggler and (c) undulator. (Adapted from Mi et al., 2012).

The radiations emitted by successive wiggler magnets do not interfere with each other and the total flux from a wiggler is the sum of emissions from each magnet. Thus, the wiggler generates incoherent radiation with a large angle, allowing several branch lines to operate simultaneously by sharing a small portion of the radiation. However when compared to wiggler magnets, the undulator has a smaller angle of deflection of electron trajectory from the straight line compared

to mc^2/E (m: mass; c: speed of light; E: energy) and the emissions from successive magnets retain coherence and interfere with each other. This interference enhances the intensity in certain regions of wavelengths at the expense of other regions and with the use of sufficient number of magnets. The spectrum becomes concentrated to a single or a few narrow, strong lines. For this reason, radiation from an undulator device can be used by only one station at a time. The flux comparison for bending magnet, wiggler and undulator is shown in Figure 2.4.

Synchrotron radiation provides a very powerful tool to many scientific fields such as physics, biology, chemistry, Earth sciences, material science, biology and medical science. The extraordinary properties of synchrotron radiation include: 1) the extremely high intensity enables a quick and accurate measurement; 2) the high collimation ensures a great resolution in measurement due to its spatial precision. This advantage especially benefits high pressure DAC studies due to small sample sizes; 3) the continuous spectrum makes it possible to conduct experiments with either white beam radiation or monochromatic light. Due to these significant advantages, synchrotron radiation source has been especially suitable for studying materials in small amounts and/or under extreme conditions.

2.4. Laser heating

The sample was heated by using double- sided laser heating facility (Figure 2.5) at GSECARS, 13-ID-D, Advanced Photon Source (APS) of Argonne National Laboratory.

The temperature of the laser heated spot was measured by using the light emitted from the heated spot which was fed into a spectrograph; the resulting intensity-vs.-wavelength curve was then fit to the Planck radiation function:

$$I = c_1 \cdot \varepsilon \cdot \lambda^{-5} / (\exp(c_2 / \lambda \cdot T) - 1) \quad (\text{Eq: 2.1})$$

Where I is intensity, c_1 and c_2 are constants, ε is emissivity, λ is the wavelength and T is temperature. A graph of $\ln(I \cdot \lambda^5)$ vs λ^{-1} was then constructed, which must be a straight line below ~4000 K if the calibration is good. Temperature of the heating spot is simply the slope of

the curve. The lasers and temperature measurement system should be well aligned with the x-ray beam for temperatures to be correlated with x-ray diffraction patterns. Shen et al. (2001, 2005) and Prakapenka et al. (2008) described in detail about the laser heating system in APS.

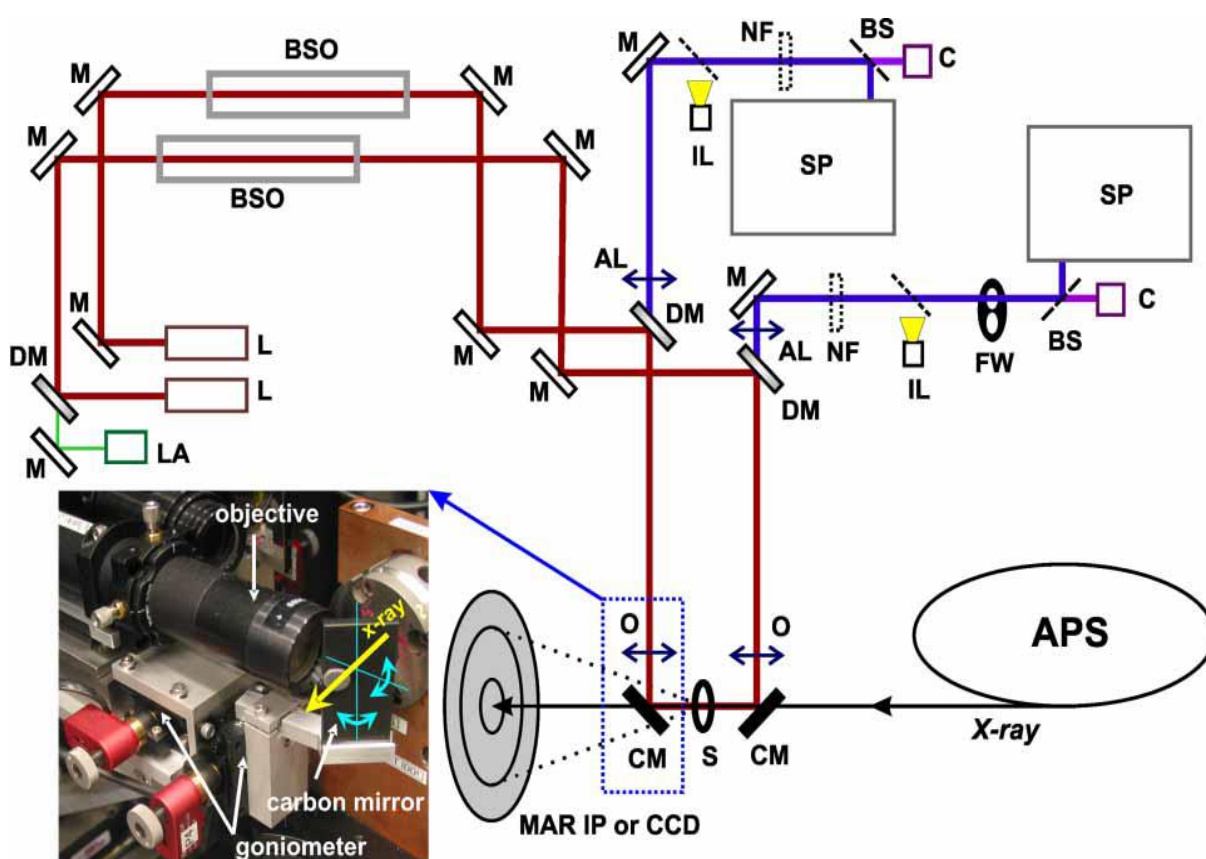


Figure 2.5: Experimental setup of laser heating diamond anvil cell in at GSECARS, 13-ID-D, Advanced Photon Source (APS) of Argonne National Laboratory (a) Picture (b) Schematic diagram (Prakapenka, 2008)

2.5. Powder X-ray Diffraction

By using a rich array of slits, collimators, focusing mirrors etc, the wide range of synchrotron radiation can be dispersed into X-ray, ultra-violet and infrared light and into different hutches for different types of studies. X-ray is high energy electromagnetic radiation, with wavelengths between roughly 0.1 \AA and 100 \AA (i.e., in between γ -rays and ultraviolet radiation). Therefore, crystal structures can diffract X-rays due to a similar length scale. X-ray powder diffraction is an

important non-destructive method for determining a range of physical and chemical properties of materials, such as phase identification, cell parameters and crystal structure changes, crystallographic textures, crystalline sizes, macro-stress and micro-strain. When compared to a conventional laboratory X-ray source (e.g., X-ray tube), synchrotron X-rays are 10^{13} times more brilliant. This high energy radiation is capable of penetrating the pressure container to probe high pressure samples. The interaction between X-rays and electrons of atoms in the samples results in a constructive spectrum when the path difference between two diffracted rays equals an integral multiple of the wavelength of incident X-ray. This selective condition is described by the Bragg equation (Bragg & Braag, 1913):

$$n \lambda = 2d \sin \theta \quad (\text{Eq: 2.2})$$

where n is the order of diffraction, λ is the wavelength of (elastically) scattered radiation, d is the spacing of lattice planes in a sample and θ is the angle of reflection with respect to these planes. The diffraction angle, defined as the angle between the incident primary beam and the diffracted beam, is therefore equal to 2θ . Diffraction experiments record scattered X-ray intensity as a function of either 2θ at a fixed wavelength (ADXRD) when monochromatic beam is used or as a function of energy at a fixed 2θ when a white beam source is used (EDXD). In this study, only ADXD were employed.

Angular dispersive X-ray diffraction (ADXRD) is a very popular non-destructive materials characterization technique that has been used in various fields ranging from engineering to biology. Buras and colleagues (Buras et al., 1977) were the first to use ADXRD techniques with DAC interfaced to synchrotron radiation. Since then synchrotron X-ray diffraction has become a well-established technique and has long been successfully applied in high pressure and high temperature studies in diamond anvil cell (Hu et al., 1993), with numerous synchrotron facilities worldwide providing access to scientists conducting experiments.

In ADXRD (Figure. 2.6), the wavelength of the incident X-ray beam is kept constant by using a monochromator and instead the angle at which the incident photons strike the lattice planes is changed. A single-crystal monochromator is used to select a very small segment of energy for

high resolution ADXRD. Diffraction by a powdered sample produces a number of diffraction rings at various 2θ angles which are collected by an area detector such as an imaging plate or a charge-coupled device (CCD) leads to a series of interference maxima in the shape of rings, concentric with the incident beam at values of 2θ that satisfy the Bragg law. By using the Bragg equation, $n\lambda=2d\sin\theta$, d-spacings are calculated from the observed θ angles. To reduce the possibility of single crystals like diffraction patterns (spotted), samples should be finely ground. Position of the atoms with the unit cell parameters can be calculated from the relative intensities of the diffraction peaks. With the synchrotron x-ray diffraction combining with laser heating systems it is possible to analyze samples at simultaneously high P-T condition in situ. We have performed the powder ADXRD experiment, double-sided laser-heated assemblage at GSECARS (13 ID-D) of APS.

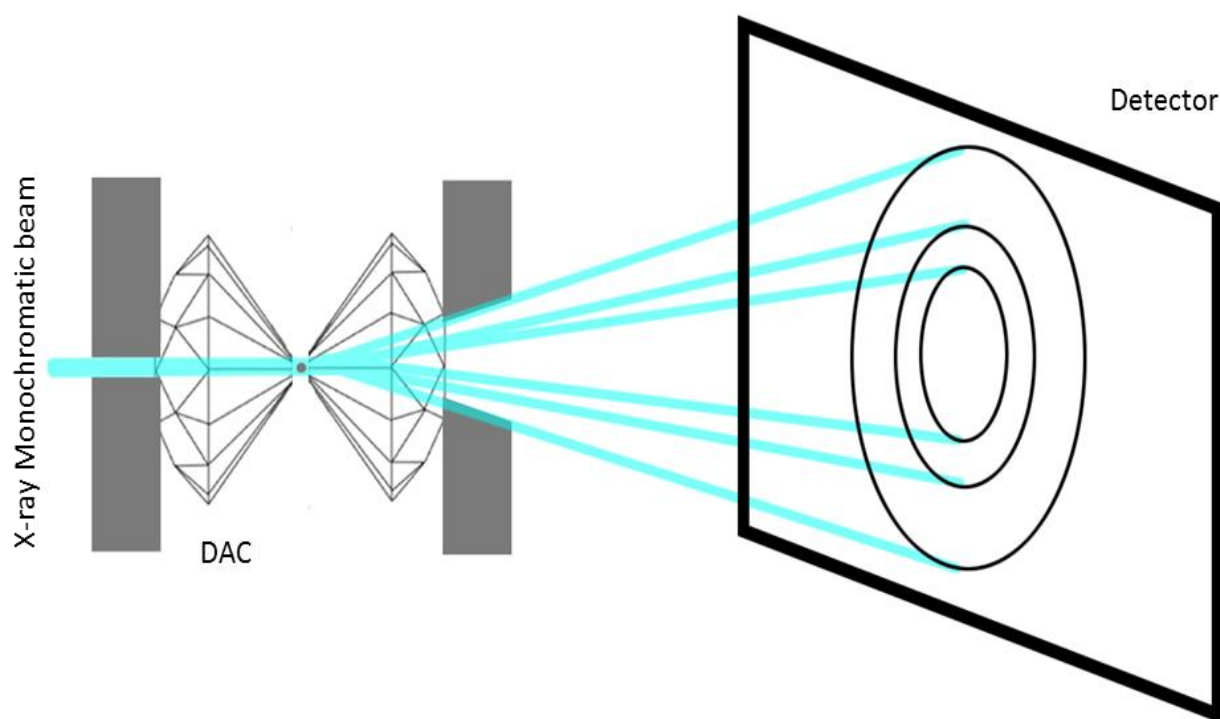


Figure 2.6: Schematic diagram of angular dispersive X-Ray diffraction technique

High pressure phase identification using synchrotron ADXRD techniques involves many advanced experimental methods, so error evaluation becomes an important issue (Ma et al., 2004). One possible source of error arises when using Bragg's law, which requires careful determination of diffraction angle 2θ to obtain accurate results. Another possible source of error

in a high pressure ADXRD experiment is the substantial heating of DAC which can cause a slight shift in lattice parameter. This occurs due to absorption of much of the X-rays with energy less than 10 keV by diamond anvils and sample (Baublitz et al., 1981).

2.6. Raman Spectroscopy

When photons of a single wavelength (monochromatic light, in this case a laser) interact with matters, the in-elastically scattering phenomenon is called Raman Effect.

With Raman scattering, the incident photons interact with materials and their energy level is either shifted up or down. The photon interacts with the electron cloud of the functional group bonds, and excites them to a virtual state. Electron then relaxes into an excited vibrational or rotational state, causing the photon to lose parts of its energy and been detected as Stokes Raman scattering. The loss of energy depends on the molecular structure, the functional group, the types of atoms in that molecule and its environment. Therefore, Raman spectroscopy can provide a finger print analysis of vibration or rotation in materials. With a transparent diamond window, materials under extreme pressure in a DAC could be studied by Raman spectroscopy.

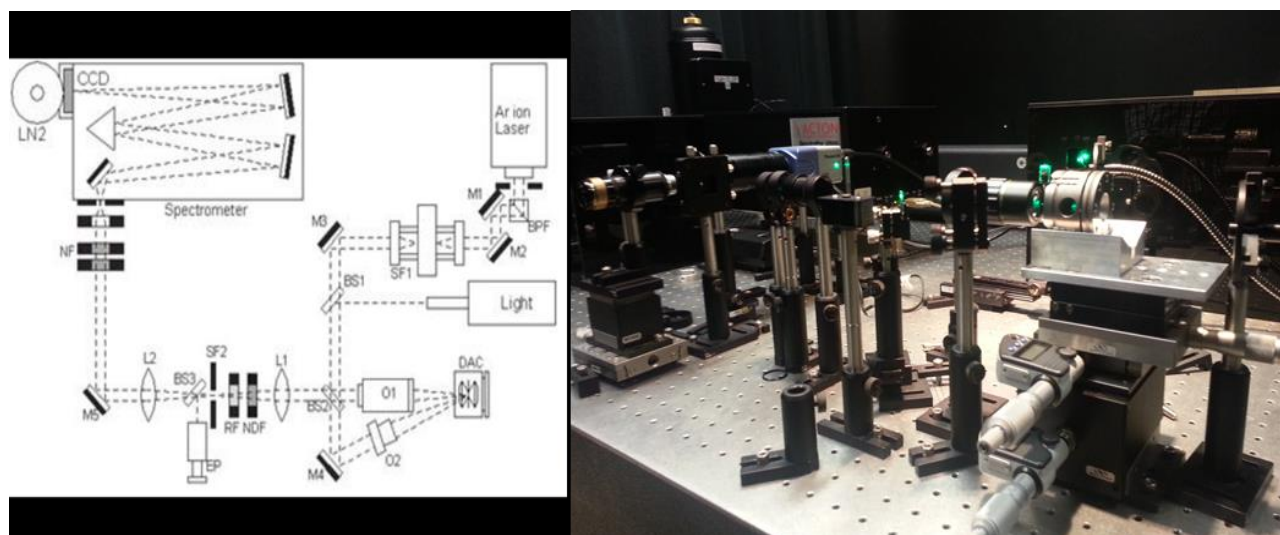


Figure 2.7: Layout of the Raman system used in this study for high pressure ruby fluorescence measurements.

In this study, a user-customized Raman system combined with ruby fluorescence method was used to determine ruby pressures in a DAC. The schematic diagram of the Raman system is shown in Figure 2.7. A beam of monochromatic light with a wavelength of 514.532 nm is directed into the sample. Most of the light passes straight through, but some is scattered by the sample. The scattering signals from the sample spot are collected by a set of optics and passed through a spectrometer for analysis. Wavelengths close to the laser line, due to elastic Rayleigh scattering, are filtered out while the rest of the collected signals are dispersed onto a liquid-nitrogen cooled charge-coupled device detector. The instrument control and data collection are performed by the software WinSpec. Pressure determination can be obtained directly from shifts in ruby fluorescence peak.

2.7. Ruby Fluorescence Scale

The use of wavelength shift of ruby R1 fluorescence line to determine pressure was originally developed by Forman, Piermarini, Barnett and Block (Forman et al., 1972). The original calibration of this method involved observing the shift of ruby R1 line with pressure, while simultaneously measuring specific volumes of several metals (Cu, Mo, Pd and Ag) by X-ray diffraction. The absolute pressure was obtained indirectly by making reference to the isothermal equations of state of metals derived from shock-wave data (Mao et al., 1986). After being revised numerous times, the ruby fluorescence method is now widely used as a common pressure scale for high pressures above 10 kbar (1 GPa).

When used in a DAC, the ruby chip is placed inside the sample chamber along with pressure medium and sample, and the fluorescence is excited using a laser or any strong light source. An optical detector collects the signal which is then displayed as a graph showing intensity versus wavelength. The R lines for ruby are quite intense and shift linearly to higher wavelengths under hydrostatic pressure (Jayaraman, 1983). Measurement of the wavelength is commonly achieved by determining the wavelength, λ_0 , of the maximum intensity R₁ line (Munro et al., 1985). This value is then used in conjunction with the equation

$$P = 1904/B \{ [1 + (\lambda - \lambda_0) / \lambda_0]^B - 1 \} \quad (\text{Eq: 2.3})$$

to determine pressure inside the sample chamber, where B is the curvature parameter (7.665 for hydrostatic, 5 for quasi-hydrostatic), λ is the measured wavelength, and λ_0 is the wavelength of maximum intensity R_1 line at ambient pressure (694.24 nm). Although the ruby fluorescence scale is accurate under hydrostatic conditions, when hydrostaticity diminishes it introduces significant error. When ruby is subjected to non-hydrostatic stress, the R lines become broader. Pure uniaxial stress produces an even greater broadening effect than non-hydrostaticity. This increasing line-width phenomenon makes ruby a useful sensor for detecting the limits of hydrostaticity under pressure (Munro et al., 1985).

2.8. Sample Preparation

2.8.1. Sample

In this study, starting material is magnesiochromite (MgCr_2O_4). Dr. Tony Wither, assistant professor of the department of earth sciences in UWO synthesized the magnesiochromite sample. A stoichiometric mixture of reagent grade MgO and Cr_2O_3 was used to synthesize the magnesiochromite. The chemical mixture was first pulverized with ethanol in an agate mortar and then hard-pressed into a pellet. Synthesized of Magnesiochromite was done by heating the pellet in a flowing atmosphere of pure CO_2 at 1300°C for 24 h. Sample was inspected by powder X-ray diffraction after quenching in air to ambient conditions in order to confirm the synthesis of magnesiochromite. The achieved lattice parameters for magnesiochromite are $a = 8.3332 \text{ \AA}$ and $V = 578.68 \text{ \AA}^3$, consistent with formerly reported parameters (Lenaz et al., 2004).

2.8.2. DAC

Sample preparation and good sample configuration in DAC are essential to a successful experiment. A symmetrical DAC with $300 \mu\text{m}$ flat culet diamonds for higher pressure (>20 GPa), and $500 \mu\text{m}$ flat culet diamonds for lower pressure (<20 GPa) was used in the experiment. Before using DAC in this experiment, the culets were aligned with the rotational center of cell to eliminate any stress concentrations which could cause the diamonds to crack under high pressure. This was achieved by first tightening the set screws to a point where the diamonds

could not come in direct contact with each other. Next, the diamonds were aligned using the lateral translation screws. The cylinder was then held stationary and the piston was rotated by 180° . After rotation, the diamond mounted in piston was checked for alignment with the cylinder diamond and if found misaligned, was translated halfway to line up with the center of the stationary cylinder diamond via lateral translation screws. The cell was then flipped over and the cylinder diamond was aligned with diamond in the piston. The piston was held stationary while the cylinder was rotated 180° and if found misaligned, the cylinder diamond was translated halfway to the center of the diamond in the piston (similar to the previous step). The process of aligning the diamonds is iterative in nature, and the above procedure is usually repeated 3-4 times before the diamonds are perfectly aligned with the rotational center of the cell.

After the alignment was complete, small pieces of sandpaper were used to remove any debris and then a q-tip soaked in methanol was used to thoroughly clean the culets. This was repeated several times to ensure that the culets were clean and ready for further procedures. Figure 2.8 shows an unaligned and an aligned DAC.

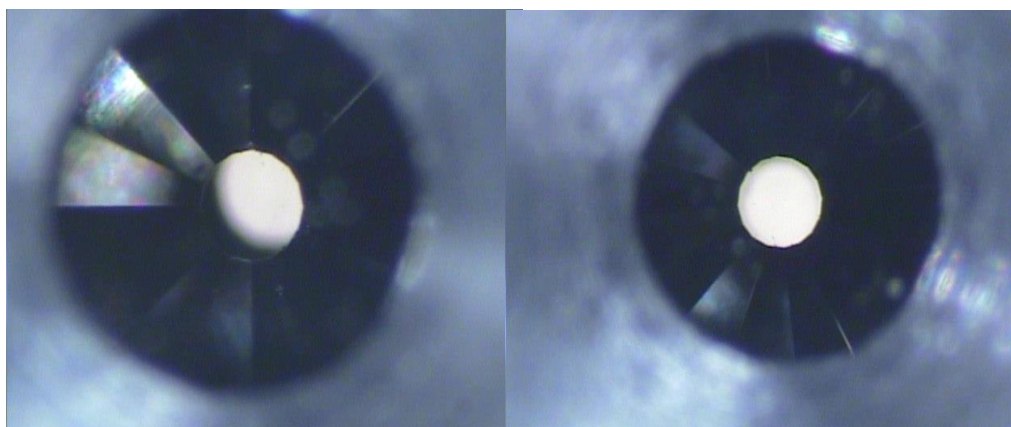


Figure 2.8: Unaligned and aligned DAC

2.8.3. Gasket Preparation

The introduction of a gasket into the diamond anvil apparatus, which was first demonstrated by Van Valkenburg (1965), was a very important development in the history of DAC; this invention that allows the use of DAC as a quantitative tool in high pressure research. The gasket performs

two functions in a high pressure experiment. With a hole drilled through it provides a chamber for the sample being studied and also provides lateral support to the diamond anvils. This support is given by the gasket extruding from the sample chamber around the side of diamond anvils. This extrusion, acting as a supporting ring, creates stress concentrations towards the sample at the edge of culets thereby preventing any motion of gasket material between anvils and thus prevents failure of anvil (Jayaraman, 1983). Below ~ 5 GPa, the gasket does not display significant deformation and beyond ~ 5 GPa, the gasket material yields and undergoes large deformation and flows out of the sample chamber to form a curved feature. The flow rate decreases after ~ 50 GPa due to bending of the diamond anvils. This process is illustrated in Figure 2.9.

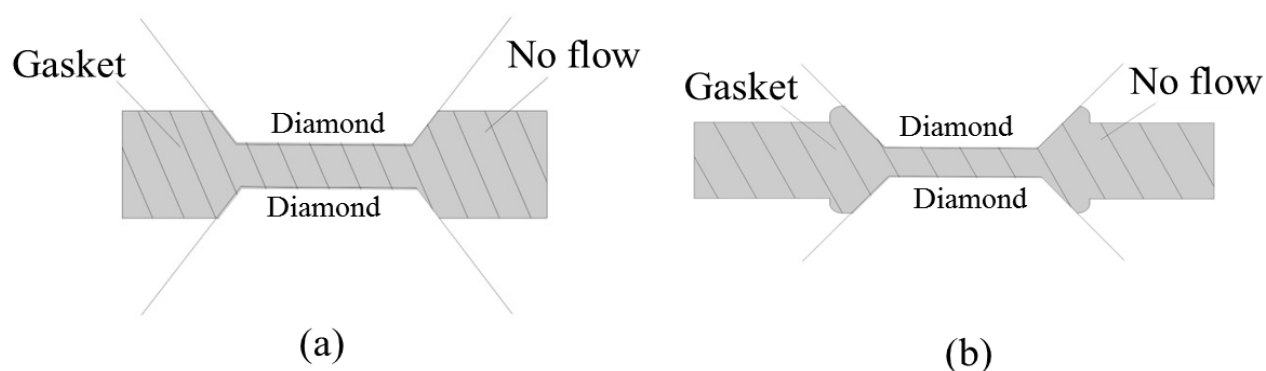


Figure 2.9: Deformation of gasket under pressures during indentation; (a) Before deformation at low pressure; (b) After deformation at high pressure

The first step in preparing the gasket was to create an indentation at its center by subjecting the gasket to a pressure predetermined by the designated maximum pressure in the experiment. This was done by using the DAC in conjunction with a small ruby chip to measure the indentation pressure. After the gasket was indented, it was removed from DAC and a hole was drilled in the center of the indentation with an electrical drilling machine (EDM).

An EDM uses electricity as opposed to mechanical methods to machine metals. In this process, a spark is created between a tool (tungsten bit) and a sample (gasket) of different voltage polarity when they are brought into close proximity. This spark occurs when a tool discharges current to the sample through a dielectric medium, can melt a small portion of the sample provided that the spark contains sufficient energy (Lorenzana, 1994). The process can be applied to both soft and

hard metals makes the EDM is appropriate for drilling high pressure gasket materials such as rhenium, stainless steel and inconel with 2-3 μm tolerances (Lorenzana, 1994). The picture of an EDM is shown in Figure 2.10.



Figure 2.10: Electronic drilling machine (EDM).

In preparation for drilling a hole with the EDM, the indented gasket was placed on the stage and secured with a small metal mount (positive side of the electric circuit). Then the wire drilling tool (negative side of the electric circuit) was lowered (z-direction) until it almost touched the gasket, and the stage was translated (x and y-directions) until the tool was aligned with the center

of the indentation. Off-center alignment could have caused the sample to migrate under load from the center to the edge of the culet. This phenomenon would limit the highest pressures of the experiment and perhaps caused premature failure of the anvils (Lorenzana, 1994). After centering, a dielectric organic solvent (EDM 185™ by Commonwealth Oil's) was dropped onto the stage and the tool was brought close enough to the gasket to initiate the spark. Figure 2.13 shows the gasket at different stages in the process.

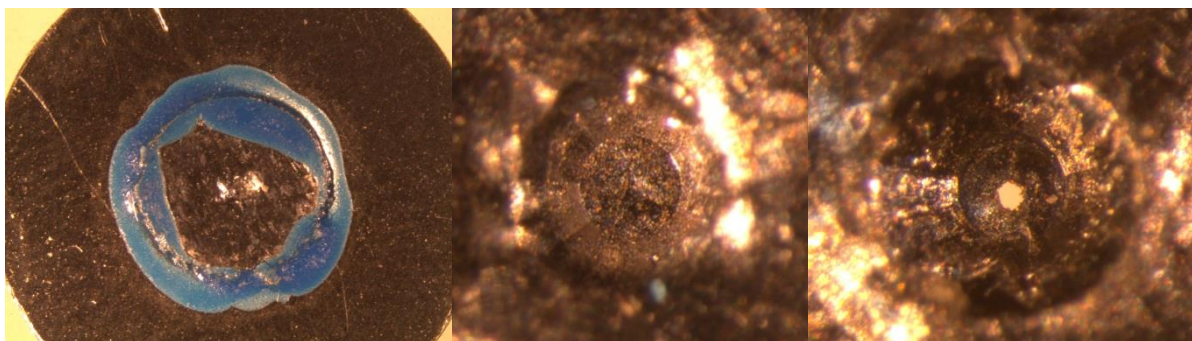


Figure 2.11: Gasket; (a) Rhenium gasket attached in the middle of steel gasket; (b) after indentation with DAC; (c) After drilling hole

2.8.4. Sample Loading

Chromite sample was ground into fine grains and compressed to form a large flake before placing into the sample chamber. This was done using 1 in³ tungsten carbide blocks. With a pre-drilled gasket centered on the bottom culet (piston side), the sample flake was placed at the center of gasket hole avoiding contact with the gasket. Similarly, gold flake has been prepared with tungsten carbide block, and placed on the opposite diamond in such a way that it touched the corner of the sample which works as a pressure standard. A small ruby chip was then placed on the culet between the sample and the gasket in order to measure the pressure during Ne gas loading. After placement of the sample and ruby, the cylinder side of the DAC was carefully lowered onto the piston, avoiding any impact of top culet with sample and ruby.

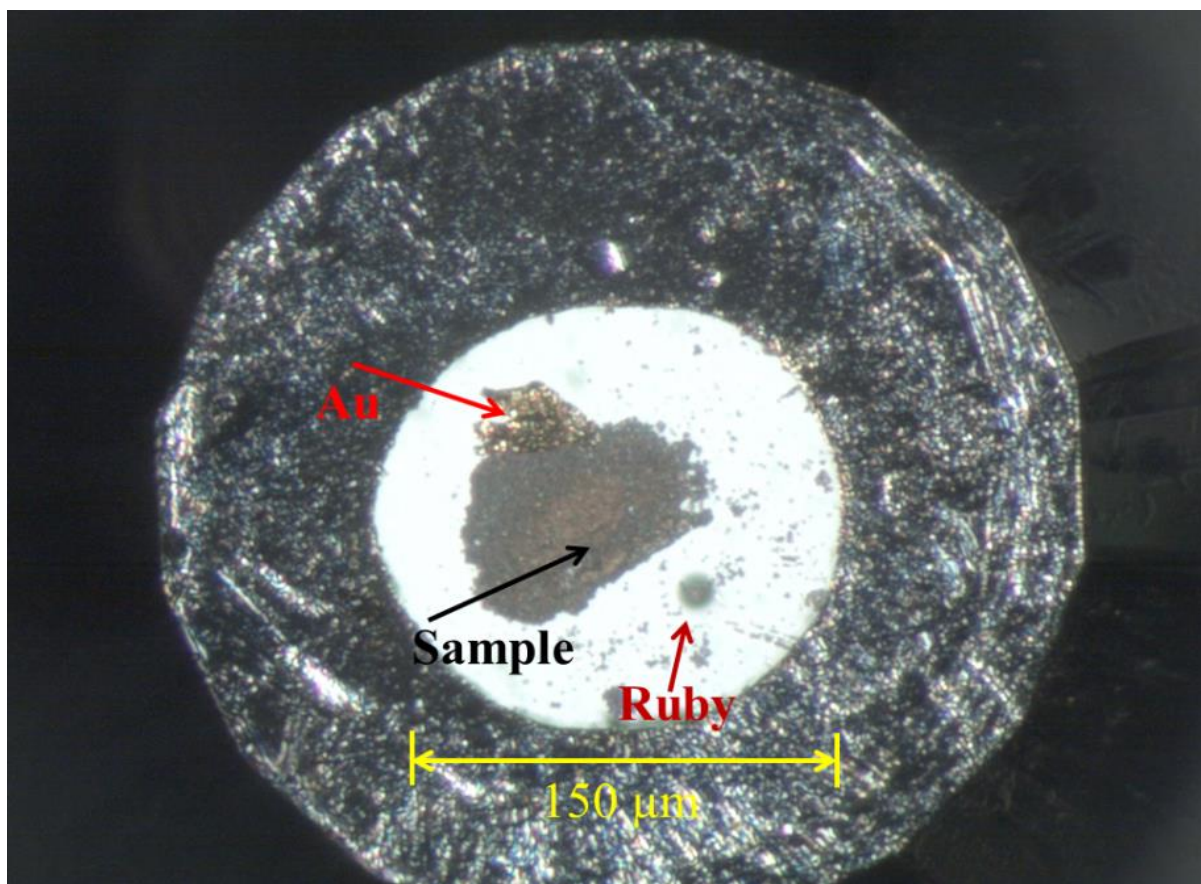


Figure 2.12: Example of sample configuration for the X-ray diffraction study in a DAC.

2.8.5. Pressure medium

The next step in the experimental procedure is to load the pressure transmitting medium into the sample chamber. The pressure medium completely fills the spatial voids in the sample chamber that are left after loading the sample and pressure calibrator. The function of pressure medium is to convert the axial forces applied by squeezing mechanism of DAC into hydrostatic pressure on the sample. It is desirable to have a low shear strength (minimizing deviatoric stresses in the sample chamber) and chemical inertness (non-reactive with the sample). The ideal pressure media are noble gases, which fulfill all these requirements (Boehler, 2000).

In this experiment we used liquefied Neon, which helps achieve hydrostatic conditions up to 60 GPa. The pressures reached throughout the experiment were well within the hydrostatic limits of the pressure medium. When loading the pressure medium, the first step was to loosen the set

screws and slightly tighten the main screws, allowing the culets to come in contact with the gasket but not sample. At this point reference guidelines were marked on each screw, with four matching lines being marked on the DAC. These later allowed the pressure medium inside the sample chamber to be secured without applying any initial pressure. Next, the main screws were loosened, turned by 180° and one set screw tightened until a slight gap was observed between the culets and the gasket. If this gap was too large, the sample may be lost when the pressure medium filled the sample chamber. The set screw was then loosened to allow the pressure medium to be contained inside the sample chamber when the main screws were tightened later on in the procedure. The DAC was then gently placed in a container capable of withstanding cryogenic conditions, while avoiding any impulse forces on the sample. This container was placed inside an insulating shell and a helical copper tube which was connected to an argon tank at one end and entered the container at the other end was inserted between them. The tank valve was opened and neon was allowed to flow into the container for several minutes. Next, a cover was placed over the container to separate the DAC from dry air which could have condensed upon cryogenic cooling and entered the sample chamber. Liquid nitrogen was poured between the two containers submerging the copper tube. At this point the neon began to liquefy due to conductive heat transfer with liquid nitrogen and was allowed to flow until the entire sample chamber was submerged. After submersion was complete, the liquefied neon continued to flow until boiling (caused by the room temperature DAC) stopped. Then the main screws were tightened 180° to their original position, containing the pressure medium inside the sample chamber. Finally, the DAC was removed from container and allowed to reach room temperature.

2.8.6. Determination of Equations of state (EOS)

Equations of state (EOS) of deep planetary materials are essential in understanding observed seismic structure of the Earth in terms of its mineralogy, and geodynamics of the planet's interior. By analyzing the seismic travel times, it is possible to derive the average densities, elastic moduli at the various depths, and pressures of the Earth's interior. In order to build consistent mineralogical models of the Earth interior, those parameters can then be used together with the elastic moduli of mineral assemblages determined from EOS.

The EOS relates the pressure (P), temperature (T) and specific volume (V), which are not all independent and have to be specified in order to define the thermodynamic state of a system. The simplest EOS is the one that describes an ideal gas:

$$PV = nRT \quad (\text{Eq: 2.4})$$

Where R = gas constant and n = number of moles

The effect of temperature (T) is much less for solids than for gases. The simplest isothermal EOS for solids is given by the definition of the bulk modulus K:

$$K = - \left(\frac{d \ln V}{dP} \right)^{-1} = - \frac{dP}{d \ln V} = - \left(\frac{d \ln M}{dP} \right)^{-1} - \left(\frac{d \ln \rho}{dP} \right)^{-1} = \frac{dP}{d \ln \rho} = -V \left(\frac{dP}{dV} \right)_T \quad (\text{Eq: 2.5})$$

If infinitesimal strains result from the application of hydrostatic pressure on the solid, bulk modulus can be considered as constant. When integrating with $K = K_0$, which means the tangent of the P vs. V curve through the zero point, the EOS becomes:

$$V = V_0 \cdot e^{-\left(\frac{P}{K_0}\right)} \quad (\text{Eq: 2.6})$$

This simple EOS does not consider the increase of the bulk modulus with pressure which limit the validity of this EOS only for low pressures.

2.8.7. Murnaghan integrated linear EOS

Murnaghan proposed an EOS in 1944 that considers the linear dependence of the bulk modulus with pressure. The change of K with P is defined by

$$K' = \left(\frac{dK}{dP} \right)_T \quad (\text{Eq: 2.7})$$

K' is the pressure derivative of the bulk modulus and describes the curvature of the P vs. V curve. K' is usually in between 2 and 8 and set to 4, if it cannot be determined with confidence.

A simple formalism is derived when expanding K to first order in P:

$$K \approx K_0 + K'P \quad (\text{Eq: 2.8})$$

Inserting the K into previous equation and with integration, the Murnaghan integrated linear EOS is obtained:

$$\frac{V}{V_0} = \left(1 + \frac{K'P}{K_0}\right)^{-\frac{1}{K'}} \quad (\text{Eq: 2.9})$$

2.8.8. Birch-Murnaghan EOS

Birch-Murnaghan EOS (Birch 1947) is the most commonly used EOS by mineralogists, which has been published in 1947. The displacement of a solid under hydrostatic conditions is not uniform; hence the solid undergoes a strain.

If the properties of solids are considered elastic:

$$\frac{V}{V_0} = (1 - 2\varepsilon)^{\frac{3}{2}} \quad (\text{Eq: 2.10})$$

As ε is dilatation which is negative for positive pressures, the compression “f” is introduced:

$$f = -\varepsilon \quad (\text{Eq: 2.11})$$

$$f = \frac{1}{2} \left[\left(\frac{V}{V_0} \right)^{\frac{-2}{3}} - 1 \right] \quad (\text{Eq: 2.12})$$

The Helmholtz free energy (F) is expanded in powers of f:

$$F = af^2 + bf^3 + \dots \quad (\text{Eq: 2.13})$$

$$P = - \left(\frac{dF}{dV} \right) \quad (\text{Eq: 2.14})$$

An expansion of F to second order provides the second-order Birch-Murnaghan EOS, to third order in the third-order Birch-Murnaghan EOS. Finite strain theory gives a numerical value of $K' = 4$ for the infinitesimal case $f \rightarrow 0$. Normally, close-packed minerals show experimental values of K' close to 4.

2.8.9. The third-order Birch-Murnaghan EOS

$$P = 3K_0 f (1 + 2f)^{\frac{5}{2}} \left[1 + \frac{3}{2}(K' - 4)f \right] \quad (\text{Eq: 2.15})$$

$$P = \frac{3}{2} K_0 \left[\left(\frac{V_0}{V} \right)^{\frac{7}{3}} - \left(\frac{V_0}{V} \right)^{\frac{5}{3}} \right] \left\{ 1 - \frac{3}{4} [4 - K'] \cdot \left[\left(\frac{V_0}{V} \right)^{\frac{2}{3}} - 1 \right] \right\} \quad (\text{Eq: 2.16})$$

If $K' = 4$, the second-order BM EOS is obtained.

2.9. Analysis of X-Ray Diffraction Patterns

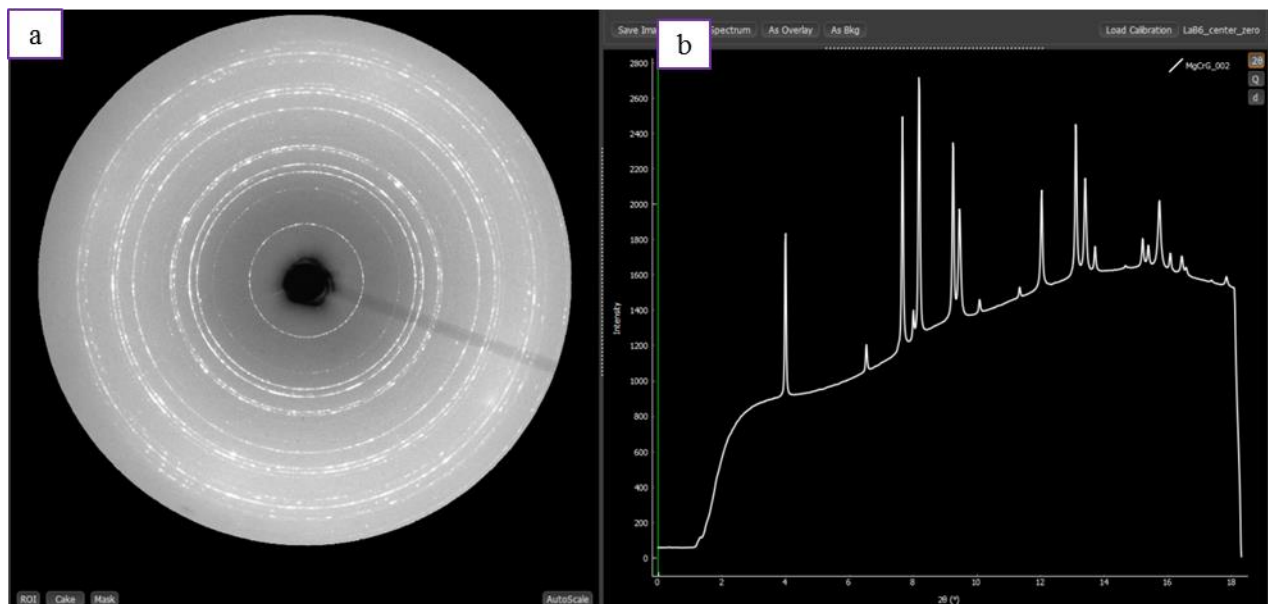


Figure 2.13: (a) 2-dimensional XRD pattern collected by CCD, (b) after integration (c) peak position determination using PeakFit program

The 2-dimensional CCD detector collects the pattern of rings of diffracted X-rays of various diameters of the crystals (Figure 2.13). These patterns are then integrated azimuthally using Fit2D software (Hammersley et al., 1996) to better illustrate the relationship between the

diffraction rings and their angle to the main X-ray beam. Each ring appears as a peak on a 1-dimensional plot; the relationship between the peak's angle to the main X-ray beam and the crystal structure of the sample is given by the Bragg Diffraction Equation:

$$n\lambda = 2 \cdot d \cdot \sin(\theta) \quad (\text{Eq: 2.17})$$

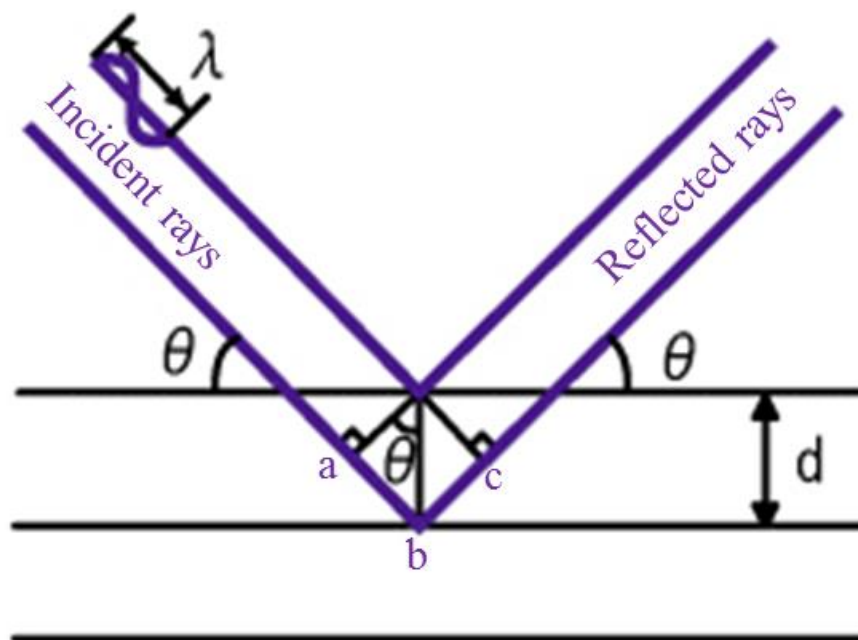


Figure 2.14: Bragg's Law reflection. The diffracted X-rays exhibit constructive interference when the distance “abc” is an integer number of wavelengths (λ).

In this equation, λ is the wavelength of the photons, θ is the angle of X-ray diffraction relative to the incident X-ray beam, and d is a measure of the distance between planes in an idealized crystal lattice. Peaks position (θ) is obtained using the PeakFit (Version 4.12), which has been used to calculate the d -spacing using Bragg law. The parameters of the unit cell and the volume have been calculated by least-squares fit using the UnitCell program (Holland and Redfern, 1997). The pressure was determined from the measured d -spacings of Au using the equations of state of Au (Fei et al., 2007).

Chapter 3

3. Phase diagram of MgCr_2O_4

High pressure and high temperature experiments of synthetic magnesiochromite (MgCr_2O_4) were performed at GSECARS, 13-ID-D, Advanced Photon Source (APS) of Argonne National Laboratory (ANL). From the X-ray diffraction measurements, we collected the diffraction patterns up to 40 GPa and 2000 K in several heating cycles using double-sided laser heating diamond anvil cell. The goal of the experiments was to synthesize the high pressure and high temperature polymorphs of MgCr_2O_4 and construct the phase diagram.

3.1. Experiment

High pressure and high temperature experiments were performed using double-sided laser heating diamond anvil cells technique at GSECARS laser heating facility (Prakapenka et al., 2008). Synthesized MgCr_2O_4 first ground to fine powder and mixed with ~10 wt.% gold for use as a pressure calibrant. Mixtures of the sample and gold were then loaded into the ~150 μm hole of a rhenium gasket. Neon gas was also loaded in DAC as a pressure medium with the GSECARS high-pressure gas loading system. The temperature of the laser heated spot was measured from both sides using the light emitted from the heated spot by spectroradiometry. The samples were probed with a monochromatic X-ray beam $3\times 3 \mu\text{m}^2$ in cross-section and 0.3344 Å in wavelength, whereas the cross-section of laser heating spot was $20\times 20 \mu\text{m}^2$. The X-ray beam was ensured to be in the center of the heating spot by carefully aligned the optical paths using fluorescence generated by the X-rays as they passed through the sample. The 2-dimensional CCD detector used to collect the pattern of rings of diffracted X-rays of various diameters of the crystals. The sample-to-detector distance and orientation of the detector was calibrated using CeO_2 powder.

3.2. Results

XRD data from a representative heating cycle are shown in Figure 3.1. At ambient pressure and temperature, it shows only magnesiochromite structure with peak positions at (111), (220), (311), (222), (400), (331), (422), (333), (440), (531), (533), (622), (444) and (711). When the pressure increased to 23.5 GPa at ambient temperature, the tetragonal phase of chromite appeared. At this high pressure, the sample has been heated until it transforms to a new phase (For miller indices: Appendix A3). Due to the local heating phenomenon of the laser heating technique, the pressure increased a few GPa during heating. The new phase has been confirmed as CaTi_2O_4 type structure of MgCr_2O_4 .

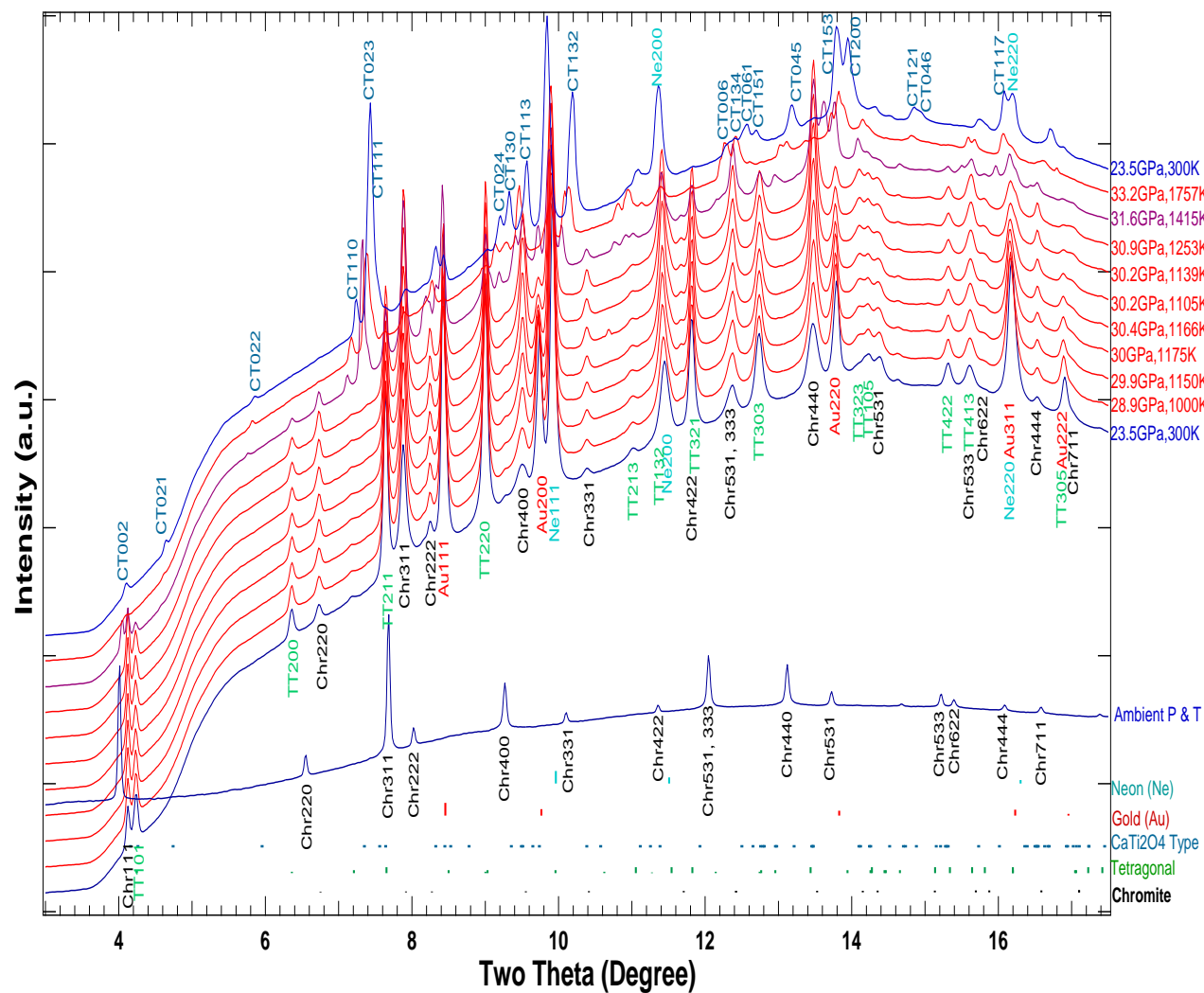


Figure 3.1: Synthesis of CaTi_2O_4 type structure of MgCr_2O_4

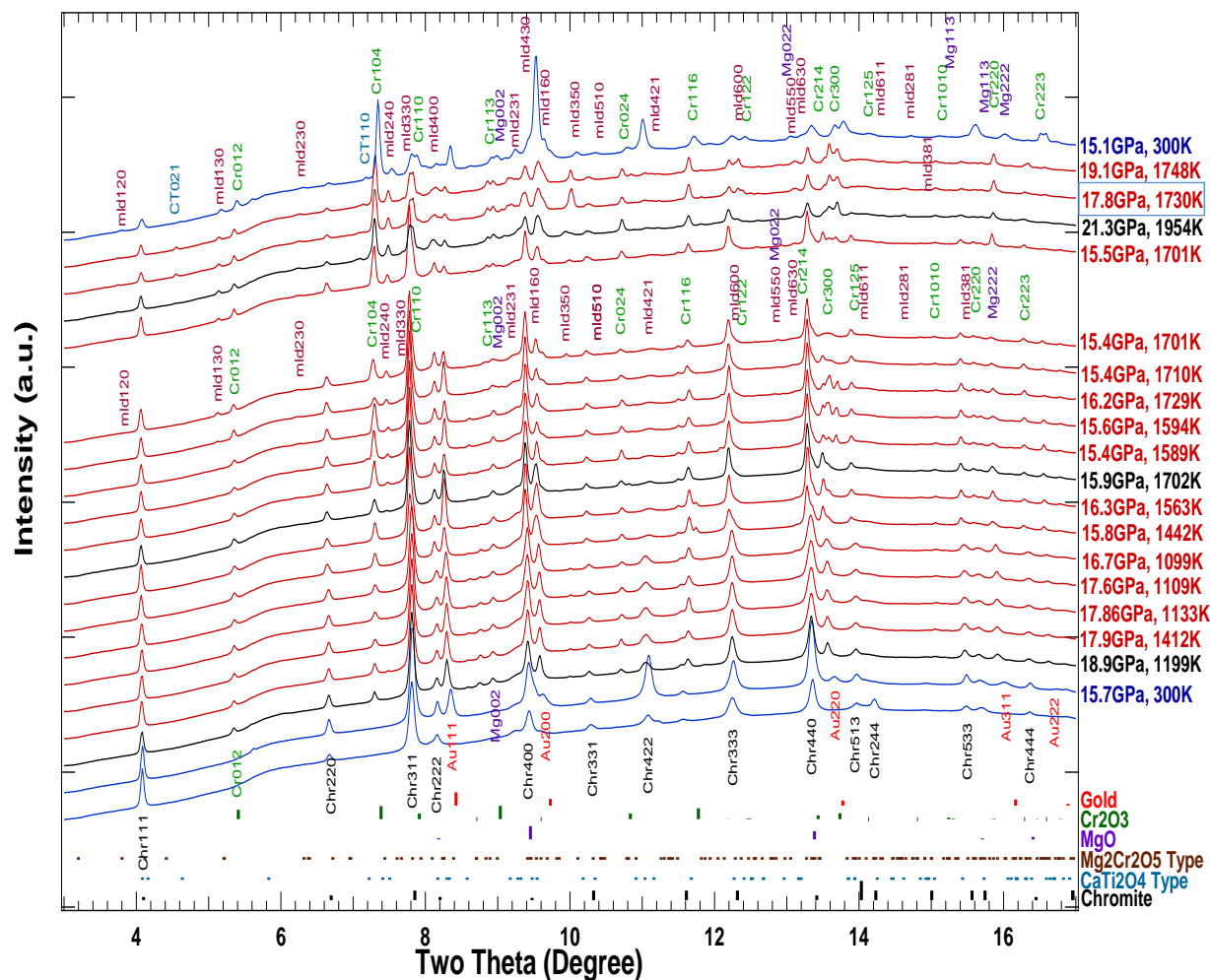


Figure 3.2: MgCr_2O_4 first dissociates to $\text{Cr}_2\text{O}_3+\text{MgO}$ about at 1200 K and 16 GPa, and then to $\text{Mg}_2\text{Cr}_2\text{O}_5+\text{Cr}_2\text{O}_3$ about at 1700 K and 16 GPa.

In our first heating cycle (Figure 3.1), we obtained a CaTi_2O_4 type structure (CT) due to high initial pressure. We observed the dissociation of MgCr_2O_4 to Cr_2O_3 and MgO (Figure 3.2 & Table 3.1) when the sample was heated at ~ 1200 K at pressure ~ 15 GPa. When the temperature was increased to ~ 1600 K, Cr_2O_3 and MgO joined together in 1:2 ratios to form $\text{Mg}_2\text{Cr}_2\text{O}_5$. At this stage the phases are $\text{Mg}_2\text{Cr}_2\text{O}_5$ and Cr_2O_3 (Figure 3.2 & Table 3.1).

Table 3.1: Results of high-pressure high-temperature experiments (CT = CaTi₂O₄ type structure, mLd = MgCr₂O₅).

Run No.	Pressure (GPa)	Temperature (K)	Phases
MgCrE_024	30.6 (4)	1738 (115)	CT
MgCrE_126	31.2 (5)	1772 (86)	CT
MgCrE_127	30.8 (4)	1825 (103)	CT
MgCrE_128	31.2 (4)	1842 (122)	CT
MgCrE_129	30.9 (3)	1786 (86)	CT
MgCrE_130	30.9 (2)	1793 (200)	CT
MgCrE_131	31.1 (2)	1796 (200)	CT
MgCrE_157	29.4 (3)	1415 (145)	CT
MgCrE_158	32.2 (2)	1757 (200)	CT
MgCrE_177	33.6 (3)	1724 (200)	CT
MgCrE_178	34.1 (3)	1792 (168)	CT
MgCrE_179	32.8 (2)	1749 (200)	CT
MgCrG11	19.2 (2)	1079 (190)	Cr ₂ O ₃ +MgO
MgCrG12	22.7 (3)	1750 (200)	CT
MgCrG14	18 (2)	1540 (1)	mLd+ Cr ₂ O ₃
MgCrG15	18 (3)	1540 (123)	mLd+ Cr ₂ O ₃
MgCrG16	18.5 (2)	1674 (15)	mLd+ Cr ₂ O ₃
MgCrG17	18.8 (2)	1679 (72)	mLd+ Cr ₂ O ₃
MgCrG27	18.9 (3)	1199 (200)	Cr ₂ O ₃ +MgO
MgCrG28	18 (2)	1412 (195)	Cr ₂ O ₃ +MgO
MgCrG29	17.9 (3)	1133 (200)	Cr ₂ O ₃ +MgO
MgCrG30	17.6 (3)	1109 (192)	Cr ₂ O ₃ +MgO
MgCrG31	16.7 (2)	1099 (200)	Cr ₂ O ₃ +MgO
MgCrG32	15.8 (2)	1442 (91)	Cr ₂ O ₃ +MgO
MgCrG34	15.9 (2)	1702 (135)	mLd+Cr ₂ O ₃
MgCrG35	15.4 (3)	1589 (1)	mLd+Cr ₂ O ₃
MgCrG36	15.6 (2)	1594 (18)	mLd+Cr ₂ O ₃
MgCrG38	16.1 (3)	1729 (200)	mLd+Cr ₂ O ₃

MgCrG39	15.4 (2)	1710 (115)	mLd+Cr ₂ O ₃
MgCrG40	15.5 (2)	1701 (36)	mLd+Cr ₂ O ₃
MgCrG41	21.3 (2)	1954 (200)	CT
MgCrG42	17.8 (3)	1730 (97)	CT
MgCrG43	19.1 (2)	1748 (133)	CT
MgCrG57	20.9 (2)	1727 (24)	CT
MgCrG58	20.3 (3)	1692 (37)	CT
MgCrG59	21.1 (2)	1616 (45)	CT
MgCrG60	19.2 (3)	1556 (33)	CT
MgCrG61	24.8 (2)	1835 (108)	CT
MgCrG62	24.6 (3)	1862 (37)	CT
MgCrG63	24.4 (2)	1771 (4)	CT
MgCrH17	13.1 (3)	1630 (200)	Spinel
MgCrH18	13.2 (2)	1637 (200)	Spinel
MgCrH22	13.3 (2)	1225 (120)	Spinel
MgCrH23	13.5 (3)	1547 (109)	Spinel
MgCrH24	17.9 (2)	1494 (25)	mLd+Cr ₂ O ₃
MgCrH25	17.9 (2)	1385 (54)	mLd+Cr ₂ O ₃
MgCrH27	18.6 (3)	1682 (9)	mLd+Cr ₂ O ₃

The result has been summarized in table 3.1, which has been used to draw the phase diagram (Figure.3.3) between different high pressure high temperature polymorphs of magnesiochromite. In our first set of experiments the pressure was too high (>30 GPa). After heating the sample at ~1700 K all new phases become pure CaTi₂O₄ type structure (CT) of single phase MgCr₂O₄. All following x-ray diffraction experiments have been performed at lower pressures (10 to 20 GPa) and temperatures (1000 to 2000 K). We found the MgO+Cr₂O₃ phases at 16.7 GPa and 1100 K at the run number MgCrG31, and Mg₂Cr₂O₅+Cr₂O₃ phases at 15.4 GPa and 1589 K at the run number MgCrG35. However, at pressure ~20 GPa, the heated sample showed CT at run number MgCrG12, MgCrG41, MgCrG42, MgCrG43, MgCrG57, MgCrG58 and MgCrG59. It is to mention that the magnesiochromite structure is present in the first two cases with MgO+Cr₂O₃ and Mg₂Cr₂O₅+Cr₂O₃, also CaTi₂O₄ type structure with Mg₂Cr₂O₅+Cr₂O₃ close to the boundary. We interpreted that the appearance of new phases at any temperature and pressure are the stable

condition for that new phase. The presence of old phases may be due to the duration of the heating was not long enough. Close to the boundary, the sample takes a longer time to transform completely to new phases due to the higher kinetic energy. When the sample experiences the pressure and temperature condition well above the stable condition, it transformed completely in new phases within few minutes. For example, the transformed phase is always pure CaTi_2O_4 type structure of MgCr_2O_4 (Figure.3.1), at higher pressure and temperature (>30 GPa, 1700 K).

In the heating cycle shown in Figure 3.2, the first appearance of the peaks of CT phase in run number MgCrG41 at the condition of pressure 21.3 GPa and temperature 1953K (table 3.1). But if we take a close look at this heating cycle, Temperature and pressure suddenly dropped in the next run MgCrG42 to 17.8GPa and 1730K. The formation of the new phase shown smaller volumes and therefore the pressure reduced. There was a sudden flash during the phase transformation in the monitor, which was showing the heating spot on the sample. From the safety concern of diamond anvil cell, the laser power was then lowered down to decrease the temperature. Nevertheless, the peaks of CT phase was still observable in the run number MgCrG42. This is probably due to the kinetic issue of the CT phase. The same phenomenon can be observed in run number MgCrH25 (Appendix 5). $\text{Mg}_2\text{Cr}_2\text{O}_5+\text{Cr}_2\text{O}_3$ have already been synthesized at higher pressure and temperature and then temperature dropped in the same heating cycle. So, we excluded those kind of data in which temperature dropped suddenly after synthesization of new phases. We plotted the different phases of MgCr_2O_4 obtained in different pressure and temperature in order to construct the phase diagram (Figure.3.3).

The unit-cell lattice parameters determined from peak positions of cubic MgCr_2O_4 , tetragonal MgCr_2O_4 , mLd-type $\text{Mg}_2\text{Cr}_2\text{O}_5$, CT-type MgCr_2O_4 , MgO and Cr_2O_3 are summarized in Table 3.2. Obtained unit-cell lattice parameters at ambient condition for mLd-type $\text{Mg}_2\text{Cr}_2\text{O}_5$ ($a_0=9.62894$ Å, $b_0=12.4625$ Å and $c_0=2.85644$ Å) and CT-type MgCr_2O_4 ($a_0=2.85107$ Å, $b_0=9.48930$ Å and $c_0=9.67853$ Å) is very similar to the cell parameter reported by Ishii et al. (2015) (Table 3.3). In table, numbers in the parenthesis are the errors at the last digit.

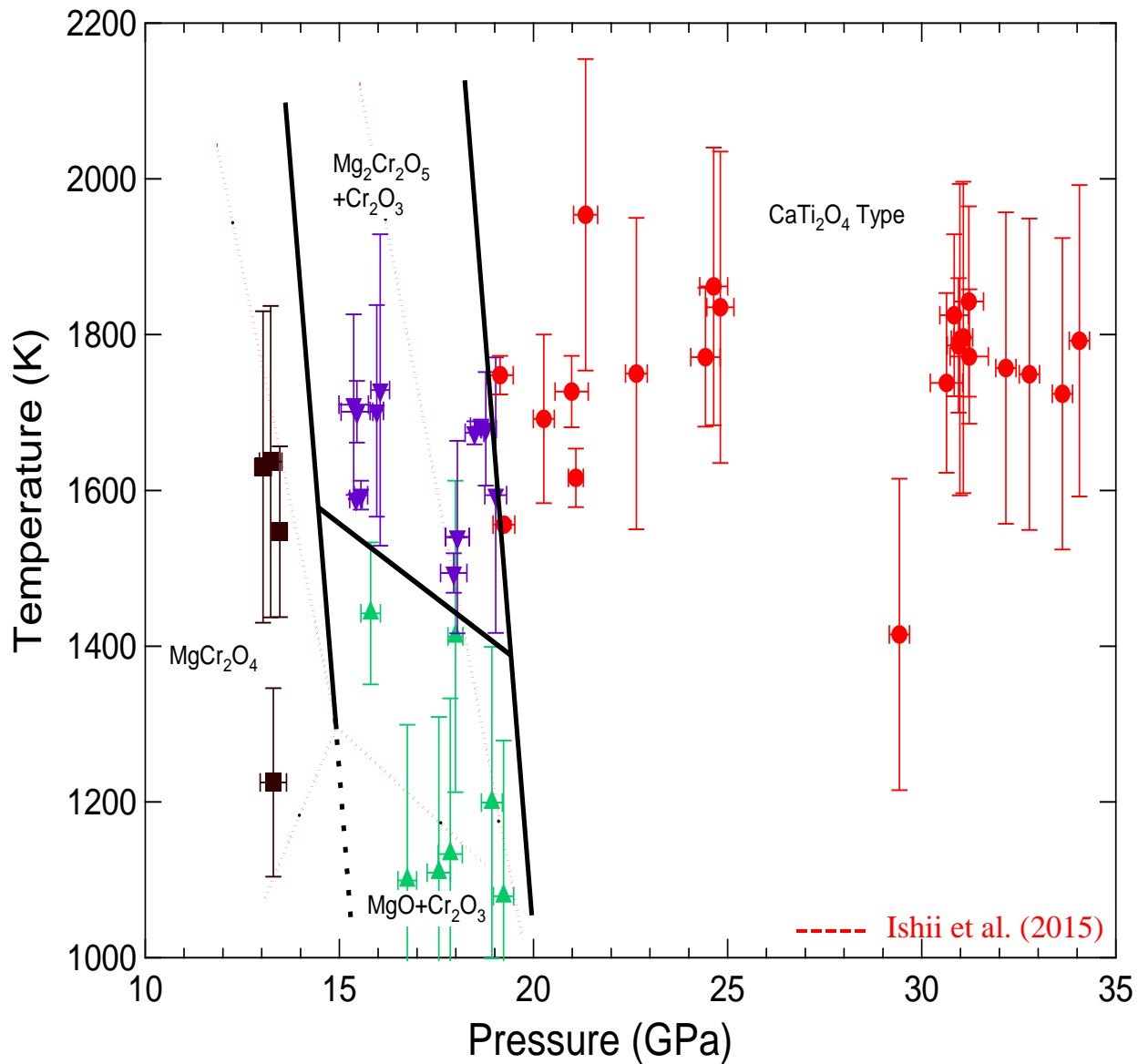


Figure 3.3: Phase diagram of MgCr_2O_4 . Solid black lines represent the phase boundary from our LHDAC experiment. Dashed red lines represent the phase boundary reported by Ishii et al (2015).

Table 3.2: Lattice parameters, symmetry and space group of different phases obtained from MgCr_2O_4 at ambient conditions.

Phase	MgCr_2O_4	MgCr_2O_4	$\text{Mg}_2\text{Cr}_2\text{O}_5$	CaTi_2O_4 type	MgO	Cr_2O_3
Symmetry	Cubic	Tetragonal	Orthorhombic	Orthorhombic	Cubic	Hexagonal
Space group	$Fd\bar{3}m$	$I4_1/amd$	$Pbam$	$Cmcm$	Fm3m	$R\bar{3}c$
a_0 (Å)	8.33324(4)	6.06301(7)	9.62031(4)	2.86465(8)	4.21124(7)	4.96527(8)
b_0 (Å)	8.33324(4)	6.06301(7)	12.387304(7)	9.51504(5)	4.21124(5)	4.96527(6)
c_0 (Å)	8.33324(4)	6.84422(3)	2.842901(6)	9.69811(6)	4.21124(4)	13.55127(4)

Table 3.3: Lattice parameters, symmetry and space group of different phases reported from references for MgCr_2O_4 at ambient conditions. But the Tetragonal MgCr_2O_4 is at 22.5GPa.

Phase	MgCr_2O_4	MgCr_2O_4	$\text{Mg}_2\text{Cr}_2\text{O}_5$	CaTi_2O_4 type	MgO	Cr_2O_3
Source	Lenaz et al., (2004)	Yong et al., (2012)	Ishii et al., (2015)	Ishii et al., (2015)	Sasaki et al. (1979)	Newham et al. (1962)
Symmetry	Cubic	Tetragonal	Orthorhombic	Orthorhombic	Cubic	Hexagonal
Space group	$Fd\bar{3}m$	$I4_1/amd$	$Pbam$	$Cmcm$	Fm3m	$R\bar{3}c$
a_0 (Å)	8.3332 (5)	6.063 (1)	9.62894(7)	2.85107(2)	4.217 (1)	4.7589
b_0 (Å)	8.3332 (5)	6.063 (1)	12.4625(1)	9.48930(8)	4.217 (1)	4.7589
c_0 (Å)	8.3332 (5)	6.895 (3)	2.85644(5)	9.67853(8)	4.217 (1)	12.991

3.3. Discussion

Dissociation of MgCr_2O_4 to Cr_2O_3 and MgO was observed at ~ 15 GPa and temperature below ~ 1500 K. Upon heating to higher temperature, which is above ~ 1500 K, Cr_2O_3 and MgO joined together in 1:2 ratios to form $\text{Mg}_2\text{Cr}_2\text{O}_5$, which is a new phase. This makes the mixture of $\text{Mg}_2\text{Cr}_2\text{O}_5$ and Cr_2O_3 as the stable phase at this P-T range. At pressure above 20 GPa, only a single phase, CaTi_2O_4 type structure (CT) was observed at the temperature of 1400-2000 K. Our phase diagram (Figure.3.3) is very similar to that of the phase diagram from Ishii et al (2015), but there are some differences. Our boundary between $\text{Cr}_2\text{O}_3+\text{MgO}$ and $\text{Mg}_2\text{Cr}_2\text{O}_5+\text{Cr}_2\text{O}_3$ is at slightly higher temperatures and the CaTi_2O_4 type structure formed at slightly higher pressures. These discrepancies may be due to the uncertainties of pressure and temperature measurements in high pressure and high temperature study. In LHDAC, we measured the pressure using gold peaks and temperature by measuring light emission from the heated spot. Ishii et al. (2015) performed the synthesis experiment using a multi-anvil press apparatus mentioning that there was no correction done for pressure effect on electromotive force of the thermocouple, which may cause this minor difference. These discrepancies may also result from the kinetic issue in laser heating diamond anvil cell technique (LHDAC). We heated the sample about half an hour for each heating cycles. Because the transformation to the new HP-HT phase takes a longer time close to the boundary, there may need a longer heating at the sample. But the important thing is that the high pressure and high temperature polymorphs yielded from our experiments of MgCr_2O_4 are same polymorphs reported by Ishii et al. (2015), and the boundaries between different polymorphs determined from two independent experiments are also of similar patterns.

Chapter 4

4. Equation of State of CaTi_2O_4 type structure of MgCr_2O_4

High pressure and high temperature experiments of synthetic magnesiochromite (MgCr_2O_4) were performed at GSECARS, 13-ID-D, Advanced Photon Source (APS) of Argonne National Laboratory (ANL). In order to determine the equation of State of CaTi_2O_4 type structure (CT) of MgCr_2O_4 , CaTi_2O_4 type structure was synthesized at high pressure (~45 GPa) and high temperature (~1800 K). Synthesized CaTi_2O_4 type structure of magnesiochromite was then decompressed from 45 GPa to ambient conditions and a great number of XRD patterns has been collected during the decompression stage (Figure.4.1).

4.1. Experiment

Synthesized MgCr_2O_4 first ground to fine powder and mixed with ~10 wt.% gold for use as a pressure calibrant. Mixtures of the sample and gold were then loaded into the ~150 μm hole of a rhenium gasket. Neon gas was also loaded to use as a pressure medium with the GSECARS high-pressure gas loading system. The samples were probed with a monochromatic X-ray beam $3 \times 3 \mu\text{m}^2$ in cross-section and 0.3344 Å in wavelength, whereas the cross-section of laser heating spot was $20 \times 20 \mu\text{m}^2$. The X-ray beam was ensured to be in the center of the heating spot by carefully aligned the optical paths using fluorescence generated by the X-rays as they passed through the sample. The 2-dimensional CCD detector used to collect the pattern of rings of diffracted X-rays of various diameters of the crystals. The sample-to-detector distance and orientation of the detector was calibrated using CeO_2 powder.

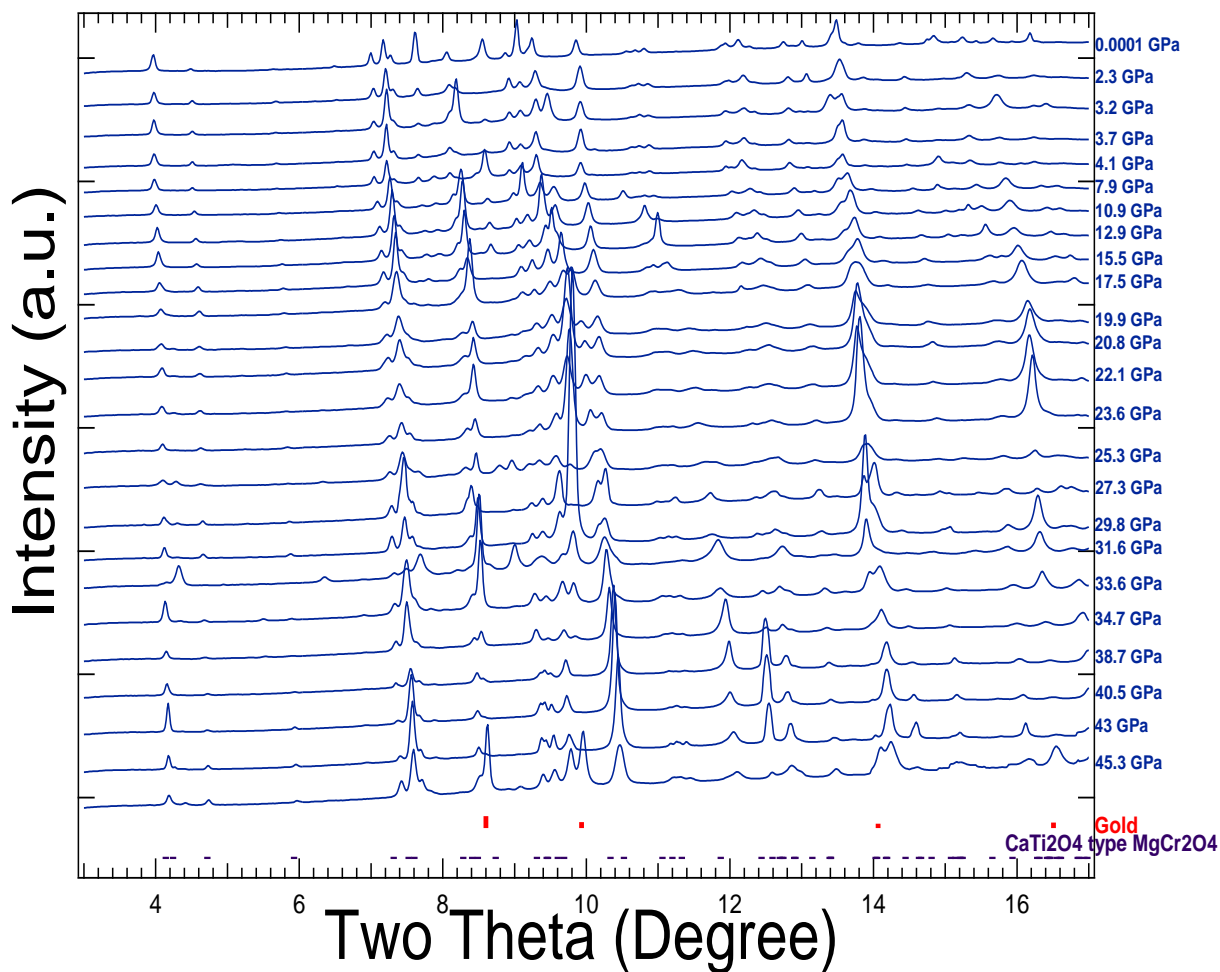


Figure.4.1: Synthesis of CaTi_2O_4 type structure of magnesiochromite was decompressed from 45 GPa to ambient conditions.

4.2. Results

The cubic MgCr_2O_4 spinel structure transformed completely to an orthorhombic CaTi_2O_4 type structure ($Cmcm$) at ~ 45 GPa and ~ 1800 K under hydrostatic condition. The lattice parameters for the CaTi_2O_4 type structure at 45.3(3) GPa are $a = 2.69714(3)$ Å, $b = 9.00774(4)$ Å, and $c = 9.15484(8)$ Å.

The observed peak position, and calculated peak position of CaTi_2O_4 type structure of magnesiochromite at ambient conditions has been shown in Appendix A2. The lattice parameters for the CaTi_2O_4 type structure of MgCr_2O_4 at ambient conditions are $a_0 = 2.86464(8)$ Å, $b_0 =$

9.51504(5) Å, and $c_0 = 9.6981(6)$ Å. Obtained unit-cell lattice parameters at ambient conditions are slightly higher than those determined by Ishii et al. (2015) ($a_0 = 2.85107(2)$ Å, $b_0 = 9.48930(8)$ Å and $c_0 = 9.67853(8)$ Å), but close enough to confirm the synthesis of CaTi_2O_4 type structure. The crystal structure of CaTi_2O_4 -type MgCr_2O_4 has been drawn using XtalDraw with structural refinement data from Ishii et al. (2015) (Figure 4.2). The unit-cell parameters and the volume of synthesised CaTi_2O_4 type MgCr_2O_4 at different pressures are presented in table 4.1. Numbers in the parenthesis are the errors at the last digit.

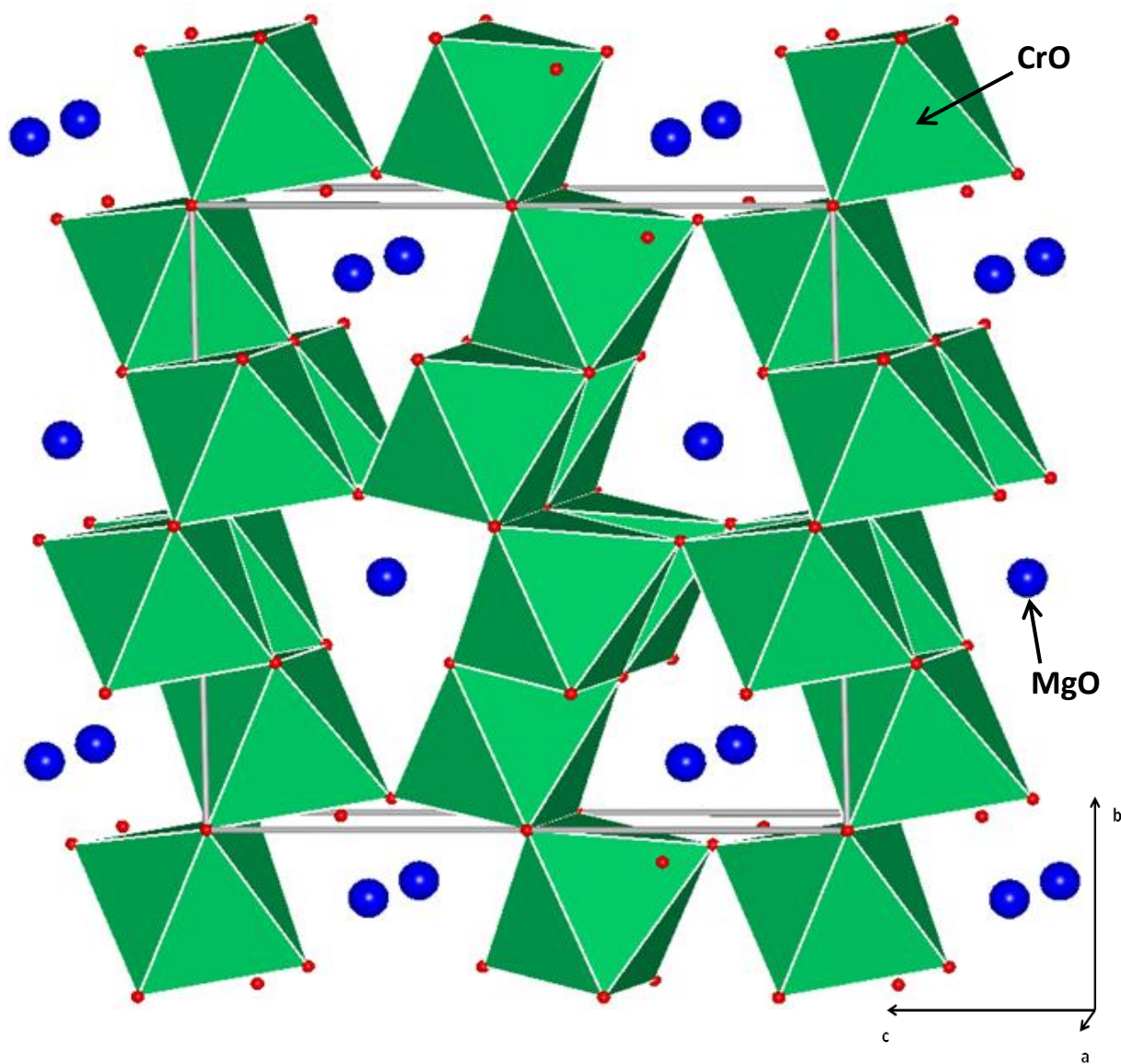


Figure 4.2: Crystal structure of CaTi₂O₄-type MgCr₂O₄ in b-c planes. Solid silver lines represent the unit cell. Blue spheres are Magnesium, green polyhedra are Chromium, and red spheres are Oxygen. (Structure adapted from Ishii et al., 2015)

Table 4.1: Unit-cell parameters of synthesised CaTi₂O₄ type MgCr₂O₄ at different pressure

P (GPa)	a (Å)	b (Å)	c (Å)	V (Å³)
0.0001	2.86464 (8)	9.51504 (5)	9.6981 (6)	264.343 (8)
2.3 (2)	2.85109 (7)	9.48029 (2)	9.6627 (5)	261.175 (5)
3.2 (3)	2.84533 (3)	9.46918 (6)	9.64956 (7)	259.988 (6)
3.7 (2)	2.84172 (5)	9.46508 (2)	9.63926 (4)	259.268 (6)
4.1 (2)	2.84002 (4)	9.45863 (3)	9.63453 (4)	258.81 (1)
7.9 (2)	2.82134 (2)	9.41101 (3)	9.5711 (7)	254.129 (7)
10.9 (2)	2.80841 (2)	9.36937 (6)	9.52618 (2)	250.663 (6)
12.9 (3)	2.80038 (7)	9.34292 (7)	9.49741 (6)	248.488 (3)
15.5 (3)	2.79082 (8)	9.31014 (7)	9.46331 (5)	245.884 (8)
17.5 (2)	2.78107 (2)	9.2924 (4)	9.43709 (4)	243.881 (8)
20.0 (2)	2.77295 (2)	9.26504 (5)	9.41066 (2)	241.774 (7)
20.8 (2)	2.76834 (3)	9.25479 (5)	9.40235 (7)	240.892 (7)
22.1 (2)	2.76457 (6)	9.24438 (3)	9.38177 (5)	239.767 (8)
23.6 (2)	2.75812 (4)	9.22226 (6)	9.37078 (6)	238.356 (9)
25.3 (2)	2.75384 (3)	9.20848 (6)	9.3467 (2)	237.02 (6)
27.3 (2)	2.74699 (3)	9.184 (8)	9.32012 (7)	235.131 (2)
29.8 (2)	2.74011 (5)	9.16358 (5)	9.28982 (3)	233.26 (4)
31.6 (2)	2.73261 (5)	9.14099 (4)	9.27891 (6)	231.779 (5)
33.6 (2)	2.72758 (7)	9.12619 (7)	9.24748 (7)	230.192 (6)
34.7 (2)	2.72306 (2)	9.11813 (6)	9.23769 (5)	229.365 (5)
38.7 (2)	2.71211 (7)	9.08071 (7)	9.21051 (3)	226.835 (4)
40.5 (3)	2.7099 (7)	9.05589 (3)	9.19153 (4)	225.565 (6)
43.0 (1)	2.70313 (2)	9.03312 (3)	9.16803 (5)	223.862 (6)
45.3 (3)	2.69714 (3)	9.00774 (4)	9.15484 (8)	222.418 (3)

The change of volume with pressure for CaTi_2O_4 type structure of MgCr_2O_4 has been shown in Figure 4.4. Normalized pressure vs. Eulerian strain graphs also shown (Figure 4.3) in order to confirm the value of the pressure derivative of the isothermal bulk modulus K_0' . Normalized pressure vs. Eulerian strain gives a horizontal line meaning the K_0' is 4. It is to mention that an upward trend would make it more than 4 and a downward trend makes it less than 4. As the K_0' is 4, we can fit our volume-pressure data with second order Birch-Murnaghan EOS. EOS drawn by Ishii et al. (2015) for CaTi_2O_4 type structure of FeCr_2O_4 also showed in the same figure for comparison. The variation of lattice parameters with pressure of CaTi_2O_4 type structure plotted in Figure 4.5.

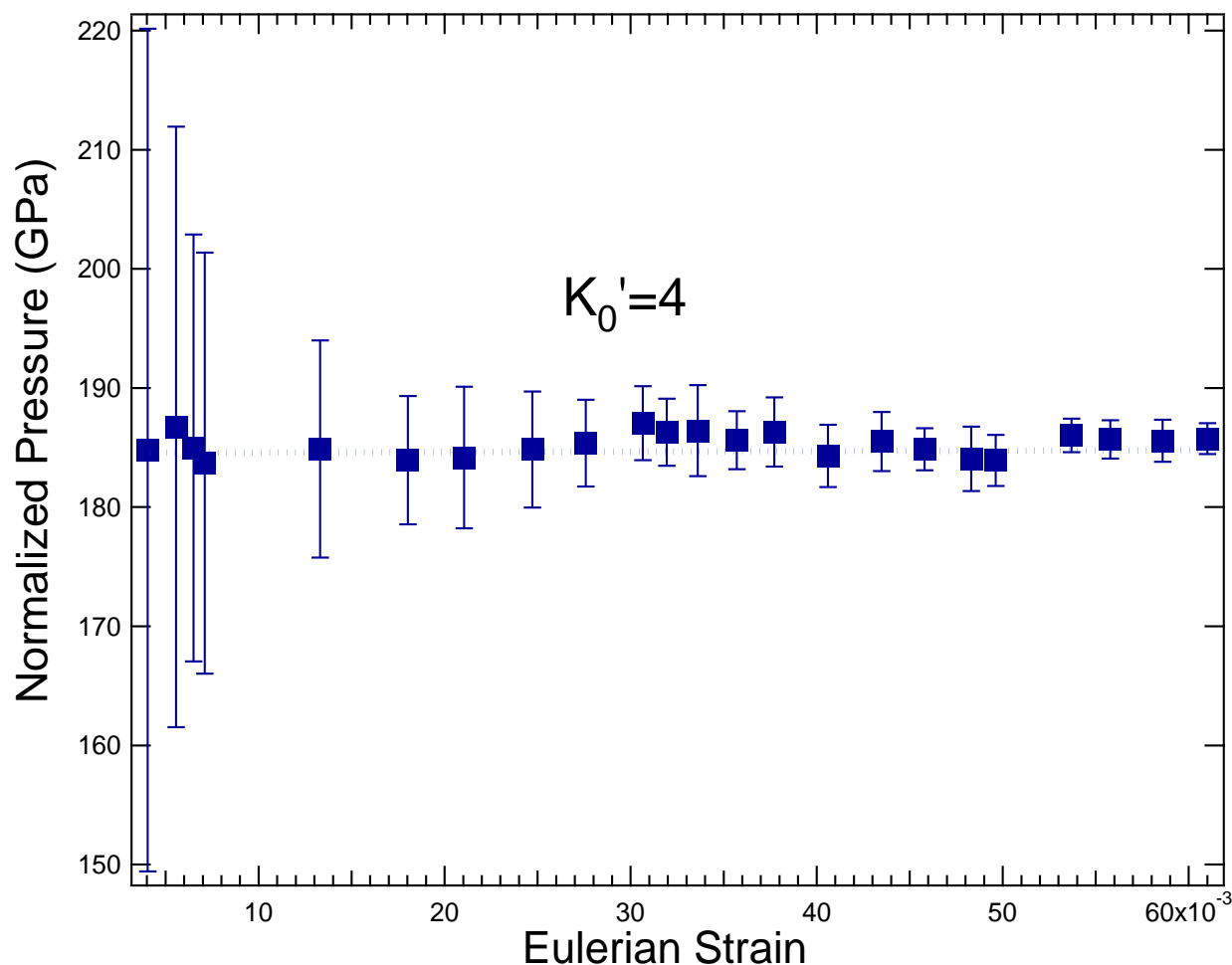


Figure 4.3: Normalized pressure vs. Eulerian Strain plot of CaTi_2O_4 type structure of MgCr_2O_4

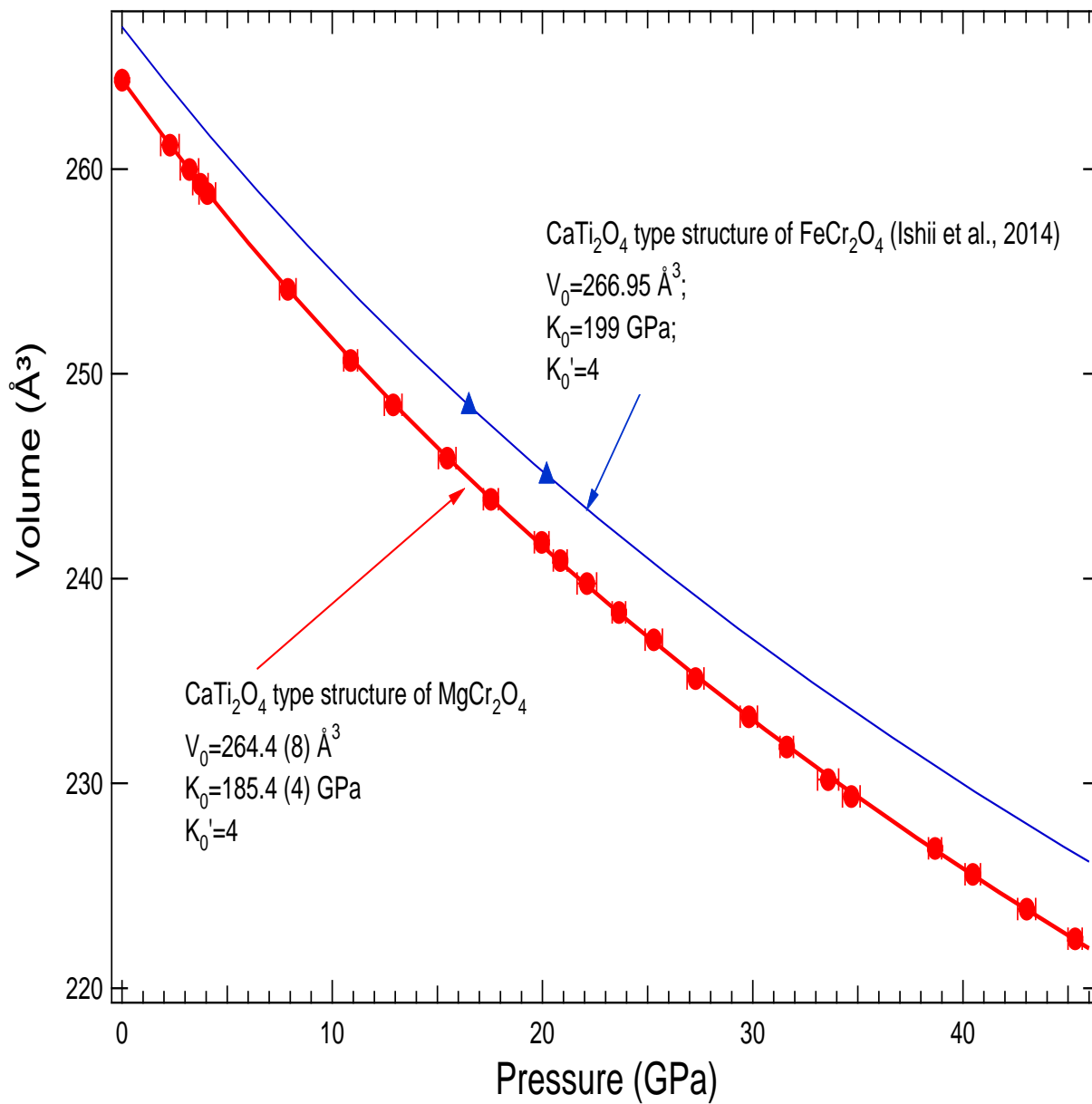


Figure 4.4: Equation of State of CaTi₂O₄ type structure of MgCr₂O₄. Red circles are P-V data and red line is the second order Birch-Murnagahan EOS fitting. Blue solid line is the EOS drawn by Ishii et al. (2014) for CaTi₂O₄ type structure of FeCr₂O₄

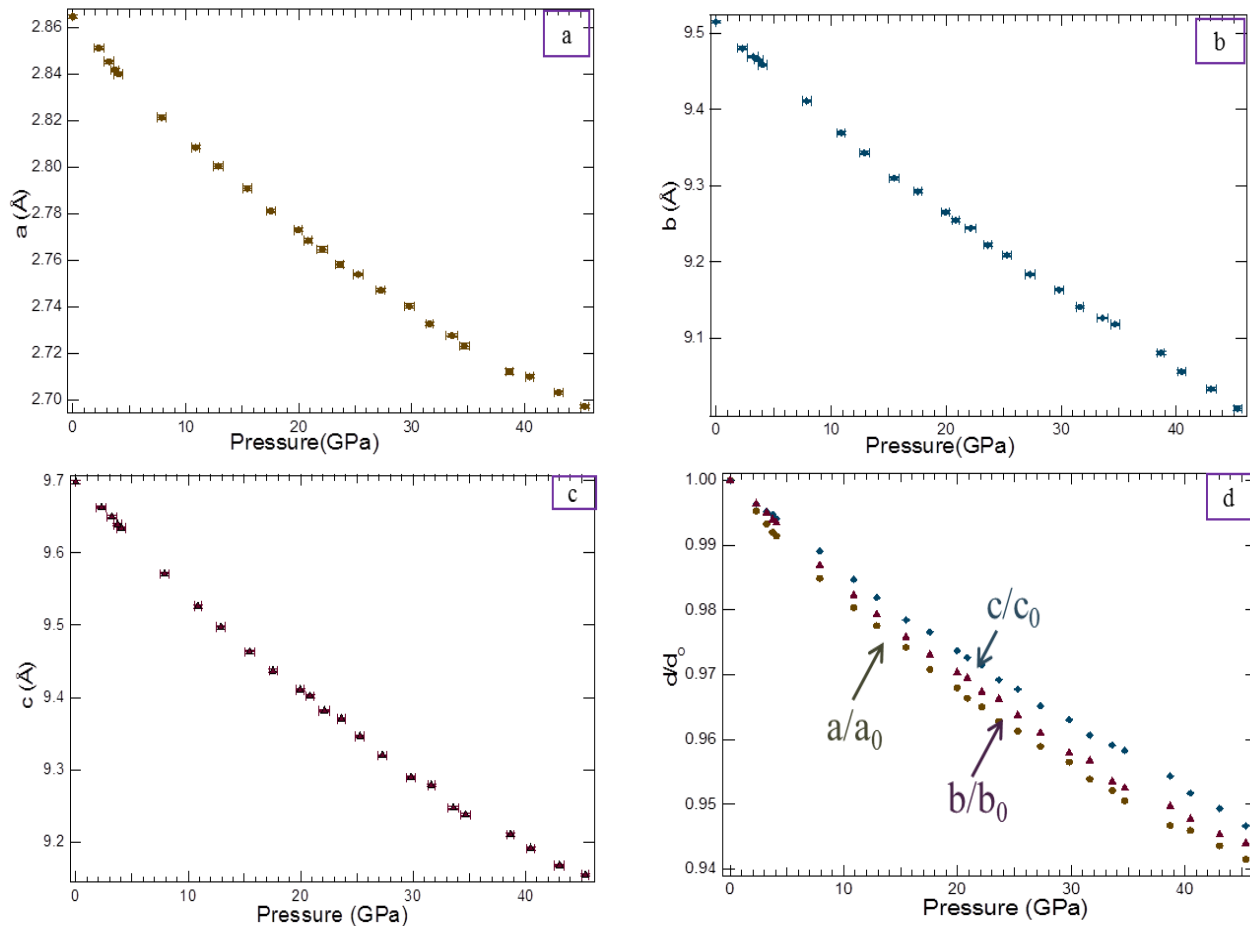


Figure 4.5: Variations of unit-cell lattice parameters with pressures for CaTi₂O₄ type structure of MgCr₂O₄ (a) a-parameter variation with pressure (b) b-parameter variation with pressure (c) c-parameter variation with pressure (d) variation of unit cell dimensions [red circle (a/a_0), Green rectangle (b/b_0), Blue triangle (c/c_0)] with pressure.

4.3. Discussion

From the Figure 4.3, normalized pressure vs. Eulerian strain showed horizontal relationship. So, we can determine the pressure derivative of the isothermal bulk modulus K_0' to be 4. This allows us to fit the volume-pressure data with second order Birch-Murnaghan EOS. The fitting yield $V_0 = 264.4 (8) \text{ \AA}^3$, $K_0 = 185.4 (4) \text{ GPa}$. The fitting curve along with pressure-volume data has been shown in Figure 4.4. Shift to the lower volume and pressure range of our EOS fitting curve then that determined by Ishii et al. (2015) indicates that the volume in each pressure step is lower

for CaTi_2O_4 type structure of MgCr_2O_4 than CaTi_2O_4 type structure of FeCr_2O_4 . The variations of lattice parameters with pressures of CaTi_2O_4 type structure plotted in Figure 4.5. All three unit cell parameters yield nicely fitted smooth curves. The decreasing magnitude of the unit cell parameters are slightly different from one another (Figure 4.5.d), suggesting the phase exhibit only weak anisotropy in compression behavior.

Chapter 5

5. Equation of State of modified ludwigite-type (mLd type)

Mg₂Cr₂O₅ phase

High pressure high temperature experiments of synthetic magnesiochromite (MgCr₂O₄) were performed at GSECARS, 13-ID-D, Advanced Photon Source (APS) of Argonne National Laboratory (ANL). In order to determine the Equation of State of mLd-type Mg₂Cr₂O₅, synthesis experiment has been performed at the stable conditions (P = ~16 GPa and T = ~1500 K) of mLd-type Mg₂Cr₂O₅ phase. Synthesized mLd-type Mg₂Cr₂O₅ phase was then decompressed from 16.2 GPa to ambient conditions and a great number of XRD patterns has been collected during the decompression stage (Figure.5.1).

5.1. Experiment

Synthesized MgCr₂O₄ first ground to a fine powder and mixed with ~10 wt.% gold for use as a pressure calibrant. Mixtures of the sample and gold were then loaded into the ~150 μm hole of a rhenium gasket. Neon gas was also loaded to use as a pressure medium with the GSECARS high-pressure gas loading system. The samples were probed with a monochromatic X-ray beam 3×3 μm² in cross-section and 0.3344 Å in wavelength, whereas the cross-section of laser heating spot was 20×20 μm². The X-ray beam was ensured to be in the center of the heating spot by carefully aligned the optical paths using fluorescence generated by the X-rays as they passed through the sample. The 2-dimensional CCD detector used to collect the pattern of rings of diffracted X-rays of various diameters of the crystals. The sample-to-detector distance and orientation of the detector was calibrated using CeO₂ powder.

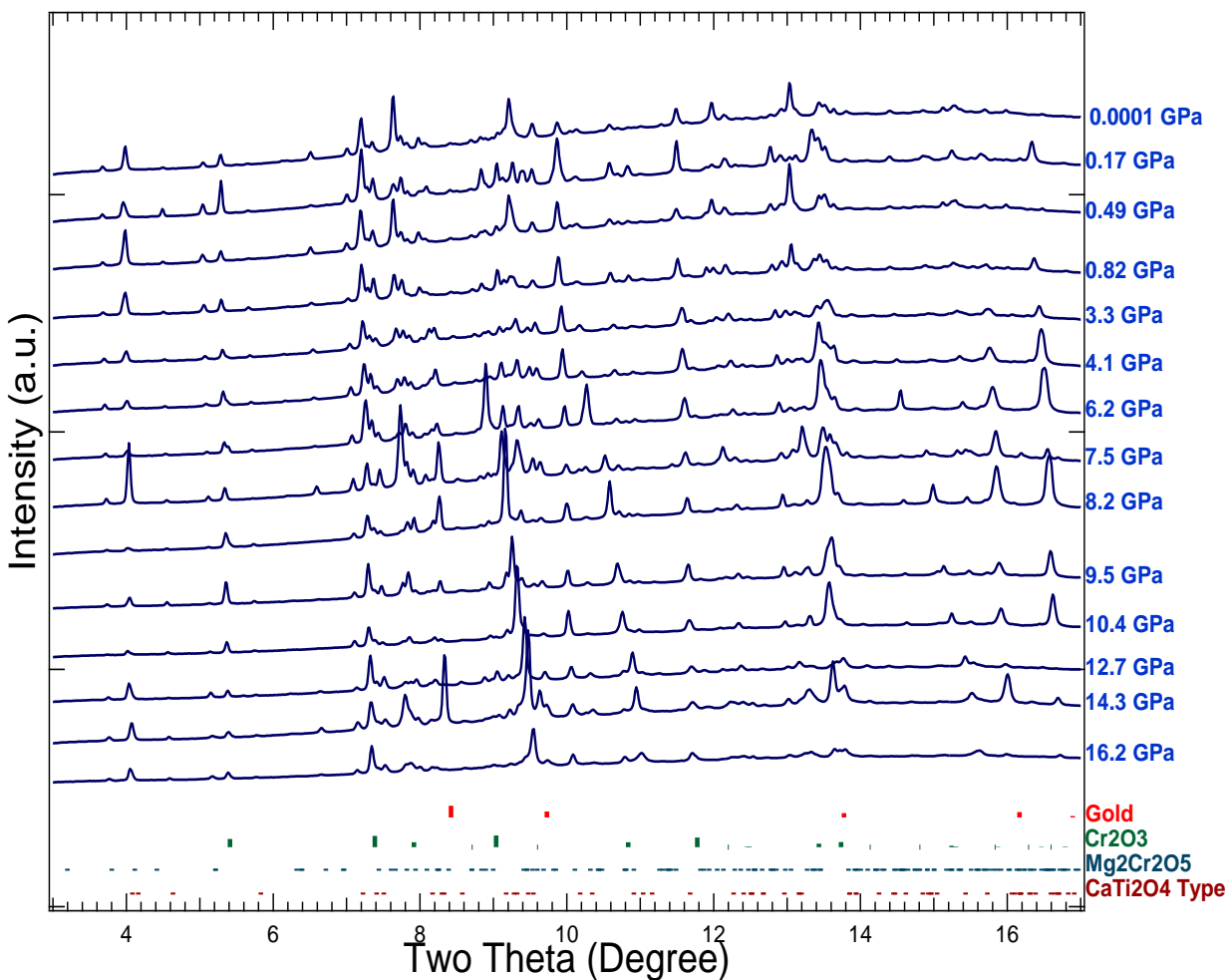


Figure 5.1: Synthesis of $\text{Mg}_2\text{Cr}_2\text{O}_5$ and Cr_2O_3 phases was decompressed from 16 GPa to ambient conditions

5.2. Results

From our experiments, the synthesized mLd-type $\text{Mg}_2\text{Cr}_2\text{O}_5 + \text{Cr}_2\text{O}_3$ phase is always mixed with original spinel structure and sometime with CaTi_2O_4 type structure. We assume that the presence of original spinel structure was due to the heating duration (Each of the heating cycle was around 1 hour). If we heated the sample long enough the residual phases would disappear. On the other hand, presence of CaTi_2O_4 type structure was because of the difficulties of keeping the temperature constant in double-sided laser heating technique. The temperature may vary due to the couplings of laser from both sides. In addition, temperature sometime jumped to very high range abruptly during the increasing of the laser power. At some points during heating, the heat

became too high, subsequently causing increase in pressure resulting in a partial synthesis of CaTi_2O_4 type structure in some occasions. The stable pressure range of mLd-type $\text{Mg}_2\text{Cr}_2\text{O}_5$ is also narrow. Due to the high fluctuation of temperature in laser heating technique, it is difficult to obtain pure phase of mLd-type $\text{Mg}_2\text{Cr}_2\text{O}_5$. For our purpose the mixed phase is good enough to determine the Equation of State, as long as the cell parameters are determinable for that specific phase at different pressure.

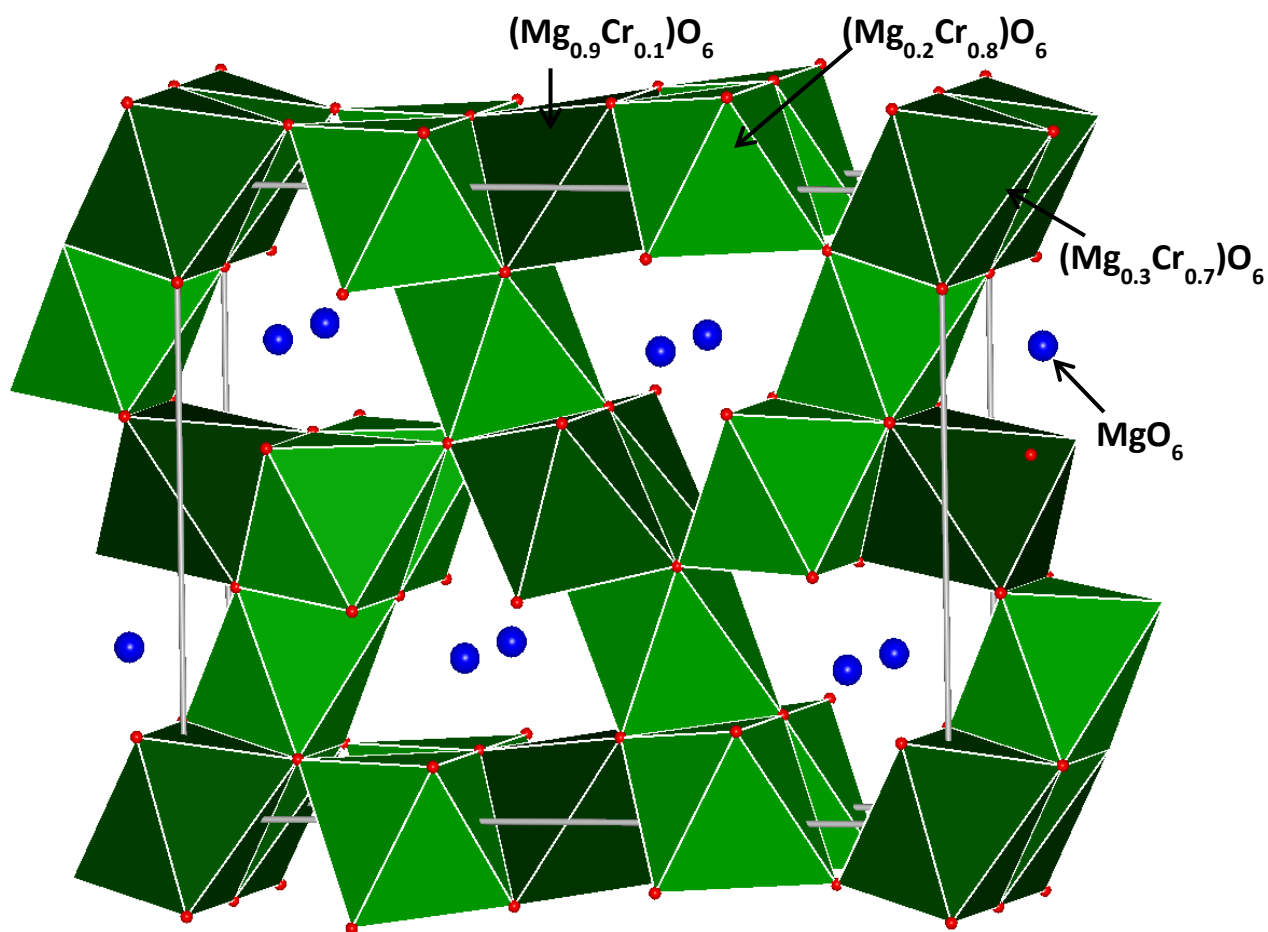


Figure 5.2: Crystal structure of modified ludwigite-type (mLd type) $\text{Mg}_2\text{Cr}_2\text{O}_5$ phase in a-b plane. Solid silver lines represent the unit cell. Blue spheres are Magnesium, different shades of green spheres are Magnesium or Chromium with different probabilities, and red spheres are Oxygen. (Structure adapted from Ishii et al., 2015)

Observed peak position, and calculated peak position of mLd-type $\text{Mg}_2\text{Cr}_2\text{O}_5$, Cr_2O_3 and CaTi_2O_4 type structure of magnesiochromite at ambient condition is shown in Appendix A3. The lattice parameters for the mLd-type $\text{Mg}_2\text{Cr}_2\text{O}_5$ at 16.2(2) GPa are $a = 9.38888(7) \text{ \AA}$, $b = 12.04560(8) \text{ \AA}$, and $c = 2.77967(5) \text{ \AA}$ and at ambient conditions are $a_0 = 9.6203(4) \text{ \AA}$, $b_0 = 12.38730(7) \text{ \AA}$, and $c_0 = 2.84290(6) \text{ \AA}$. Obtained cell parameters at ambient condition are slightly lower than that determined by Ishii et al. (2015) ($a_0 = 9.62894(7) \text{ \AA}$, $b_0 = 12.4625(1) \text{ \AA}$ and $c_0 = 2.85644(2) \text{ \AA}$). Again, the obtained lattice parameters are close enough with published result by Ishii et al. (2015) to confirm the dissociation to $\text{Mg}_2\text{Cr}_2\text{O}_5 + \text{Cr}_2\text{O}_3$. The crystal structure of modified ludwigite-type (mLd type) $\text{Mg}_2\text{Cr}_2\text{O}_5$ phase has been drawn using XtalDraw (Figure 5.2) using the cell refinement data from Ishii et al., 2015.

The dissociation of MgCr_2O_4 phase gives $\text{Mg}_2\text{Cr}_2\text{O}_5$ and Cr_2O_3 . So, we are also able to determine the EOS of Cr_2O_3 phase in order to compare our EOS with the EOS determined by Dera et al. (2011), which will allow verifying our pressure data. Figure 5.2 shows EOS of Cr_2O_3 phase from those same XRD patterns which are used to determine the EOS of mLd-type $\text{Mg}_2\text{Cr}_2\text{O}_5$ phase.

The variations of volume with pressure for mLd-type $\text{Mg}_2\text{Cr}_2\text{O}_5$ phase have been tabulated in Table 5.1, and the EOS has been presented in Figure 5.5. Normalized pressure vs. eulerian strain graphs also drawn (Figure 5.4) in order to confirm the value of the pressure derivative of the isothermal bulk modulus K_0' . Normalized pressure vs. eulerian strain gives a horizontal line meaning the K_0' is 4. Therefore, we fit our volume-pressure data with second order Birch-Murnaghan EOS. The variations of lattice parameters with pressure of mLd-type $\text{Mg}_2\text{Cr}_2\text{O}_5$ phase plotted in Figure 5.6. The decreasing magnitudes of the unit cell parameters are also presented in Figure 5.6.d.

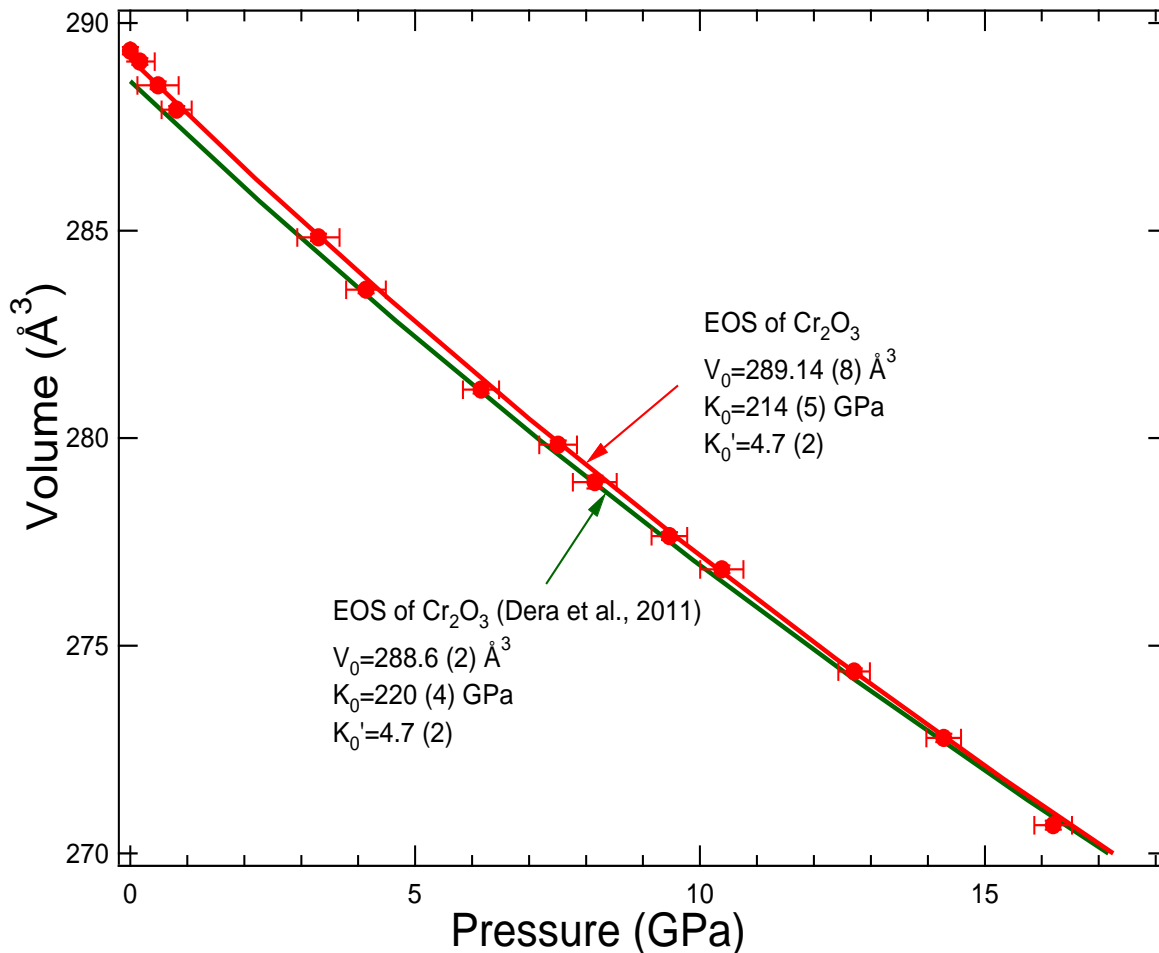


Figure 5.3: Equation of state of Cr_2O_3 . Red circles are P-V data obtained from our sample, and solid red line is Birch-Murnaghan EOS fittings. Solid green curve is the Equation of State of Cr_2O_3 determined by Dera et al (2011).

Table 5.1: Unit-cell parameters of synthesised MgCr₂O₅ type MgCr₂O₄ at different pressure

P (GPa)	a (Å)	b (Å)	c (Å)	V (Å ³)
0.0001	9.6203 (4)	12.38730 (7)	2.84290 (6)	338.9 (8)
0.2 (1)	9.61926 (6)	12.37961 (6)	2.84259 (2)	338.5 (5)
0.5 (1)	9.61345 (4)	12.37276 (8)	2.84102 (8)	337.9 (5)
0.8 (2)	9.60564 (5)	12.36719 (5)	2.83991 (8)	337.4 (6)
3.4 (2)	9.56685 (5)	12.30314 (5)	2.83019 (7)	333.1 (4)

4.2 (3)	9.54813 (4)	12.28661 (7)	2.82699 (6)	331.6 (4)
6.2 (2)	9.51204 (8)	12.24082 (5)	2.82027 (5)	328.4 (5)
7.5 (2)	9.49621 (3)	12.21436 (5)	2.81456 (2)	326.5 (7)
8.2 (3)	9.48551 (5)	12.20129 (6)	2.81196 (7)	325.4 (8)
9.5 (2)	9.46453 (6)	12.17683 (7)	2.80648 (8)	323.4 (6)
10.4 (2)	9.45029 (8)	12.16268 (8)	2.80293 (9)	322.2 (7)
12.7 (2)	9.42255 (8)	12.11934 (8)	2.79285 (7)	318.9 (2)
14.3 (3)	9.40663 (2)	12.08241 (3)	2.78731 (8)	316.8 (8)
16.2 (2)	9.38888 (7)	12.04560 (8)	2.77967 (5)	314.4 (4)

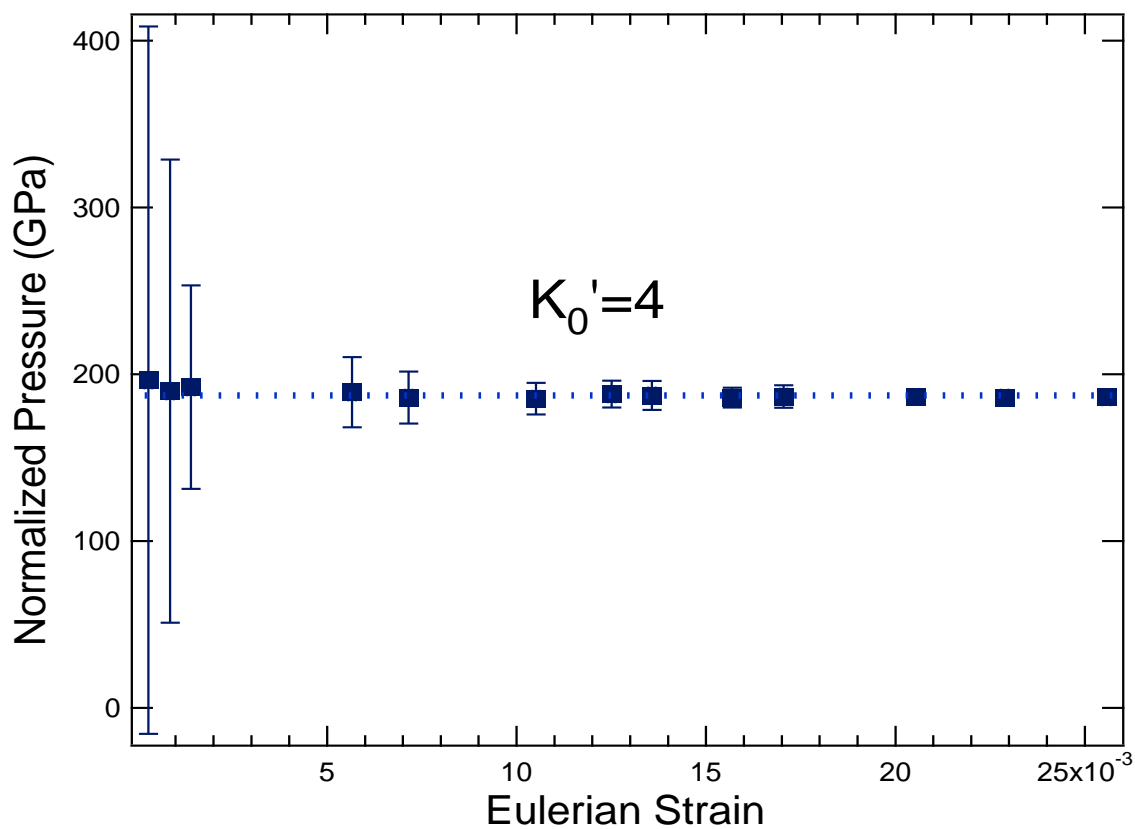


Figure 5.4: Normalized pressure vs. Eulerian Strain plot of $\text{Mg}_2\text{Cr}_2\text{O}_5$ phase

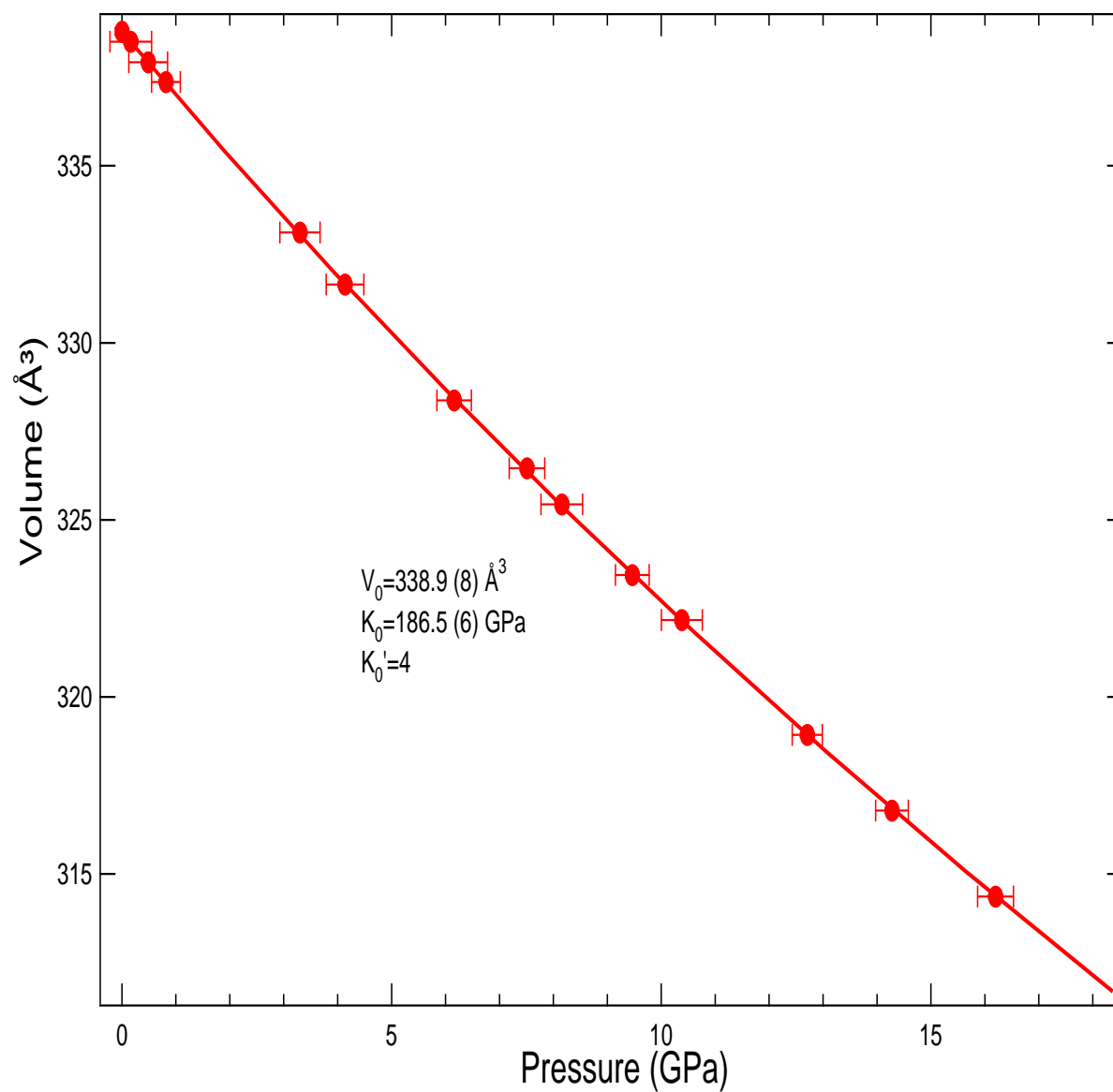


Figure 5.5: Equation of State of Mg₂Cr₂O₅ phase

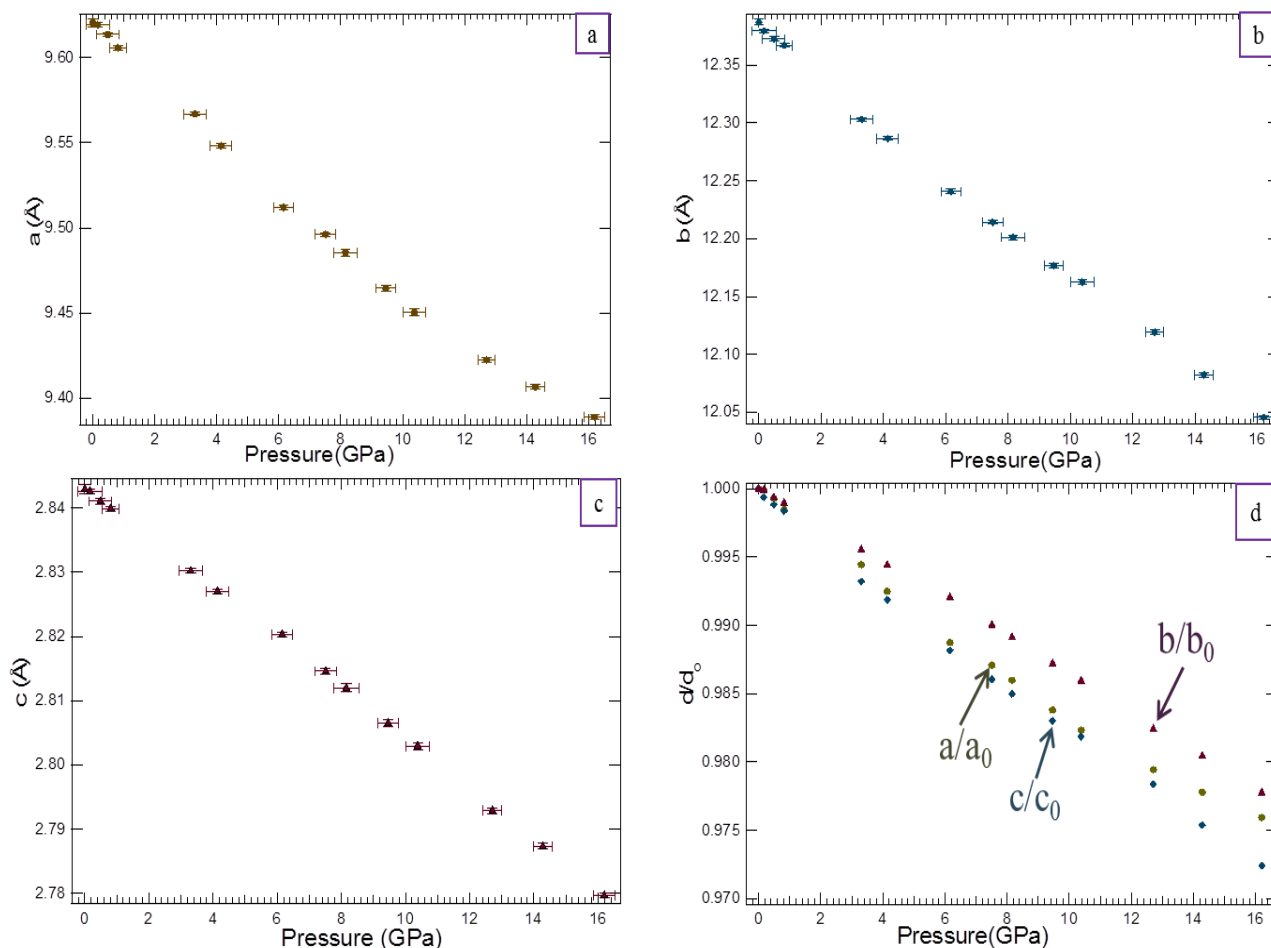


Figure 5.6. Variations of unit cell parameters with pressure (a) a-parameter variation with pressure (b) b-parameter variation with pressure (c) c-parameter variation with pressure (d) variation of unit cell dimensions [red circle (a/a_0), Green rectangle (b/b_0), Blue triangle (c/c_0)] with pressure.

5.3. Discussion

Figure 5.4 shows EOS of Cr_2O_3 phase from those same XRD patterns, which has been used to determine the EOS of mLd-type $\text{Mg}_2\text{Cr}_2\text{O}_5$ phase. The Birch-Murnaghan EOS fittings of our Cr_2O_3 phase yield very similar result to published EOS of Cr_2O_3 by Dera et al. (2011). That gives a higher confidence level to the EOS of mLd-type $\text{Mg}_2\text{Cr}_2\text{O}_5$ phase.

The change in volume with pressure of mLd-type $\text{Mg}_2\text{Cr}_2\text{O}_5$ has been shown in Figure 5.4. Normalized pressure vs. eulerian strain graphs are also drawn (Figure 5.3) in order to confirm the value of the pressure derivative of the isothermal bulk modulus K_0' . Normalized pressure vs. eulerian strain gives a horizontal line, meaning the K_0' is 4. Second order Birch-Murnaghan EOS fitting yield $V_0 = 338.8 (8) \text{ \AA}^3$, $K_0 = 186.5 (6) \text{ GPa}$. The variation of lattice parameters with pressure of $\text{Mg}_2\text{Cr}_2\text{O}_5$ plotted in Figure 5.6. All three unit-cell lattice parameters yield nicely fitted smooth curve. The decreasing magnitude of the unit cell parameters are slightly different with one another (Figure 5.6.d), suggesting the phase exhibit only weak anisotropy in compression behavior.

Chapter 6

6. Equation of State of CaTi_2O_4 type structure of Natural Chromite

High pressure high temperature experiments of natural magnesiochromite (MgCr_2O_4) were performed at GSECARS, 13-ID-D, Advanced Photon Source (APS) of Argonne National Laboratory (ANL). In order to determine the equation of State of CaTi_2O_4 type structure (CT) of natural chromite, CaTi_2O_4 type structure was synthesized at high pressure (~40 GPa) and high temperature (~1800 K). Synthesized CaTi_2O_4 type structure of magnesiochromite was then decompressed from 40 GPa to ambient conditions and numbers of XRD reading has been collected during the decompression stage (Figure.6.1).

6.1. Experiment

The geological location of the natural chromite is Sudbury, which we obtained from Dr. Jordan. Natural chromite first separated from other accessory minerals by picking with needle under microscope. Compositional determination with microprobe showed the presence of Mg, Fe, Al, Cr, and a small amount of Mn and Ti [$\text{Mn}_{0.01}\text{Mg}_{0.52}\text{Fe}_{0.61}\text{Ti}_{0.01}\text{Al}_{0.58}\text{Cr}_{1.3}\text{O}_4$]. Separated chromite then ground to a fine powder and mixed with ~10 wt.% gold for use as a pressure calibrant. Mixtures of the sample and gold were then loaded into the ~150 μm hole of a rhenium gasket. Neon gas was also loaded to use as a pressure medium with the GSECARS high-pressure gas loading system. Two sided laser heating technique was used to heat the sample at high temperatures at GSECARS laser heating facility (Prakapenka et al., 2008). The samples were probed with a monochromatic X-ray beam $3\times 3 \mu\text{m}^2$ in cross-section and 0.3344 \AA in wavelength, whereas the cross-section of laser heating spot was $20\times 20 \mu\text{m}^2$. The X-ray beam was ensured to be in the center of the heating spot by carefully aligned the optical paths using fluorescence generated by the X-rays as they passed through the sample. The 2-dimensional CCD detector used to collect the pattern of rings of diffracted X-rays of various diameters of the crystals. The sample-to-detector distance and orientation of the detector was calibrated using CeO_2 powder.

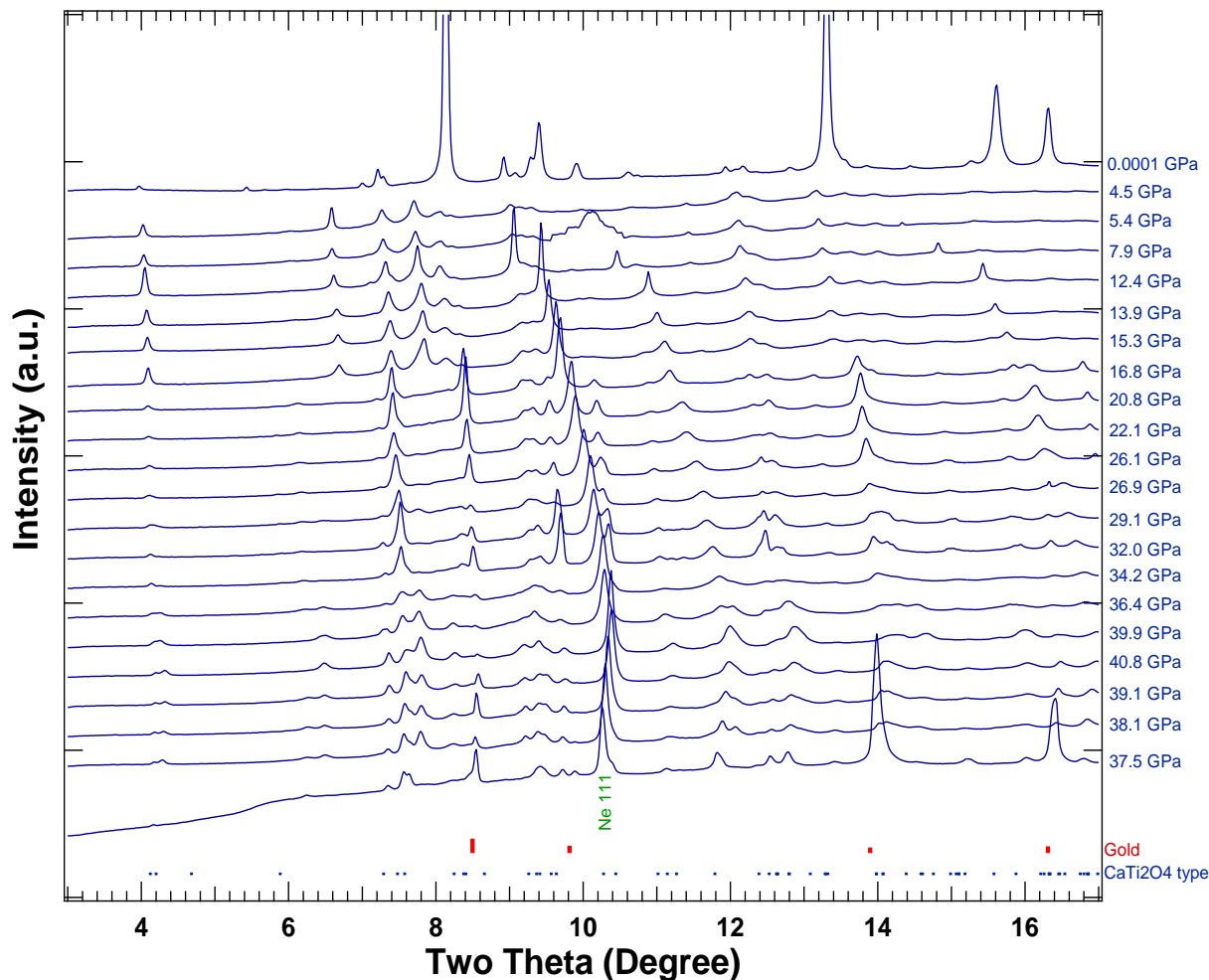


Figure 6.1: Synthesis of CaTi_2O_4 type structure of natural chromite was decompressed from 40 GPa to ambient conditions.

6.2. Results

The cubic chromite spinel structure transformed completely to an orthorhombic CaTi_2O_4 type structure ($Cmcm$) at ~ 40 GPa and ~ 1800 K under hydrostatic condition. The lattice parameters for the CaTi_2O_4 type structure at 40.8(2) GPa are $a = 2.6891(6)$ Å, $b = 8.98896(5)$ Å, and $c = 9.12122(8)$ Å.

The observed peak positions, and calculated peak positions of CaTi_2O_4 type structure of chromite at ambient condition has been shown in Appendix A2. The lattice parameters for the CaTi_2O_4 type structure at ambient conditions are $a_0 = 2.8575(6)$ Å, $b_0 = 9.45065(6)$ Å, and $c_0 =$

9.666412(7) Å. Obtained cell parameters at ambient condition are very similar than those determined by Ishii et al. (2015) ($a_0 = 2.85107(2)$ Å, $b_0 = 9.48930(8)$ Å and $c_0 = 9.67853(8)$ Å), and slightly lower than the cell parameters obtained for the CaTi_2O_4 type structure of MgCr_2O_4 ($a_0 = 2.86464(8)$ Å, $b_0 = 9.51504(5)$ Å, and $c_0 = 9.6981(6)$ Å) in our previous study.

Table 6.1: Unit-cell parameters of synthesised CaTi_2O_4 type of natural chromite at different pressure

P (GPa)	a (Å)	b (Å)	c (Å)	V (Å³)
0.0001	2.8575 (6)	9.45065 (6)	9.66412 (7)	261.0 (1)
4.5 (2)	2.8254 (8)	9.40488 (8)	9.58554 (4)	254.7 (2)
5.4 (2)	2.8221 (2)	9.38405 (6)	9.5733 (5)	253.5 (2)
7.9 (2)	2.8111 (6)	9.34343 (2)	9.53145 (8)	250.3 (2)
12.4 (3)	2.7917 (7)	9.28542 (4)	9.45297 (5)	245.1 (4)
13.9 (3)	2.7843 (7)	9.26591 (8)	9.44125 (5)	243.6 (2)
15.3 (2)	2.7778 (5)	9.25539 (4)	9.41098 (4)	241.9 (1)
16.8 (2)	2.7700 (6)	9.23299 (4)	9.3873 (6)	240.3 (2)
20.8 (3)	2.7553 (4)	9.19116 (7)	9.34332 (7)	236.9 (2)
22.1 (2)	2.7482 (4)	9.17713 (5)	9.32668 (8)	235.5 (3)
26.14 (2)	2.7339 (6)	9.14167 (5)	9.27814 (5)	231.8 (3)
26.9 (3)	2.7289 (2)	9.12821 (7)	9.26427 (4)	231.0 (2)
29.1 (3)	2.7231 (5)	9.10749 (4)	9.24125 (5)	229.4 (3)
32.0 (2)	2.713 (8)	9.07676 (8)	9.21015 (6)	227.0 (2)
34.2 (2)	2.7064 (8)	9.05617 (4)	9.18631 (4)	225.4 (3)
36.4 (3)	2.7024 (6)	9.04155 (5)	9.16928 (8)	223.9 (2)
37.5 (2)	2.6979 (5)	9.02689 (4)	9.15931 (5)	223.2 (3)
38.1 (2)	2.6957 (7)	9.00995 (7)	9.1458 (7)	222.5 (2)
39.1 (3)	2.6943 (6)	9.00693 (3)	9.14168 (7)	222.1 (3)
39.9 (3)	2.6912 (4)	8.99229 (4)	9.12996 (4)	221.3 (2)
40.8 (2)	2.6891 (6)	8.98896 (5)	9.12122 (8)	220.9 (2)

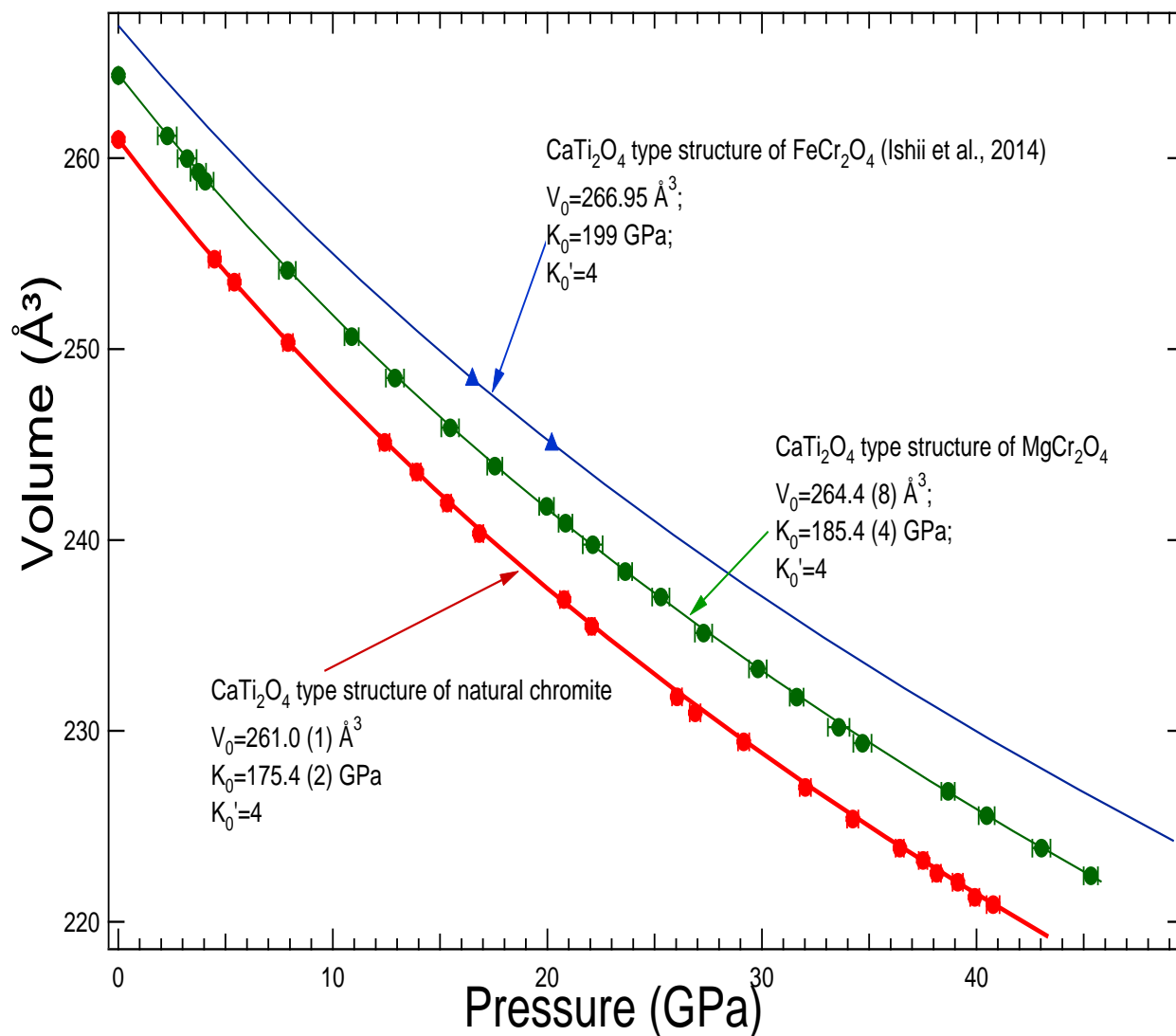


Figure 6.2: Equation of State of CaTi_2O_4 type structure of natural chromite. Red circles are our P-V data and red line is the second order Birch-Murnaghan EOS fitting. Blue solid line is the EOS drawn by Ishii et al. (2015) for CaTi_2O_4 type structure of FeCr_2O_4 , and green solid line is the EOS of CaTi_2O_4 type structure of MgCr_2O_4 , which has been presented in chapter 4.

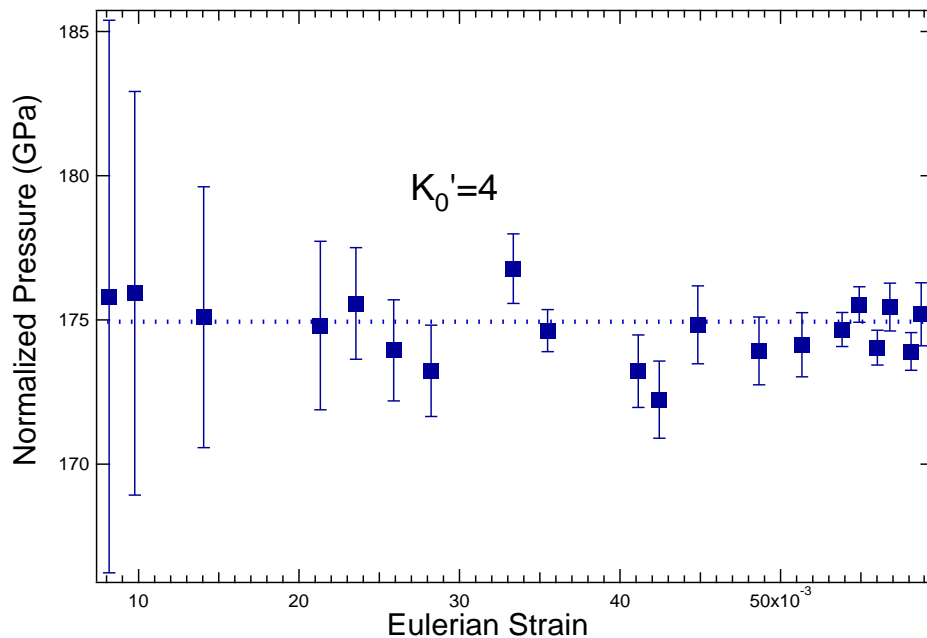


Figure 6.3: Normalized pressure vs. Eulerian Strain plot shows that the derivative of the bulk modulus (K_0') is actually 4.

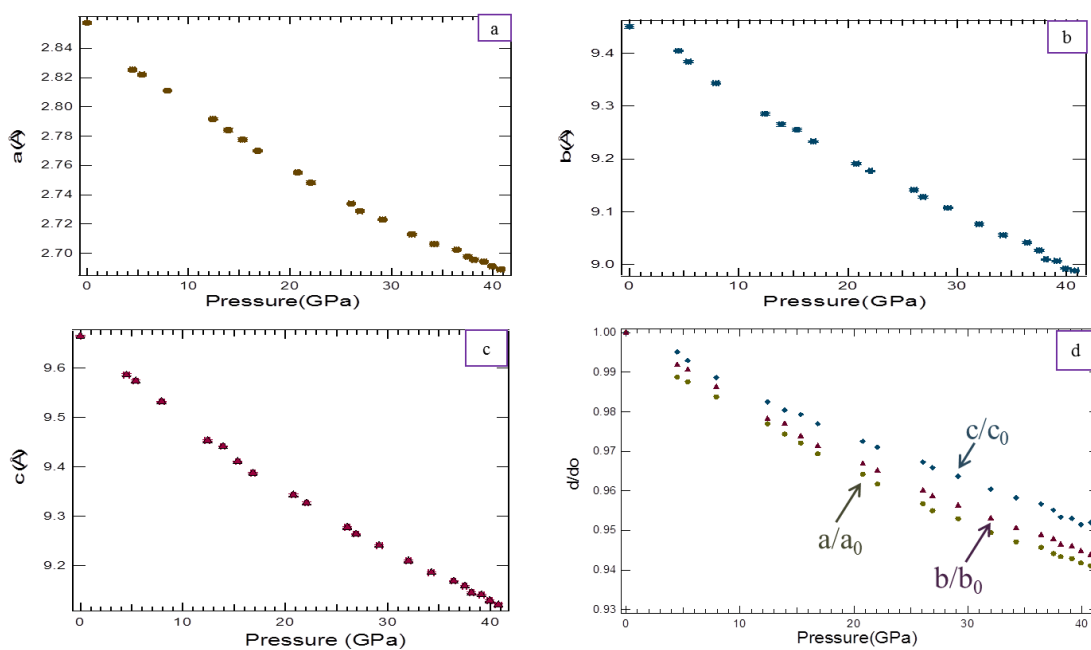


Figure 6.4. Variation of unit cell parameters with pressure (a) a-parameter variation with pressure (b) b-parameter variation with pressure (c) c-parameter variation with pressure (d) variation of unit cell dimensions [red circle (a/a_0), Green rectangle (b/b_0), Blue triangle (c/c_0)] with pressure.

6.3. Discussion

From the Figure 6.3, normalized pressure vs. eulerian strain showed horizontal relationship. So, we can fix the pressure derivative of the isothermal bulk modulus K_0' to 4. This allows us to fit the volume-pressure data with second order Birch-Murnaghan EOS. The fitting yield $V_0 = 261.0$ (1) \AA^3 , $K_0 = 175.4$ (2) GPa. The fitting curve along with pressure-volume data has been shown in Figure 6.2. Comparing the EOS fitting curve of all three CaTi_2O_4 type structure (Figure 6.2) indicates that the volume in each pressure step is lowest in CaTi_2O_4 type structure of natural chromite and highest in CaTi_2O_4 type structure of FeCr_2O_4 . Natural chromite contains Al beside Fe and Mg. Therefore the presence of Al in chromite makes it smallest in volume. On the other hand, if the tetrahedral of chromite totally occupied by Fe that yields the largest volume. Though the presence of Mg in the chromite tetrahedral makes the chromite lower in volume than Fe bearing chromite, but the volume is higher than Al bearing chromite. Sean et al. (2011) found the similar relationship of cations and volume of crystal studying the equation of state of post-perovskites. The variation of lattice parameters with pressure of CaTi_2O_4 type structure plotted in Figure 6.4. All three unit cell parameters yield nicely fitted smooth curve. The decreasing magnitude of the unit cell parameters are slightly different from one another (Figure 6.4.d), suggesting the phase exhibit only weak anisotropy in compression behavior.

Chapter 7

7. Geophysical implications

Researchers (Yang et al., 2007, Yamamoto et al., 2009, and Arai, 2010 & 2013) explained the association of high pressure minerals (diamond, clinopyroxene and coesite) with chromite in the podiform chromitites of the Luobusa ophiolite by the inverse transformation from CT/CF-phase to chromite by mantle upwelling process. They explained that the SiO₂ and CaO components are necessary to be incorporated in the host chromite or its precursor for occurrence of diopsidic clinopyroxene and coesite exsolution lamellae in the chromite. But natural chromite contain only 0.6 wt.%, of SiO₂ and the CaO content is less than several tens of ppm (Arai and Yurimoto, 1994). According to Ishii et al. (2014, 2015), CT/CF-phase can't revert back to a cubic chromite structure during mantle upwelling process. So, they concluded that the formation pressure for the Luobusa ophiolite chromitites is not more than 12-15 GPa (360–450 km deep). But our experiments indicate otherwise.

After synthesis of a CaTi₂O₄ type structure, we heated the sample at lower pressure (Appendix A2). It showed a growing phase of Cr₂O₃ with time. But we didn't manage to find neither the MgO nor Mg₂Cr₂O₅ phase, which are the associated phases with Cr₂O₃ for two different kind of dissociation identified beforehand. So, we suspect the other phase is MgO, which is not identifiable due to the overlapping with the peaks of CaTi₂O₄ type structure. This is an obvious indication of the dissociation back from CT-phase to Cr₂O₃+MgO. If we look very closely at Figure 3.2 and Appendix 1, we can see that the both kind of dissociates phases Cr₂O₃+MgO and Mg₂Cr₂O₅+Cr₂O₃ can move from one stable condition to another. In Figure 3.2, the dissociate phases are Cr₂O₃+MgO at the beginning of heating moving to Mg₂Cr₂O₅+Cr₂O₃ with increasing temperature. In contrast, Mg₂Cr₂O₅+Cr₂O₃ appeared first at high temperature but peak intensity of Mg₂Cr₂O₅ diminishes with increasing intensity of Cr₂O₃ with time during the heating at lower temperatures (Appendix 1). These indicate that the HP-HT polymorphs of magnesiochromite are very likely able to revert back to low pressure - low temperature (LP-LT) phases, if given

enough time. The chemical composition of natural chromite in the Luobusa ophiolite chromitites reported by Yamamoto et al. (2009) is $(\text{Mg}_{0.77}, \text{Fe}^{2+}_{0.22})_{0.99}(\text{Al}_{0.42}, \text{Cr}_{1.46}, \text{Fe}^{3+}_{0.11})_{1.99}\text{O}_4$, which can be approximated as a solid solution of the MgCr_2O_4 - FeCr_2O_4 - MgAl_2O_4 system. So, it is very likely that the HP-HT polymorphs of other spinel group members would show similar behavior. Mantle upwelling is a very slow process, which gives the HP-HT polymorphs of spinel enough time to revert back to LP-LT phases. Therefore, our interpretation is that the formation pressure for the Luobusa ophiolite chromitites is very likely more than 12-15 GPa (360–450 km deep).

We showed in chapter 3, MgCr_2O_4 dissociate to Cr_2O_3 + MgO and $\text{Mg}_2\text{Cr}_2\text{O}_5$ + Cr_2O_3 phases. In contrast FeCr_2O_4 doesn't show Cr_2O_3 + MgO dissociation (Ishii et al. 2014). FeCr_2O_4 dissociates into $\text{Fe}_2\text{Cr}_2\text{O}_5$ + Cr_2O_3 at about 12-16 GPa. At 17–18 GPa, the two dissociate phases combine into CaFe_2O_4 -type below 1600 K and CaTi_2O_4 -type above 1600 K. The MgAl_2O_4 spinel also has been studied at high pressures and high temperatures by Ono et al. (2006). MgAl_2O_4 showed two different decomposed phases MgO + Al_2O_3 at pressure above 15 GPa and $\text{Mg}_2\text{Al}_2\text{O}_5$ + Al_2O_3 at about 20 GPa and 2400 K. Those decomposed phases joined together to form a single phase MgAl_2O_4 of CaFe_2O_4 type structure at around 30 GPa and then transformed to CaTi_2O_4 type structure above 45 GPa. From the above discussion, it is clear that all these three spinels behave slightly differently at high pressure and high temperature (Appendix A8). Only the common HP-HT polymorph in these three different spinel groups is dissociation to mLd type structure ($\text{Mg}_2\text{Al}_2\text{O}_5$ / $\text{Mg}_2\text{Cr}_2\text{O}_5$ / $\text{Fe}_2\text{Cr}_2\text{O}_5$) + oxides (Al_2O_3 / Cr_2O_3). When Mg is present in tetrahedra (MgAl_2O_4 and MgCr_2O_4), it showed the dissociation into two different oxides (MgO + Cr_2O_3 or MgO + Al_2O_3). FeCr_2O_4 doesn't show that kind of dissociation behavior. So, we may logically conclude that Mg is playing the main role for this kind of dissociation. MgCr_2O_4 doesn't show CaFe_2O_4 type structure at high pressure. The absence of either Fe in tetrahedra or Al in octahedral site may not allow the formation of a CaFe_2O_4 type structure. Both of these structural changes in spinel might be due to the ionic radius of different cations (Appendix A7). Fe^{2+} in tetrahedral normally is in high spin state at ambient condition and ionic radius 92 pm, which is bigger than the ionic radius of Mg^{2+} (86 pm). But at HP-HT iron can shift to low spin state (Yamanaka et al., 2008; Lin et al., 2005), when the ionic radius become only 75 pm. It makes the Mg^{2+} largest cation in size at HP-HT condition in spinel group minerals, which may cause the spinel destabilize and dissociates to the constitute oxides. Similarly, Fe^{2+} and Al^{3+} (67.5 pm) is

smaller in size than Mg^{2+} and Cr^{3+} (75.5 pm), respectively. This may give the spinel enough room to transform to CaFe_2O_4 type structure. This explanation can be verified studying the natural spinel samples at high pressure and high temperature, which is a solid solution of different spinel phases $\{(\text{Fe,Mg})(\text{Al,Cr})_2\text{O}_4\}$.

Comparing the Birch-Murnaghan EOS fitting curve of all three CaTi_2O_4 type structure in Figure 6.2 indicates that the volume in each pressure step is highest in FeCr_2O_4 and lowest in natural chromite. Though the presence of Mg in the chromite tetrahedral makes the chromite lower in volume than Fe bearing chromite, but the volume is higher than Al bearing natural chromite. Therefore the presence of Al in chromite also makes it smallest in volume. On the other hand, EOS fitting showed that the CaTi_2O_4 type structure of MgCr_2O_4 $\{K_0 = 185.4 (4) \text{ GPa}\}$ has the lower bulk modulus value than the CaTi_2O_4 type structure of FeCr_2O_4 ($K_0 = 199 \text{ GPa}$) and CaTi_2O_4 type structure of natural chromite $\{K_0 = 175.4 (2) \text{ GPa}\}$. Compressibility is the opposite of bulk modulus. Hence, it may conclude that the presence of Fe in tetrahedra makes the spinel less compressible. Natural chromite contains Al, which indicate that the presence of Al makes the spinel highly compressible in nature.

From the discussion above, it is highly likely that HP-HT polymorphs of chromite bearing spinel are present in the deep mantle. This makes it geologically very important to determine the phase diagram and equation of state of these high pressure Cr-bearing polymorphs. The experimentally calibrated high pressure polymorphs of chromite series minerals could be an ideal pressure gauge for shock-metamorphosed terrestrial rocks and meteorites and also for mantle rocks covering the important pressure range throughout the transition zone. Determination of the isothermal bulk modulus is the first step to determine the other thermodynamics parameter of high pressure polymorphs of MgCr_2O_4 . The newly determined bulk modulus for two high pressure polymorphs of magnesiochromite in this study will be of great help to facilitate the determination of the speed of sound and other mechanical waves in the high pressure form of magnesiochromite.

Chapter 8

8. Conclusion

High pressure high temperature experiments of synthetic magnesiochromite (MgCr_2O_4) were performed up to 40 GPa and 2000 K at GSECARS, 13-ID-D, Advanced Photon Source (APS) of Argonne National Laboratory (ANL) and at X17B3, National Synchrotron Light Source (NSLS) of Brookhaven National Laboratory (BNL) using double sided laser heating diamond anvil cell (LHDAC).

In the HP-HT experiment of MgCr_2O_4 , we observed the dissociation to $\text{Cr}_2\text{O}_3 + \text{MgO}$ at ~ 15 GPa and temperature below 1440 K, and $\text{Mg}_2\text{Cr}_2\text{O}_5 + \text{Cr}_2\text{O}_3$ when the sample heated above 1600 K. At pressure above 20 GPa, only a single phase, CaTi_2O_4 type structure (CT) was observed at the temperature of 1400-2000 K. Our phase diagram is very similar to that of the phase diagram from Ishii et al (2015) with a minor discrepancy. Our boundary between $\text{Cr}_2\text{O}_3 + \text{MgO}$ and $\text{Mg}_2\text{Cr}_2\text{O}_5 + \text{Cr}_2\text{O}_3$ is at slightly high temperature, and the synthesis pressure of CaTi_2O_4 type structure was also slightly higher.

The lattice parameters for the CaTi_2O_4 type structure at ambient conditions are $a_0 = 2.86464(8)$ Å, $b_0 = 9.51504(5)$ Å, and $c_0 = 9.6981(6)$ Å; CaTi_2O_4 type structure of natural chromite are $a_0 = 2.8575(6)$ Å, $b_0 = 9.45065(6)$ Å, and $c_0 = 9.666412(7)$ Å.; and mLd-type $\text{Mg}_2\text{Cr}_2\text{O}_5$ are $a_0 = 9.6203(4)$ Å, $b_0 = 12.38730(7)$ Å, and $c_0 = 2.84290(6)$ Å. Both of the results are similar to that of the lattice parameter reported by Ishii et al. (2015). Fitting the P-V data with Birch-Murnaghan EOS of CaTi_2O_4 type structure of MgCr_2O_4 yields $V_0 = 264.4(8)$ Å³, $K_0 = 185.4(4)$ GPa, $K_0' = 4$; and of CaTi_2O_4 type structure of natural chromite yields $V_0 = 261(1)$ Å³, $K_0 = 175.4(2)$ GPa, $K_0' = 4$. We have also determined the EOS parameter for mLd-type $\text{Mg}_2\text{Cr}_2\text{O}_5$ phase $V_0 = 338.8(8)$ Å³, $K_0 = 186.5(6)$ GPa, $K_0' = 4$. All of the phases showed weak anisotropy in compression behavior. It has been also interpreted that the CT phase of magnesiochromite may revert back to the lower pressure lower temperature phases; support the presence of high pressure high temperature polymorphs of chromite spinel in deep mantle.

Chromite spinel [(Mg, Fe, Al)Cr₂O₄] is a common mineral in many meteorites and mantle rocks. It is also a possible candidate in the lunar crust. High pressure polymorphs of chromite have been observed in a shocked meteorite and it is very likely that those polymorphs of chromite also exist in the earth's mantle. Obtained phase diagram and bulk modulus will be of great help to understand the physical properties of mantle and shock-metamorphosed terrestrial rocks. This data also possibly have implication for the lunar deep interior.

References

Arvanitidis, I., Artin, C., Claeson, P., Jacobsson, H., Johansson, P., Rasmus, J., and Swartling, D., 1996. Study of the Kinetics of Reduction of Iron Chromate by Hydrogen. *Scandinavian Journal of Metallurgy*, Vol. 25, pp. 141-147.

Arai, S., 2010. Chromitites : An Enigmatic Mantle Rock Type. *J.Geography*. Vol, 119 (2), pp. 392-410.

Arai, S., 2013. Conversion of low-pressure chromitites to ultrahigh-pressure chromitites by deep recycling: A good inference. *Earth and Planetary Science Letters*, v. 379, pp. 81–87.

Arai, S., Yurimoto, H., 1994. Podiform chromitites of the Tari-Misaka ultramafic complex, southwestern Japan, as mantle–melt interaction products. *Economic Geology*, Vol. 89, pp. 1279–1288.

Ballhaus, C., Berry, R.F., Green, D.H., 1990. Oxygen fugacity controls in the Earth's upper mantle. *Nature*, Vol. 349, pp. 437-449.

Baublitz, M.A., Arnold, V., and Ruoff, A.L., 1981. Energy Dispersive X-ray Diffraction from High Pressure Polycrystalline Specimens Using Synchrotron Radiation. *Review of Scientific Instruments*, Vol. 52(11), pp. 1616-1624.

Birch, F., 1947. Finite Elastic Strain of Cubic Crystals". *Physical Review*, Vol. 71 (11), pp. 809–824.

Boehler, R., 2000. High Pressure Experiments and the Phase Diagram of Lower Mantle and Core Materials. *Reviews of Geophysics*, Vol. 38(2), pp. 221-245.

Bosi, F., Hålenius, U., and Skogby, H., 2008. Stoichiometry of synthetic ulvöspinel single crystals. *American Mineralogist*, Vol. 93, pp. 1312–1316.

Bragg, W.H.; Bragg, W.L., 1913. The Reflexion of X-rays by Crystals. *Proc R. Soc. Lond. A* Vol. 88 (605), pp. 428–38.

Brister, K., 1997. X-ray Diffraction and Absorption at Extreme Pressures. *Review of Scientific Instruments*, Vol. 68(4), pp. 1629-1647.

Bruno, M.S. and Dunn, K.J., 1984. Stress analysis of a bevelled diamond anvil. *Reu. Sei. Inshum*. Vol. 55, pp. 940-956.

Bulanova, G.P. 1995. The formation of diamond. *Journal of Geochemical Exploration*. Vol. 53, pp. 1–23

Buras, B., Olsen, J.S., Geward, L., Will, G., and Hinze, E., 1977. X-ray energy-dispersive diffractometry using synchrotron radiation. *Applied Crystallographer*, Vol. 10, pp. 431-438.

Catti, M., Freyria, F., Zicovich, C., and Dovesi, R., 1999. High-pressure decomposition of $M\text{Cr}_2\text{O}_4$ spinels (M = Mg, Mn, Zn) by ab initio methods. *Physical Chemistry Miner*, Vol. 26, pp. 389.

Chen, M., Shu, J., Mao, H.K., Xie, X., and Hemley, R.J., 2003(a). Natural Occurrence and Synthesis of Two New Postspinel Polymorphs of Chromite. *Proceedings of the National Academy of Sciences*, Vol. 100 (25), pp. 14651-14654.

Chen, M., Shu, J., Xie, X., Mao, H., 2003(b). Natural CaTi_2O_4 -structured FeCr_2O_4 polymorph in the Suizhou meteorite and its significance in mantle mineralogy. *Geochimica et Cosmochimica Acta*, Vol. 67, pp. 3937-3942.

Chudinovskikh, L., Boehler, R., 2001. High-pressure polymorphs of olivine and the 660-km seismic discontinuity. *Nature*, Vol. 411, pp. 574-577.

Cloutis, E. A., Sunshine, J. M., and Morris, R. V., 2004. Spectral reflectance-compositional properties of spinels and chromites: Implications for planetary remote sensing and geothermometry, *Meteorit. Planet. Sci.*, Vol. 39, pp. 545–565.

Dewaele, A., Loubeyre, P., Mezouar, M., 2004. Equations of state of six metals above 94 GPa. *Phys. Rev.*, Vol. B 70, pp. 094112.

Duke, J., 1983. Ore deposit models 7. magmatic segregation deposits of chromite. *Geosci. Can*, Vol. 10, pp. 15–24.

Dera, B. Lavina, Y. Meng, P. V. B, J., 2011. Structural and electronic evolution of Cr_2O_3 on compression to 55GPa. *Solid State Chem*. Vol. 184, pp. 3040-3055.

Elder, F.R., Gurewitsch, A.M., Langmuir, R.V., and Pollack, H.C., 1947. Radiation from Electrons in a Synchrotron. *Phys. Rev*, Vol. 74, pp. 52-56.

Eremets, M. I., 1996. High Pressure Experimental Methods. *Oxford Science Publications*, ISBN-13: 978-0198562696.

Evans, B.W., and Frost, B.R., 1974. Chrome spinels in progressive metamorphism-a preliminary analysis. *Geochimica et Cosmochimica Acta*, Vol. 39, pp. 959-972.

Fabriès, J., 1979. Spinel-olivine geothermometry in peridotites from ultramafic complexes. *Contrib. Mineral. Petrol.*, Vol. 69, pp. 329-336.

FeCr₂O₄, Iron Chromium Oxide Data Sheet, 1997. *JCPDS-International Center for Diffraction Data, PCPDFWIN*, Vol.:1.30.

Finger LW, Hazen RM, Hofmeister AM, 1986. High-pressure crystal-chemistry of spinel (MgAl₂O₄) and Magnetite (Fe₃O₄) - Comparisons with silicate spinels. *Phys Chem Minerals*, Vol. 13, pp. 215–220.

Finger, L.W., Hazen, R.M., Zou, G., Mao, H.K., and Bell, P.M., 1981. Structure and Compression of Crystalline Argon and Neon at High Pressures and Room Temperature. *Applied Physics Letter*, Vol.39 (11), pp. 892-894.

Forman, R.A., Piermarini, G.J., Barnett, J.D., and Block, S., 1972. Pressure Measurement Made by Utilization of Ruby Sharp-Line Luminescence. *Science*, Vol. 176, pp. 284-286.

Griffin, W.L., and Ryan, C.G., 1995. Trace Elements in Indicator Minerals: Area Selection and Target Evaluation in Diamond Exploration. *Journal of Geochemical Exploration*, Vol. 53, pp. 311-337.

Gu, F. and Wills, B., 1988. Chromite- mineralogy and processing. *Minerals Engineering*, Vol. 1 (3), pp. 235-240.

Haavik, C., Stolen, S., Fjellvag, H., Hanfland, M., and Housermand, D., 2000. Equation of state of magnetite and its high-pressure modification: Thermodynamics of the Fe-O system at high pressure. *American Miner*, Vol. 83, pp. 514.

Hammersley J (1996) Fit2D report. Europe Synchrotron Radiation Facility, Grenoble

Hazen, R.M., and Yang, H., 1999. Effects of cation substitution and order-disorder on P-V-T equations of state of cubic spinels. *American Miner*, Vol. 84, pp. 1956.

Hazen, R.M., and Downs, T., 2000. Reviews in mineralogy, vol 41. *Mineralogical Society of America, Washington D.C. ISBN 0-939950-53-7*

Holland, T.J.B., and Redfern, S.A.T., 1997. Unit cell refinement from powder diffraction data: the use of regression diagnostics. *Mineralogical Magazine*, Vol. 61, pp. 65-77.

Holzappel, W.B., 1984. X-ray Diffraction on Solids Under High Pressure. *Review of Applied Physics*, Vol. 19, pp. 705-713.

Hu, J.Z., Mao, H.K., Shu, J.F., and Hemley, R.J., 1993. The Joint International Association for Research and Advancement of High Pressure Science and Technology and

American Physical Society Topical Group on Shock Compression of Condensed Matter Conference. *AIP, Colorado Springs, Colorado*, pp. 441.

Irifune, T., Fujino, K., and Ohtani, E., 1991. A New High-pressure Form of MgAl_2O_4 . *Nature*, Vol. 349, pp. 409.

Irifune, T., Naka, H., Sanehira, T., Inoue, T., and Funakoshi, K., 2002. In Situ X-ray Observations of Phase Transitions in MgAl_2O_4 Spinel to 40GPa Using Multianvil Apparatus with Sintered Diamond Anvils. *Physics and Chemistry of Minerals*, Vol. 29 (10), pp. 645-654.

Irvine, T., 1965. Chromian spinel as a petrogenetic indicator: part 1. *Theory*. *Can. J. Earth Sci.* Vol. 2, pp. 648–672.

Irvine, T., 1967. Chromian spinel as a petrogenetic indicator: Part 2 Petrologic applications. *Can. J. Earth Sci.* Vol. 4, pp. 71–103.

Ishii, T., Kojitani, H., Tsukamoto, S., Fujino, K., Mori, D., Inaguma, Y., Tsujino, N., Yoshino, T., Yamazaki, D., Higo, Y., Funakoshi, K., Akaogi, M., 2014. High-pressure phase transitions in FeCr_2O_4 and structure analysis of new post-spinel FeCr_2O_4 and $\text{Fe}_2\text{Cr}_2\text{O}_5$ phases with meteoritical and petrological implications. *American Mineralogist*. Vol. 99 (8-9), pp. 1788–1797.

Ishii, T., Kojitani, H., Fujino, K., Yusa, H., Mori, D., Inaguma, Y., Matsushita, Y., Yamaura, K., Akaogi, M., 2015. High-pressure high-temperature transitions in MgCr_2O_4 and crystal structures of new $\text{Mg}_2\text{Cr}_2\text{O}_5$ and post-spinel MgCr_2O_4 phases with implications for ultrahigh-pressure chromitites in ophiolites". *Am. Miner.* Vol. 100(1), pp. 59-65.

Jahren, A.H., Kruger, M.B., and Jeanloz, R., 1992. Alexandrite as a high- temperature pressure calibrant, and implications for the ruby-fluorescence scale. *Journal of Applied Physics*, Vol. 71, pp. 1579-1582.

Jayaraman, A., 1983. Diamond Anvil Cell and High-Pressure Physical Investigations. *Reviews of Modern Physics*, Vol. 55(1), pp. 65-108.

Jephcoat, A.P., 1998. Rare-Gas Solids in the Earth's Deep Interior. *Letters to Nature*, Vol. 393, pp. 355-358.

Kim, B.N., Hiraga, K., Morita, K., and Sakka, Y., 2001. A high-strain-rate superplastic ceramic. *Nature*, Vol. 413, pp. 288.

Kim, D.C., and Ihm, S.K., 2001. Application of Spinel-Type Cobalt Chromite as a Novel Catalyst for Combustion of Chlorinated Organic Pollutants. *Environmental Science and Technology*, Vol. 35, pp. 222-226.

Kojitani, H., Enomoto, A., Tsukamoto, S., Akaogi, M., Miura, H., Yusa, H., 2010. High-pressure high temperature phase relations in MgAl_2O_4 . *J. Phys: Conf. Ser.*, Vol. 215.

Kyono, A., Gramsch, S., Yamanaka, T., Ikuta, D., Ahart, M., Mysen, B., Mao, H.K., Hemley, R., 2012. The influence of the Jahn–Teller effect at Fe^{2+} on the structure of chromite at high pressure. *Phys. Chem. Miner.* Vol. 39, pp. 131–141.

Lenaz, D., Skogby, H., Princivalle, F., Hålenius, U., 2004. Structural changes and valence states in the MgCr_2O_4 - FeCr_2O_4 solid solution series. *Physics and Chemistry of Minerals*, Vol. 31, pp. 633-642.

Levy, D., Pavese, A., and Hanfland, M., 2000. Phase transition of synthetic zinc ferrite spinel (ZnFe_2O_4) at high pressure, from synchrotron X-ray powder diffraction. *Physical Chemistry Miner*, Vol. 27, pp. 638.

Lorenzana, H.E., Benaïmias, M., Radousky, H., Kruger, M.B., 1994. Producing Diamond Anvil Cell Gaskets for Ultrahigh-Pressure Applications Using an Inexpensive Electric Discharge Machine. *Review of Scientific Instruments*, Vol. 65 (11), pp. 3540-3543.

Ma, Y., Mao, H.K., Hemley, R.J., Gramsch, S.A., Shen, G., and Somayazulu, M., 2001. Two Dimensional Energy Dispersive X-ray Diffraction at High Pressures and Temperatures. *Review of Scientific Instruments*, Vol. 72 (2), pp. 1302-1305.

Ma, Y., Prewitt, C.T., Zou, G., Mao, H.K., and Hemley, R.J., 2003. High-Pressure High-Temperature X-ray Diffraction of β Boron to 30GPa. *Physical Review B*, Vol. 67, pp.1-6.

Ma, Y., Somayazulu, M., Shen, G., Mao, H.K., Shu, J., and Hemley, R.J., 2004. In Situ X-ray Diffraction Studies of Iron to Earth-Core Conditions. *Physics of the Earth and Planetary Interiors*, Vol. 143-144, pp. 455-467.

Malavasi, L., Tealdi, C., Amboage, M., Mozzati, M.C., and Flor, G., 2005. High Pressure X-ray Diffraction Study of MgMn_2O_4 Tetragonal Spinel. *Journal of Condensed Matter*, Vol. 238, pp. 171–174.

Mao, H.K., 1973-1974. Carnegie Institution Annual Report of the Director, Geophysical Laboratory. pp. 332.

Mao, H.K., Xu, J., and Bell, P.M., 1986. Calibration of the Ruby Pressure Gauge to 800kbar under Quasi-Hydrostatic Conditions. *Journal of Geophysical Research*, Vol. 91 (B5), pp. 4673-4676.

Mao, H.K., Bell, P.M., 1978. High-Pressure Physics - Sustained Static Generation of 1.36 to 1.72 Megabars. *Science*, Vol. 200 (4346), pp. 1145-1147.

Mao, H.K., Bell, P.M., Dunn, K.J., Chrenko, R.M., DeVries, R.C., 1979. Absolute pressure measurements and analysis of diamonds subjected to maximum static pressures of 1.3-1.7 Mbar. *Rev Sci Instrum*. Vol. 50, pp. 1002-1009.

Martinho, H., and others, 2001. Studies of the three-dimensional frustrated antiferromagnetic ZnCr₂O₄. *J. APPL. PHYS.*, 89(11), pp. 7050-7052.

Miletich, R.; Allan, D. R.; Kuhs, W. F.; 2000. High-Pressure Single-Crystal Techniques. *Mineralogical Society of America*, Vol 41(1), pp. 445-519.

Miyahara, S., and Ohnishi, H., 1956. Cation arrangement and magnetic properties of copper ferrite-chromite series. *Journal of the Physical Society of Japan*, Vol. 11, pp. 1296-1302.

Munro, R.G., Piermarini, G.J., Block, S., and Holzappel, W.B., 1985. Model Line- Shape Analysis for the Ruby R Lines Used for Pressure Measurement. *Journal of Applied Physics*, Vol. 52(2), pp. 165-169.

Murnaghan, F.D., 1944. The Compressibility of Media under Extreme Pressures. *Proceedings of the National Academy of Sciences of the United States of America*, Vol. 30, pp. 244-247.

O'Neill, H.S.C., and Navrotsky, A., 1983. Simple spinels; crystallographic parameters, cation radii, lattice energies, and cation distribution. *American Miner*, Vol.68, pp. 181-189.

O'Neill, H.S.C., and Navrotsky, A., 1984. Cation distributions and thermodynamic properties of binary spinel solid solutions. *American Miner*, Vol. 69, pp. 733-742.

O'Neill, H.C. & Wall, V.J., 1987. The olivine-orthopyroxene-spinel oxygen geobarometer, the nickel precipitation curve, and the oxygen fugacity of the Earth's upper mantle. *J. Petrol.*, Vol. 28, pp. 1169-1191.

Ono, S., Kikegawa, T., and Ohishi, Y., 2006. The stability and compressibility of MgAl₂O₄ high-pressure polymorphs. *Phys. Chem. Miner.*, Vol. 33(3), pp. 200–206.

Petric, A., Jacob, K.T., 1982. Thermodynamic Properties of Fe₃O₄-FeV₂O₄ and Fe₃O₄-FeCr₂O₄ Spinel Solid Solutions. *Journal of the American Ceramic Society*, Vol. 65(2), pp. 117-123.

Perinelli C., Bosi F., Andreozzi G.B., Conte A.M., and Armienti P., 2014. Geothermometric study of Cr-rich spinels of peridotite mantle xenoliths from northern Victoria Land (Antarctica). *American Mineralogist*, Vol. 99, pp. 839-846.

Pieters C, Besse S, Boardman J, Buratti B, Cheek L, Clark R, Combe J, Dhingra D, Goswami J, Green R, et al., 2011. Mg-spinel lithology: A new rock type on the lunar farside. *J GEOPHYS RES-PLANETS*, Vol. 116, pp. 14.

Prakapenka V. B., Kubo A., Kuznetsov A., Laskin A., Shkurikhin O., Dera P., Rivers M. L. and Sutton S. R., 2008. Advanced flat top laser heating system for high pressure research at GSECARS: Application to the melting behavior of germanium. *High Pres. Res.*, Vol. 28, pp. 225-235.

Ringwood, A.E., and Ried, A., 1969. High pressure synthesis of some compounds of cadmium. *Earth and Planetary Sciences Letter*, Vol. 6, pp. 245.

Romeijn, F.C., 1953. Physical and crystallographical properties of some spinels. *Philips Reserve Report*, Vol. 8, pp. 304.

Rubin A. E., 1997. Mineralogy of meteorite groups. *Meteoritics & Planetary Science* Vol. 32, pp. 231–247.

Ruoff, A. L., Xia, H., Luo, H., and Vohra, Y.K., 1990. Miniaturization techniques for obtaining static pressures comparable to the pressure at the center of the Earth- X-ray diffraction at 416 GPa. *Review of Scientific Instruments*, Vol. 61(12), pp. 3830-3833.

Sack, R.O., and Ghiorso, M.S., 1991. Chromian spinels as petrogenetic indicators: thermodynamics and petrological applications. *American Mineralogist*, Vol. 76, pp. 827-847.

Sawaoka, A., Saito, S., Inoue, K., and Asada, T., 1971. Effect of High Pressure on the Lattice Constants of Chromites Having The Spinel Structure. *Material Review Bulletin*, Vol. 6 (2), pp. 97-102.

Schollenbruch, K., Woodland, A.B., Frost, D.J., 2010. The stability of hercynite at high pressures and temperatures. *Phys Chem Minerals*, Vol. 37, pp. 137–143.

Shieh, S.R., Dorfman, S.M., Kubo, A., Prakapenka, V.B., Duffy, T.S., (2011) Synthesis and equation of state of post-perovskites in the (Mg, Fe)₃Al₂Si₃O₁₂ system. *Earth Planet. Sci. Lett.*, Vol. 312, pp. 422–428

Shen G. Y., Rivers M. L., Wang Y. B. and Sutton S. R., 2001. Laser heated diamond anvil cell system at the Advanced Photon Source for in situ x-ray measurement at high pressure and temperature. *Rev. Sci. Instrum.*, Vol. 72, pp. 1273-1282.

Shen G. Y., Prakapenka V. B., Eng P. J., Rivers M. L. and Sutton S. R., 2005. Facilities for high-pressure research with the diamond anvil cell at GSECARS. *J. Synch. Rad.*, Vol. 12, pp. 642-649.

Shim, S.H., Duffy, T.S., and Shen, G., 2001. The stability and P–V–T equation of state of CaSiO₃ perovskite in the Earth's lower mantle. *Nature*, Vol. 411, pp. 571.

Speziale, S., Duffy, T.S., and Angel, R.J., 2004. Single-Crystal Elasticity of Fayalite to 12GPa. *Journal of Geophysical Research-Solid Earth*, Vol. 109 (B12), pp. 1-15.

Stachel, T., and Harris, J.W., 2008. The origin of cratonic diamonds – constraints from mineral inclusions. *Ore Geology Reviews*, Vol. 34, pp. 5–32.

Tathavadkar, V.D., Antony, M.P., and Jha, A., 2005. The Physical Chemistry of Thermal Decomposition of South African Chromite Minerals. *Metallurgical and Materials Transactions B*, Vol. 36(B), pp. 75-84.

Thorslund P., Wickman, F.E., Nyström, J.O., 1984. The Ordovician chondrite from Brunflo, central Sweden, I. General description and primary minerals. *Lithos*, Vol. 17, pp. 87–100.

Uchida, T., Wang, Y., Rivers, M.L., Sutton, S.R., Weidner, D.J., Vaughan, M.T., Chen, J., Li, B., Secco, R.A., Rutter, M.D., and Liu, H., 2002. A large-volume press facility at the Advanced Photon Source: diffraction and imaging studies on materials relevant to the cores of planetary bodies. *J. Phys.: Condens. Matter*, Vol. 14, pp. 11517-11523.

Valkenburg, V.A., 1965. Conference Internationale Sur-les-Hautes Pressions. *LeCreusot, Saone-et-Loire, France*.

Wang, Z., O'Neill, H., Lazor, P., Saxena, S.K., 2002. High pressure Raman spectroscopic study of spinel MgCr₂O₄. *J. Phys. Chem. Solids*, Vol. 63, pp. 2057–2061.

Wang, Z., Saxena, S.K., Lazor, P., and O'Neill, H.S.C., 2003. An In Situ Spectroscopic Study of Pressure Induced Dissociation of Spinel NiCr₂O₄. *Journal of Physics and Chemistry of Solids*, Vol. 64, pp. 425-431.

Willmott, P., 2011. An introduction to synchrotron radiation: techniques and applications. *John Wiley and Sons Ltd, United Kingdom, 2011*

Xie X., Chen M., and Wang D., 2001. Shock-related mineralogical features and P-T history of the Suizhou L6 chondrite. *Eur. J. Mineral.*, Vol. 13, pp. 1177–1190.

Xie X., Minitti M., Chen M., Mao H. K., Wang D., Shu J., and Fei Y., 2002. Natural high-pressure polymorph of merrillite in the shock melt veins of the Suizhou L6 chondrite. *Geochim. Cosmochim. Acta*, Vol. 66, pp. 2439–2444.

Yamamoto, S., Komiya, T., Hirose, K., Maruyama, S., 2009. Coesite and clinopyroxene exsolution lamellae in chromites: In-situ ultrahigh-pressure evidence from podiform chromitites in the Luobusa ophiolite, southern Tibet. *Lithos*, Vol. 109, pp. 314–322.

Yang, J.-S., Dobrzhinetskaya, L., Bai, W.-J., Fang, Q.-S., Robinson, P.T., Zhang, J., Green, H.W., 2007. Diamond- and coesite-bearing chromitites from the Luobusa ophiolite. *Tibet. Geo.*, Vol. 35, pp. 875–878.

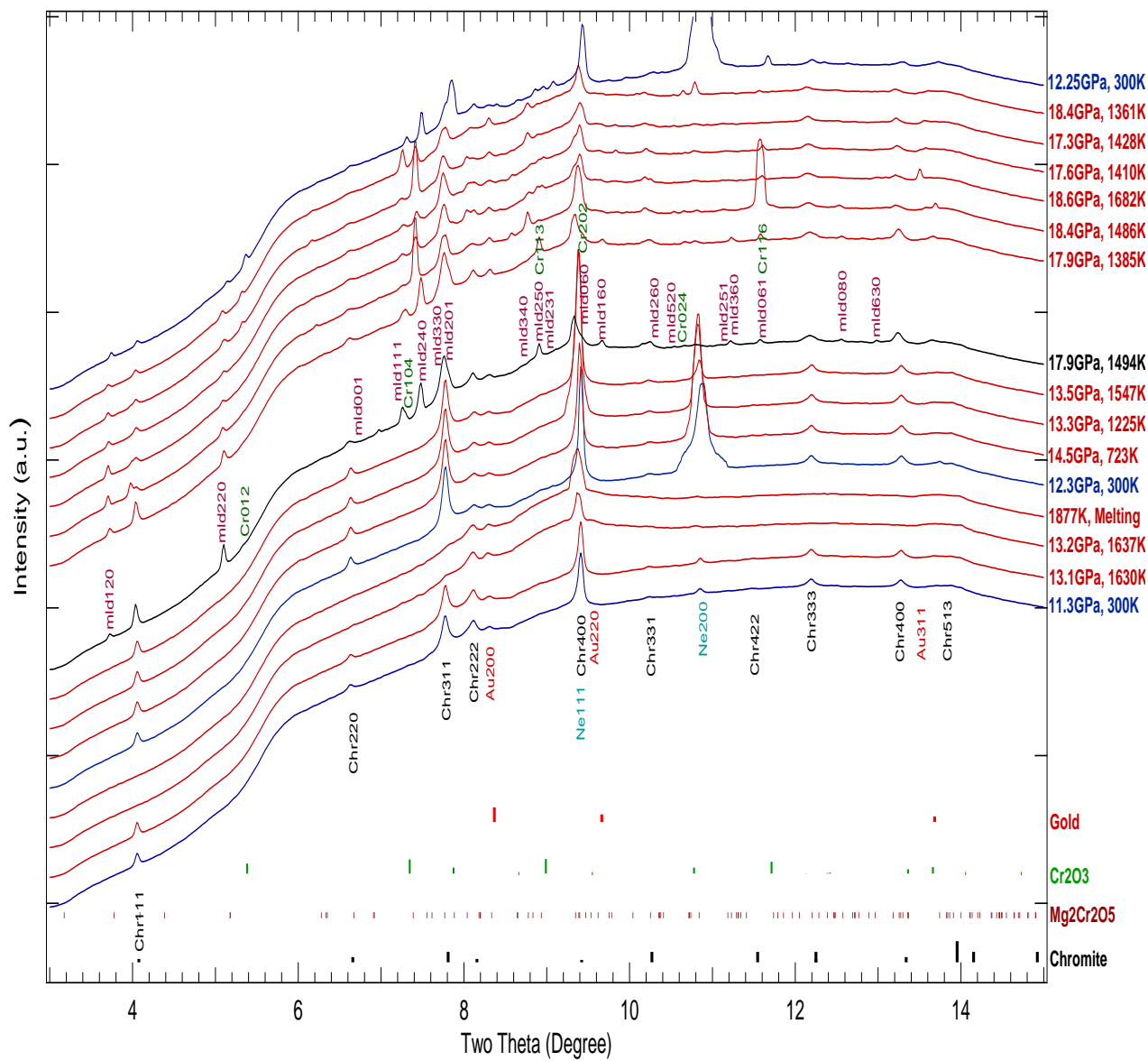
Yong, W., Botis, S., Shieh, S. R., Shi, W., Withers, A. C., 2012. Pressure-induced phase transition study of magnesiochromite (MgCr₂O₄) by Raman spectroscopy and X-ray diffraction. *Physics of the Earth and Planetary Interiors*, Vol. 196, pp. 75-82.

Zerr, A., Miehe, G., Serghiou, G., Schwarz, M., Kroke, E., Riedel, R., Fuess, H., Kroll, P., and Boehler, R., 1999. Synthesis of cubic silicon nitride. *Nature*, Vol. 400, pp. 340-352.

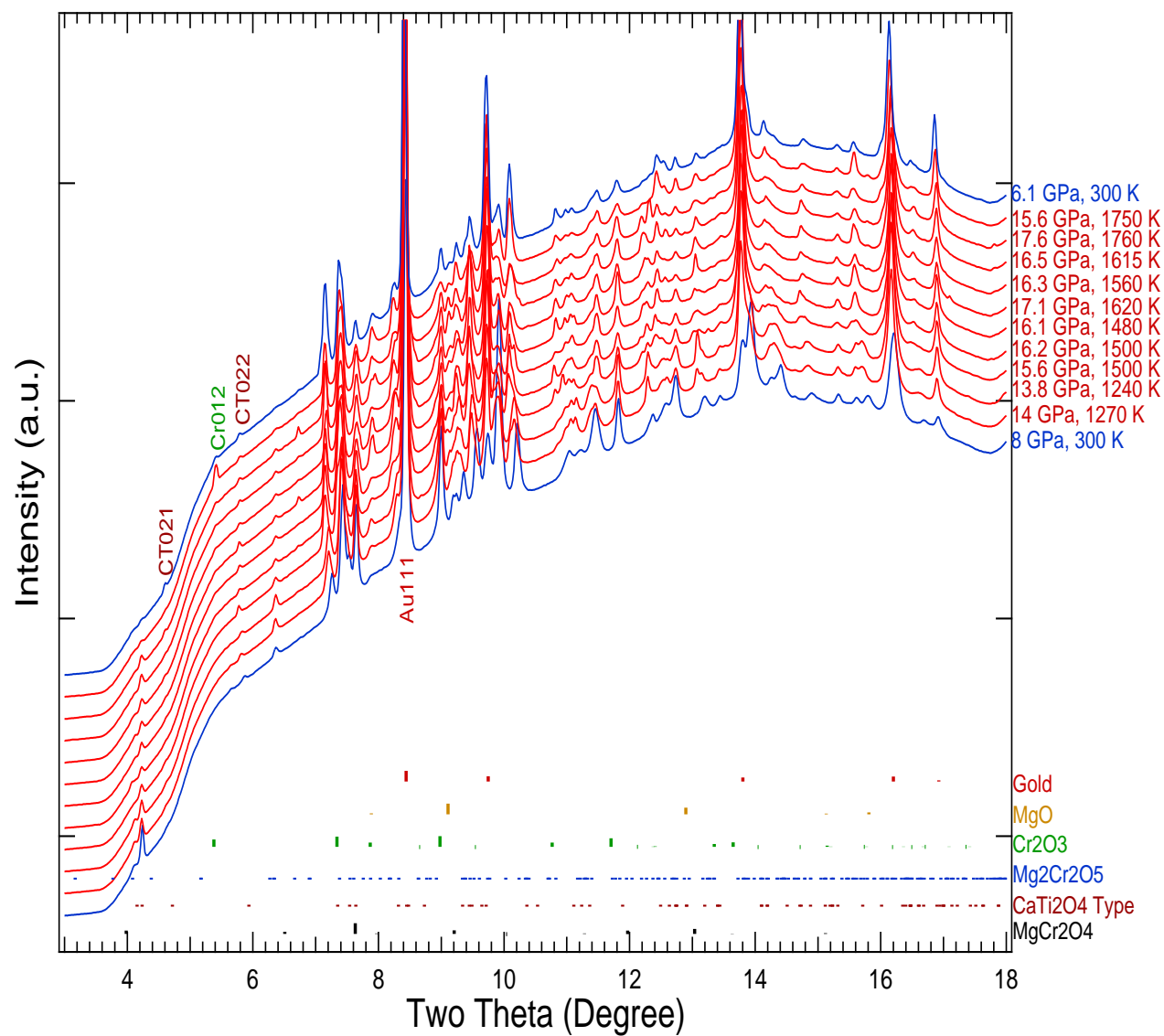
Zhou, X.B., De Hosson, J.Th.M., 1991. Spinel/Metal Interfaces in Laser Coated Steels: A Transmission Electron Microscopy Study. *Acta Metallic Materials*, Vol. 39 (10), pp. 2267-2273.

Appendices

Appendix A1: MgCr_2O_4 decomposed to $\text{Mg}_2\text{Cr}_2\text{O}_5$ and Cr_2O_3 at about 1500 K and 18 GPa.



Appendix A2: Cr_2O_3 peaks showed up after reheating the synthesized CaTi_2O_4 type structure of MgCr_2O_4



Appendix A3: Calculated and observed peak positions of synthesised CaTi_2O_4 type MgCr_2O_4 .

d(obs)	hkl	d(calc)	res(d)
4.84539	002	4.84905	-.00366
4.27304	021	4.27126	0.00179
3.39788	022	3.39597	0.00191
2.74008	110	2.74303	-0.00295
2.67359	023	2.67384	-0.0002
2.63722	111	2.63935	-0.00212
2.38076	040	2.37876	0.00201
2.16306	024	2.16019	0.00288
2.12425	130	2.12589	-0.0016
2.08864	113	2.09134	-0.00270
2.0749	131	2.07652	-0.002
1.94639	132	1.94689	-5E-04
1.81662	114	1.81644	0.00017
1.79706	025	1.79609	0.00097
1.77648	133	1.77611	0.00037
1.6169	006	1.61635	0.00055
1.58458	150	1.5851	-0.0006
1.5641	151	1.56434	-0.0002
1.50657	152	1.50661	-5E-05
1.50362	045	1.50324	0.00039
1.43212	135	1.43275	-0.0006
1.42431	063	1.42375	0.0006
1.39313	116	1.3925	0.0007
1.37754	202	1.37357	0.00397
1.33739	046	1.33692	0.00047
1.3262	154	1.32667	-5E-04
1.28318	136	1.28659	-0.00341
1.26116	223	1.26249	-0.0013

1.22699	240	1.22705	-6E-05
1.21637	241	1.21732	-1E-03
1.19554	047	1.19719	-0.002
1.19011	080	1.18938	0.0007
1.18075	081	1.18053	0.0002
1.16105	137	1.16063	0.0004
1.12054	225	1.11974	0.0008
1.10994	118	1.10873	0.0012

Appendix A4: Calculated and observed peak positions of synthesised $\text{Mg}_2\text{Cr}_2\text{O}_5+\text{Cr}_2\text{O}_3$ and CaTi_2O_4 type MgCr_2O_4 .

d(obs)	Mg₂Cr₂O₅			Cr₂O₃			CaTi₂O₄ type		
	hkl	d(calc)	res(d)	hkl	d(calc)	res(d)	hkl	d(calc)	res(d)
5.213002	120	5.2092	0.0038						
4.818596	200	4.8161	0.00249						
4.2607							021	4.26542	-0.00472
3.800495	220	3.8018	-0.0013						
3.627271				012	3.63063	-0.00335			
3.391873							022	3.39019	0.00168
3.128075	230	3.13453	-0.00645						
3.098274	040	3.0965	0.00178						
2.945155	140	2.94791	-0.00276						
2.736519							110	2.73645	0.00007
2.664371				104	2.66113	0.00324	023	2.6687	-0.00432
2.634414							111	2.63318	0.00124
2.608906	240	2.6046	0.00431						
2.529234	330	2.53453	-0.0053						
2.498646	121	2.49312	0.00553						
2.479125				110	2.48263	-0.00351			
2.452912	201	2.44598	0.00694						
2.404155	150	2.39913	0.00503						

2.378983						040	2.37603	0.00295	
2.280135	221	2.27496	0.00517						
2.262742				006	2.25855	0.0042			
2.206014	250	2.20288	0.00314						
2.173841				113	2.17568	-0.00184			
2.157319						024	2.15576	0.00156	
2.136896						042	2.13271	0.00419	
2.117513						130	2.12186	-0.00434	
2.100114	231	2.10439	-0.00428						
2.082865	041	2.09277	-0.00991			113	2.08663	-0.00377	
2.070852						131	2.07261	-0.00176	
2.013422	160	2.0185	-0.00507						
1.943569						32	1.94318	0.00039	
1.910908						043	1.91299	-0.00208	
1.893545	260	1.89738	-0.00383						
1.833987	151	1.83256	0.00142						
1.81373				024	1.81531	-0.00158	114	1.81238	0.00135
1.794802						025	1.79228	0.00252	
1.771611						133	1.77265	-0.00104	
1.759651	421	1.76074	-0.00109						
1.74406	530	1.74575	-0.00169						
1.700807						044	1.69509	0.00571	
1.670563				116	1.67065	-0.00009			
1.649873	161	1.64516	0.00471						
1.615713	351	1.61375	0.00196	211	1.6137	0.00201	006	1.61267	0.00305
1.603345	600	1.60537	-0.00202				134	1.59515	0.0082
1.580593	511	1.58112	-0.00053	122	1.58043	0.00016	115	1.58002	0.00057
1.558837	620	1.554	0.00483				151	1.56189	-0.00305
1.541323	521	1.54384	-0.00251						
1.518497	550	1.52072	-0.00222						
1.503284							152	1.5042	-0.00092
1.486321	531	1.48716	-0.00083						
1.472962	280	1.47396	-0.00099						
1.464203				214	1.46536	-0.00116			

1.429616	470	1.42588	0.00374	300	1.43335	-0.00373	135	1.42984	-0.00022
1.420615	002	1.41972	0.0009				153	1.42081	-0.00019
1.408371	560	1.40843	-0.00005						
1.391076	380	1.39458	-0.0035	125	1.39385	-0.00278	116	1.38935	0.00173
1.374701	461	1.37212	0.00258				202	1.37023	0.00378
1.363826	621	1.3632	0.00063				220	1.36823	-0.0044
1.334077							046	1.33435	-0.00027
1.317591							222	1.31659	0.001
1.302991	570	1.30315	-0.00016						
1.293531	232	1.29325	0.00028	1010	1.29247	0.00107			
1.285166				119	1.28742	-0.00226	136	1.28393	0.00124
1.270643	322	1.27081	-0.00017						
1.259425	740	1.25746	0.00197				223	1.25958	-0.00015
1.250375				217	1.2448	0.00558			
1.239382	0100	1.2386	0.00078	220	1.24132	-0.00193			
1.229906	191	1.22831	0.00159				204	1.23018	-0.00027
1.224463	402	1.22299	0.00147				155	1.22511	-0.00049
1.212235	721	1.21425	-0.00201	306	1.21021	0.00203			
1.202725	750	1.20291	-0.00018						
1.192875	252	1.19335	-0.00048	131	1.18803	0.00485			
1.166885	062	1.16978	-0.00289				028	1.17213	-0.00524

Appendix A5: Laser heating spot on the sample from both sides



Appendix A6: Composition of different samples

Sample	MgO (%)	FeO (%)	Cr ₂ O ₃ (%)	Al ₂ O ₃ (%)	Others (%)
MgCr ₂ O ₄	20.9	-	79.1	-	-
FeCr ₂ O ₄	-	32.1	67.9	-	-
Natural Chromite	11	23	50	15	1

Appendix A7: Ionic radius of different ions

Ions	Radius (pm)
Mg²⁺	86
Cr³⁺	75.5
Fe²⁺(ls)	75
Fe²⁺(hs)	92
Al³⁺	67.5
O²⁻	140

Appendix A8: High pressure polymorphs of different spinel group minerals

Spinel	Polymorphs
MgCr ₂ O ₄	<ol style="list-style-type: none"> 1. Cr₂O₃+MgO 2. Mg₂Cr₂O₅+Cr₂O₃ 3. CaTi₂O₄ type structure
FeCr ₂ O ₄	<ol style="list-style-type: none"> 1. FeCr₂O₅+Cr₂O₃ 2. CaFe₂O₄-type structure 3. CaTi₂O₄-type structure
MgAl ₂ O ₄	<ol style="list-style-type: none"> 1. MgO+Al₂O₃ 2. Mg₂Al₂O₅ + Al₂O₃ 3. CaFe₂O₄ type structure 4. CaTi₂O₄-type structure

Appendix A9 : Interatomic distances and angles in the structures of CaTi₂O₄ (CT)-type MgCr₂O₄ and modified ludwigite (mLd)-type Mg₂Cr₂O₅ (Ishii et al., 2015).

CT-type MgCr₂O₄					
Bond length (Å)				Bond angles (°)	
Mg–O ²ⁱ × 2	1.989(2)	Cr–O ³ⁱⁱⁱ × 2	1.958(1)	O ^{1vi} –Cr1–O ³ⁱⁱⁱ	172.4(1)
Mg–O ³ⁱⁱ × 4	2.270(1)	Cr–O ²	1.960(1)	O ² –Cr1–O ^{3iv}	179.8(1)
Mg–O ¹ × 2	2.631(1)	Cr–O ^{3iv}	2.016(2)	Cr ^{1vii} –O ¹ –Cr ^{1viii}	89.58(4)
Average	2.290	Cr–O ^{1v} × 2	2.023(1)	Cr ^{1vii} –O ^{1vi} –C ^{1vi}	90.42(4)
<i>n_c</i>	4.93	Average	1.990	Cr1–O ² –Cr ^{1iv}	124.7(1)
BVS	1.90	<i>n_c</i>	5.95	Cr ^{1ix} –O ³ –Cr ^{1x}	93.44(10)
		BVS	2.94	Cr ^{1ix} –O ³ –Cr ^{1iv}	96.81(9)
mLd-type Mg₂Cr₂O₅					
Bond length (Å)					
M1 site		M2 site		M3 site	
M1–O ¹ × 4	2.010(2)	M2–O ^{3x} × 2	2.028(3)	M3–O ^{2x} × 2	2.012(2)
M1–O ^{2x} × 2	2.066(3)	M2–O ⁴ × 4	2.117(2)	M3–O ³ × 2	2.016(2)
Average	2.029	Average	2.088	M3–O ⁴	2.062(3)
<i>n_c</i>	5.97	<i>n_c</i>	5.91	M3–O ^{5x}	2.064(3)
BVS	2.43	BVS	2.07	Average	2.030
				<i>n_c</i>	5.97
				BVS	2.42
M4 site		M5 site			
M4–O ¹ × 2	1.963(2)	M5–O ¹ × 2	2.099(2)		

M4–O2 ^{xi}	2.011(3)	M5–O3 × 2	2.134(3)		
M4–O4 × 2	2.029(2)	M5–O5 × 2	2.190(3)		
M4–O5	2.035(3)	Average	2.141		
Average	2.005	n_c	5.93		
n_c	5.95	BVS	1.80		
BVS	2.59				
Bond angles (°)					
O1–M1–O1 ^{vii}	90.6(1)	M3 ^{ix} –O2 ^{vi} –M1 ^{xii}	121.2(2)	M3 ^{ix} –O3–M3 ^{xv}	90.5 (1)
O1–M1–O2 ^x	97.32(7)	M1–O1–M1 ^{xii}	90.6(1)	M3–O5–M3 ^{xii}	90.2(2)
O4–M2–O4 ^{xii}	84.85(8)	M4–O2–M1 ^{xiii}	95.85(3)	M4 ^{vii} –O4–M3	96.64(5)
O3 ^x –M2–O4 ^{xii}	84.92(8)	M1 ^{xii} –O1–M4 ^{xiv}	96.15(5)	M3 ^{xii} –O5–M4	97.95(5)
O3 ^x –M3–O5 ^{vii}	169.29(9)	M2–O4–M2 ^{vii}	84.9(1)	M4 ^{vii} –O2–M3 ^{ix}	121.85(4)
O4–M3–O2 ^x	179.4(2)	M3–O4–M2 ^{vii}	92.0(1)	M4–O2–M4 ^{vii}	93.4(1)
O2–M4–O4 ^{xii}	176.12(1)	M3 ^{xv} –O3–M2 ^{ix}	96.2(1)	M4–O4–M4 ^{vii}	89.5(1)
O1 ^{xi} –M4–O5	172.0(2)	M4 ^{vii} –O4–M2 ^{vii}	92.16(3)		

Curriculum Vitae

Name: Tauhid Belal Khan

Post-secondary Education and Degrees: [2004-2009] BSc. in Civil Engineering
Bangladesh University of Engineering and Technology, Dhaka, Bangladesh

[2011-2013] MSc. in Advanced Clay Science
Université de Poitiers, Poitiers, France

[2013-2015] MSc. in Geophysics
University of Western Ontario, London, Ontario, Canada

Honours and Awards: [2013-2015] Western Graduate Research Scholarship
[2014] Canadian Exploration Geophysical Society travel bursary and book award
[2011-2013] Erasmus Mundus Scholarship

Related Work Experience: [2013-2015] Teaching Assistant and Research Assistant
University of Western Ontario, London, Ontario, Canada

[2010-2011] Lecturer
University of Information Technology and Sciences, Dhaka, Bangladesh

Publications:

Chemed, Y.C., Christidis, G.E., **Khan, T.B.**, Koutsopoulou, E., Hatzistamou, V., Kelessidis, V.C., 2014. Rheological properties of palygorskite-bentonite and sepiolite-bentonite mixed clay suspensions, *Applied Clay Science*, vol. 90, pp. 165–174.

Begum, M., Salekin, M.S., **Khan, T.B.**, Ahmed, W., 2013. Cost Analysis of Steel Concrete Composite Structures in Bangladesh, *Asian Journal of Civil Engineering (BHRC)*, 14 (6): 935-944

Conference paper and Poster presentation:

Tauhid Belal Khan, Sean R. Shieh, Vitali Prakapenka, Clemens Prescher (2015) Equation of state of CaTi₂O₄ type structure of chromite. *Poster presentation in proceedings of distinguished Lecturer and Materials & Biomaterials Research Showcase. April 27, Western University, London, ON, Canada*

Tauhid Belal Khan, Sean R. Shieh, Vitali Prakapenka, Clemens Prescher (2014) Equation of state of high pressure polymorph of magnesiochromite spinel. *Poster presentation in proceedings of interdisciplinary Research Showcase. December 02, Western University, London, ON, Canada*

Sean R. Shieh, Tianqi Xie, **Tauhid Belal Khan**, Ievgeniia Morozova (2014) Materials under extreme environment. High pressure diamond anvil cell study. *Poster presentation in proceedings of interdisciplinary Research Showcase. December 02, Western University, London, ON, Canada*

Sean SHIEH, **Tauhid Belal KHAN**, Zhongying MI, Vitali PRAKAPENKA (2014) Stability and Elasticity of Chromium Spinel. *In proceedings of the 11th Annual Meeting of the Asia Oceania Geosciences Society (AOGS), July 28-August 1, at Royton Sapporo Hotel, Japan*

Tauhid Belal Khan, George Christidis (2013) Rheological properties of mixed sepiolite-bentonite suspensions. *In proceedings of the 11th Annual Conference - Groupe Français des Argiles (GFA), April 9-11, Laboratoire de Réactivité de Surface à Ivry sur Seine, 24, Université Pierre et Marie Curie, Site Le Raphaël, 3 rue Galilée, 94200.*

Tauhid Belal Khan, Bruno Lanson, Fabien Hubert, Nathaniel Findling, Camille Rivard, Michelle M. Wander (2013) Influence of cropping practices on CLAY MINERALOGY: Insights from the MORROW PLOTS experimental fields. *Poster presentation in proceedings of the 50th anniversary annual meeting of the Clay Minerals Society, October 6-10, University of Illinois Urbana-Champaign.*